A Numerical Investigation of Rectangular Cylinders with Interest in Maximizing Drag

Jonathan M. Wai

A dissertation

submitted in partial fulfillment of the

requirements for the degree of

Doctor of Philosophy

University of Washington

2015

Reading Committee:

Robert Breidenthal, Chair

Peter Rhines

Mitsuru Kurosaka

Program Authorized to Offer Degree:

Aeronautics and Astronautics

University of Washington

Abstract

A Numerical Investigation of Rectangular Cylinders
with Interest in Maximizing Drag

Jonathan M. Wai

Chair of the Supervisory Committee:
Professor Robert Breidenthal
Aeronautics and Astronautics

In this dissertation, rectangular cylinder flow is explored through a series of numerical simulations. First, rectangular cylinders at a Reynolds number of 20,000 are simulated using Reynolds-Averaged Navier-Stokes (RANS) simulations and detached eddy simulations (DES). 2-D and 3-D simulations are performed using a variety of turbulence models. It is found that unlike 2-D simulations, the 3-D simulations are found to be in agreement with the experimental data over the entire range of aspect ratios simulated. The results of the 2-D and 3-D simulations was found to be consistent with existing literature. Unfortunately, RANS simulations are not ideal for learning about the physics of the flow due to a different set of governing equations than nature.

A switch to direct numerical simulations (DNS) is made and 3-D simulations of rectangular cylinders at Re = 500 are performed. For the aspect ratios considered at Re = 500, it is uncharted territory due to the lack of experimental data and simulation results. A significant change in drag coefficient vs. aspect ratio is found when compared to the higher Reynolds number case. This

change is thought to be due to the lack of vortex roll-up in the free shear layer that only appears in the high Reynolds number case. In addition, there is a local increase in the drag coefficient that corresponds to the mean spanwise flow and free shear layer impingement.

Last, we perform a series simulations where suction and blowing are applied to an aspect ratio 0.62 rectangular cylinder. Through this method, we attempt to increase its drag coefficient from its value at Re = 500 (2.24) to its value at Re = 20,000 (2.94). It is found that the drag coefficient does indeed increase, but not for the reasons originally expected.

TABLE OF CONTENTS

LIST OF FIGURES

LIST OF TABLES

ACKNOWLEDGEMENTS

I would not have been able to complete this dissertation if not for the support of many individuals. Whether it was their technical expertise or simply their friendship, I am grateful for everyone who has stood beside me through my many years of education.

First of all, I would like to thank my adviser, Robert Breidenthal. Little did he know at the time, but his introduction of the rectangular cylinder problem turned out to be perfect for my interests. A project where we attempt to achieve something completely backwards from the norm in aeronautics has been right up my alley. In addition, he has allowed me to grow individually as a researcher, while providing timely guidance when needed. I have thoroughly enjoyed having him as an advisor including his jokes.

I would also like to thank the rest of committee, which comprised of Peter Rhines, Mitsuru Kurosaka, Kuen Lin, and John Kramlich. Thank you for your guidance and support these past few years. Peter thank you for the opportunities you provided me in your lab in the past and being a part of my reading committee. Mitsuru, thank you also for being a part of my reading committee. Kuen, thank you so much for waking up early while on sabbatical to attend my defense via Skype.

In addition, the numerical simulations presented would never have been possible without the following individuals. I absolutely must thank Pieter Buning of NASA Langley, Thomas Pulliam of NASA Ames, Philippe Spalart of Boeing who have all been very, very helpful and patient with me during the entire process. Whenever I ran into an obstacle with the computations, they provided much needed guidance. I am also grateful for technical support provided by Brian Leverson. Without his help with the department cluster, this project would not have been possible.

Next, I must thank my all of my friends. There are too many of you to name individually, but I would like to thank you all for keeping me grounded, keeping me sane, and keeping me laughing throughout the years. I am appreciative of all of you and the love that you have shown me. Know that without your support, I may never have seen this through.

Finally, I must thank my family for their love and support. To my parents, John and Nancy Wai, thank you for raising me, providing me with everything I have ever needed, and more. Thank you dad for your help with CFD and being my on-call resource. To my sister, Janna Wai, thank you

providing the push I needed to finish. Here is a little endorsement for you. For those of you who read my dissertation, please read hers as well!

Chapter 1. INTRODUCTION

1.1 MOTIVATION

In engineering, when it comes to the motion of objects, drag is the force that must be overcome. Airplanes, cars, boats, and urban structures are all subject to its effects, which leaves engineers to do their best to account for it and design around it. Nevertheless, as undesirable as drag sounds, it does have its applications. Paddles, parachutes, airbrakes, and aeroballistics are a few such applications where increased drag is actually desired. In the design of such objects, it can be imagined that maximizing the drag would actually be optimal. By maximizing the drag in such applications, weight, material, and fuel can be conserved due to physically smaller objects being able to provide an equivalent drag force with a smaller cross-section. However, how to begin designing geometries with maximized drag is a daunting task. There are an infinite number of geometries that can be considered that would take many lifetimes to search. Fortunately, prior research into the rectangular cylinder has provided a place to start.

Prior experiments into rectangular cylinder flow have shown that an aspect ratio 0.62 rectangular cylinder has a drag coefficient of approximately 3. This drag coefficient is greater than any other known geometry in the Reynolds number range of 2×10^4 - 7×10^4. The significance of this result becomes apparent when it is compared to other, more well-known geometries, such as, the circular cylinder and a perpendicular flat plate. At similar Reynolds numbers, the two geometries have drag coefficients of 1.2 and 2, respectively. In this thesis, we will explore the cause for the drag increase through numerical simulations. Through these simulations, it is hoped that the underlying physics of the flow can be made apparent and applied to increase the drag of other geometries.

1.2 BRIEF HISTORY

In this section, a brief history of the rectangular cylinder problem and the computational fluid dynamics program, OVERFLOW, used throughout the course of this research will be provided. There have been many contributions on both fronts and their efforts should be recognized.

1.2.1 *Rectangular Cylinder*

The first publication regarding rectangular cylinders noting the drag increase was in 1967 by Nakaguchi, Hashimoto, and Muto [1]. They measured the drag coefficients and Strouhal numbers of rectangular cylinders with Reynolds numbers 2×10^4 - 6×10^4 and showed that the drag coefficient peaked to a value of 2.8 for a rectangular cylinder with aspect ratio 0.62. In addition, they showed that the Strouhal number experiences a discontinuity between aspect ratios 2.5 and 3. Bearman and Trueman followed the work of Nakaguchi, Hashimoto, and Muto by confirming their drag coefficient results as well as definitively showing that the increase in drag coefficient was due to the proximity of the shed vortices on the back face of the rectangular cylinder [2]. This was accomplished in two ways through two separate experiments on modified aspect ratio 0.62 rectangular cylinders. With a splitter plate, Bearman and Trueman interrupted the ability of the shed vortices to be formed in close proximity the rear face of the rectangular cylinder, which resulted in reduced drag. With trailing edge spoilers, they increased the length a shed vortex would be created and forced the shed vortices to be created further away from the rear face of the rectangular cylinder, which again, resulted in lower drag. Notably, the results of both experiments were in disagreement with previously published results by Hoerner, whose book *Fluid Dynamic Drag* was the knowledge base on drag up to that point [3]. The original experiments were followed by Okajima, who measured the Strouhal number of various aspect ratios over a range of Reynolds numbers, but the primary concentration of the experiment was on aspect ratios greater than or equal to 1 [4].

As the cost of numerical simulations reduced, numerical simulations of rectangular cylinders began to be performed. In the beginning, they were primarily 2-D and at much lower Reynolds number compared to the original experiment for feasibility purposes. Davis and Moore performed

2-D simulations of rectangular cylinders of Reynolds number 100 to 2800, with their primary focus being the square cylinder [5]. Okajima performed 2-D simulations of rectangular cylinders with aspect ratios 0.6 to 8 with Reynolds number 150-800 [6]. During the early 1990's, further reduction of simulation cost and the introduction of several turbulence models made it possible to attempt simulating the original experiment. Rodi compared 3-D Large Eddy Simulations (LES) and 2-D RANS simulations of a square cylinder at Reynolds number 2.2×10^4 [7]. Sohankar, Norberg, and Davidson performed 2-D and 3-D simulations of square cylinders for Reynolds numbers in the range $200 - 500$ [8]. Shimada and Ishihara performed 2-D simulations of aspect ratios 0.6 to 8.0 using a modified k-ε turbulence model [9].

The popularity of turbulence models led to the need for one of the last well-known experiments on the subject. Lyn, Einav, Rodi, and Park performed laser Doppler velocimetry (LDV) experiments measuring the ensemble-averaged flow quantities of the turbulent flow around a square cylinder [10]. Their measurements of ensemble averages provides experimental quantities equivalent to flow variables solved for using the Reynolds-Averaged Navier Stokes (RANS) equations. Their experiments have become the basis to which the results of turbulent numerical simulations of rectangular cylinders are compared to.

1.2.2 *Overflow*

Overflow is a computational fluid dynamics (CFD) software package developed in collaborative effort between NASA's Johnson Space Center and Ames Research Center. The original need for the code arose from needing a method to evaluate the flow around the space shuttle launch vehicle. The original version of the code was developed in the early 1990's by NASA's Pieter Buning and Dennis Jespersen. To this day, Dr. Buning still maintains and updates the code. Overflow is capable of solving 3-D compressible flow around solid bodies by solving the time-dependent Reynolds-Averaged Navier-Stokes equations using overset structured grids. With multiple turbulence models, boundary conditions, and numerical schemes, the code has been found fully capable of solving a wide array of CFD problems for various government agencies, for industry, and in academia while being good agreement with experiment [11, 12].

1.3 NOTATION

In this section, notation that will be used throughout the thesis and introduce the geometry of the problem will be introduced. Additional notation will be provided as necessary, but what is shown here will give the reader an adequate understanding of the problem and results obtained within this document.

The geometry of the rectangular cylinder problem is shown in Fig. 1.1. The length of the rectangle that corresponds to the dimension in the stream-wise direction is defined as d. Its width, which is perpendicular to oncoming flow, is defined as h. The ratio of these two dimensions is known as the aspect ratio and is defined in Eqn. 1.1.

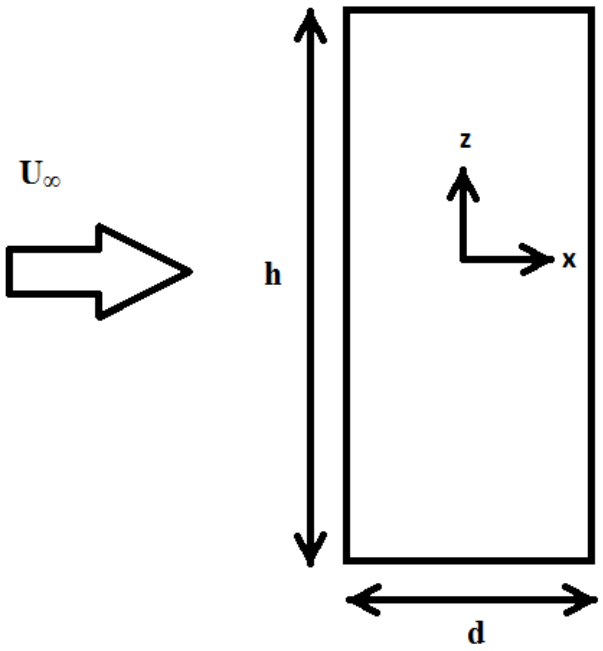

Figure 1.1 Basic geometry of rectangular cylinder flow with oncoming flow

$$AR = \frac{d}{h} \tag{1.1}$$

The Reynolds number, which is important in characterizing bluff body flows, is the dimensionless ratio of the inertial forces to viscous forces and is defined as follows:

$$Re = \frac{\rho_\infty U_\infty L}{\mu} \tag{1.2}$$

where ρ_∞ is the free-stream fluid density, U_∞ is the free-stream velocity of the fluid, μ is the dynamic viscosity, and L is the typical length scale of the flow in question. In the case of rectangular cylinder flow, h was the selected length scale.

The non-dimensional aerodynamic force coefficients of lift and drag are defined in their usual manner in the following equations:

$$C_d = \frac{F_D}{\frac{1}{2}\rho_\infty U_\infty^2 A} \tag{1.3}$$

$$C_L = \frac{F_L}{\frac{1}{2}\rho_\infty U_\infty^2 A} \tag{1.4}$$

where F_D is the force due to drag, F_L is the force due to lift, and A is the reference area.

The pressure coefficient is defined by the following:

$$C_p = \frac{p - p_\infty}{\frac{1}{2}\rho_\infty {U_\infty}^2} \tag{1.5}$$

where p is the pressure at any point in the flow field and p_∞ is the free-stream pressure.

The Strouhal number is the dimensionless measurement of the vortex shedding frequency and is defined as follows:

$$St = \frac{f_s L}{U_\infty} \tag{1.6}$$

where f_s is the vortex shedding frequency.

The vorticity, which will be mentioned extensively, is a vector field describing the local rotational motion of a fluid and is defined as follows:

$$\boldsymbol{\omega} \equiv \nabla \times \boldsymbol{U} \tag{1.7}$$

where $\boldsymbol{\omega}$ is the vorticity vector, ∇ is the del operator, and $\boldsymbol{U}$ is the velocity vector.

Chapter 2. RANS SIMULATIONS OF RECTANGULAR CYLINDERS AT RE = 20,000

2.1 MOTIVATION

During the initial literature search of rectangular cylinders, it was unclear if CFD simulations could replicate the experimental results of Nakaguchi, Hashimoto, and Muto in its entirety. Shimada and Ishihara had shown that for aspect ratios greater than 0.62 they were able to match experiment quite well with 2-D simulations using a modified k-ε turbulence model, but the ability to successfully simulate aspect ratios less than 0.62 was unknown [9]. Thus, simulations of rectangular cylinders at Reynolds number 20,000 were performed using various turbulence models. In addition, simulating the original experiment was viewed an excellent learning opportunity to discover how to perform the simulations presented in the following chapters. With an available data set, simulating the original experiment correctly would provide confirmation of the simulation method and would provide confidence for future simulations.

2.2 GRIDS

To begin the simulations, we must first consider the grid. The methodology for simulations in this paper and grid construction were largely adopted from communications with Dr. Philippe Spalart as well as his publication on detached-eddy simulations of an airfoil at a high angle of attack, which with an extensive region of separated flow qualifies as a bluff body [13]. In this section, calculations of the normal wall spacing are provided, the grid construction is discussed, and examples of the grid are shown.

2.2.1 *Normal wall spacing*

The method for calculating the normal wall spacing is the same as that adopted by the Overflow User's Manual [12]. The calculation used within the manual is presented here, while accounting for the notation used within the paper.

The dimensionless wall distance for a wall-bounded flow can be defined as

$$y^+ \equiv \frac{\rho_w u^* y}{\mu_w} \tag{2.1}$$

where ρ_w is the fluid density at the wall, μ_w is the dynamic viscosity at the wall, u^* is the friction velocity, and y is the distance to the nearest wall.

The friction velocity is defined as:

$$u^* \equiv \sqrt{\frac{\tau_w}{\rho_w}} \tag{2.2}$$

where τ_w is the wall shear stress.

The skin friction coefficient, which is a function of the wall shear stress, is defined as:

$$c_f \equiv \frac{\tau_w}{\frac{1}{2}\rho U_\infty^2} \tag{2.3}$$

If we insert Eqns. 2.2 and 2.3 into 2.1 as well as assume $\rho_w = \rho_\infty$ and $\mu_w = \mu_\infty$, we can write

$$y^+ = \frac{Re}{L}\sqrt{\frac{c_f}{2}}y \tag{2.4}$$

or

$$\frac{y}{L} = \frac{y^+}{Re\sqrt{\frac{c_f}{2}}} \tag{2.5}$$

where Re is the Reynolds number as defined in Eq. 1.2, c_f is the skin friction coefficient, and L is a typical length scale of the flow.

Using the flat plate correlation from White [14] to estimate the skin friction coefficient we get,

$$c_f \approx \frac{0.455}{\ln^2(0.06Re_x)} \tag{2.6}$$

where Re_x is the Reynolds number based with the length scale dependent on the downstream distance x.

A typical choice for x is 10% of the reference length, which results in the following:

$$Re_x = 0.1Re$$

For the value of y^+, we select a value in the range of $0 < y^+ < 5$. This range corresponds to values of y^+ within the viscous sublayer of the boundary layer, which is where the first grid point off the wall must reside to ensure it is properly resolved. For simplicity, we select $y^+ = 1$.

For the set of calculations presented in this chapter, the Reynolds number of the RANS simulations is 2×10^4. With the preceding information, we can compute,

$$Re_x = 2 \times 10^3$$
$$c_f \approx \frac{0.455}{\ln^2(0.06Re_x)}$$
$$= 0.0199$$
$$\frac{y}{L} = \frac{1}{Re\sqrt{\frac{c_f}{2}}}$$
$$\frac{y}{L} = 5.0 \times 10^{-4}$$

This estimate represents the maximum distance the first grid point off the body can be relative to the width of the rectangular cylinder, h. For the turbulent simulations presented in this paper, the selected distance was 1.0×10^{-5} to ensure that the boundary layer was properly resolved.

2.2.2 *Grid construction and boundary conditions*

Using the Overflow meshing software Overgrid, the non-dimensional grids were constructed with the rectangular cylinder width h equal to 1. Using generalized coordinates, the grids were constructed using the determined and specified values. Upon their completion, the grids were output into a file containing Cartesian coordinates. The surface grids were constructed around the point (0, 0), with the first grid point on the surface of the rectangular cylinder located at (AR/2, 0). Points were then distributed along the ξ-coordinate, which wraps around the body, until the last point coincided with the first and a periodic boundary condition was applied in ξ. An example grid showing the x-z and ξ-ζ plane is shown in Fig. 2.1. The distribution of the grid points in ξ used a hyperbolic tangent function with the smallest spacing going into the corners of the rectangular cylinder. The distance between the corner and the next grid point out in ξ was set to 1.0×10^{-3}.

In constructing 2-D and 3-D grids in Overflow, there is a slight variation. Overflow only handles 3-D grids, so even for 2-D simulations a 3-D grid must be constructed. They differ in the number of planes needed in the spanwise direction and the boundary conditions applied. For the 2-D grid, two copies of a surface grid slice were copied in the η direction and concatenated, forming 3 planes. The 2-D boundary condition applied ensured all 3 planes have identical flow. For construction of the 3-D grid, the grid slice was copied to the specified bounds of η, -1 and 1. The copied parts of the grid were then concatenated and the points in η were redistributed to 53, as suggested by Dr. Spalart. It is worth noting that in the initial trials of the 3-D simulations that if too few points in η were specified that the simulation did not show 3-D behavior and that the simulations behaved more like a 2-D simulation.

To finish the 2-D and 3-D grids, points were distributed in the ζ-coordinate using a hyperbolic tangent function. The initial spacing off the wall in the ζ-coordinate was set to be 1.0×10^{-5} as determined in the calculation of the normal wall spacing. The maximum value for ζ was set to be $15h$. The total number of grid points for each simulation varied based on the aspect ratio. The number of grid points for the 2-D and 3-D simulations are summarized in Tables 2.1 and 2.2, respectively.

The boundary conditions for the 2-D and 3-D simulations are summarized in Table 2.3. Since Overflow handles both simulations as 3-D, 6 boundary conditions need to be specified for 2-D and 3-D simulation. In specifying the boundary conditions of the 2-D and 3-D simulations, there were 4 boundary conditions in common.

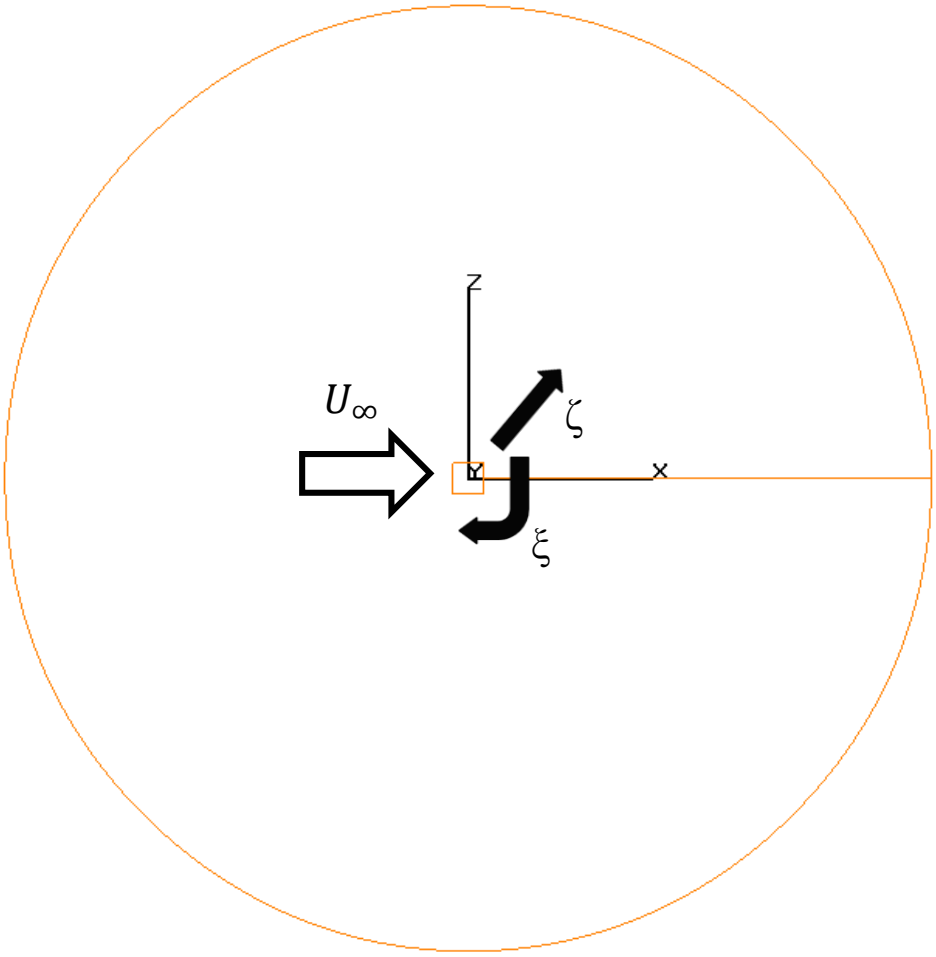

Figure 2.1 Grid of the AR = 1 case as seen from the x-z plane.

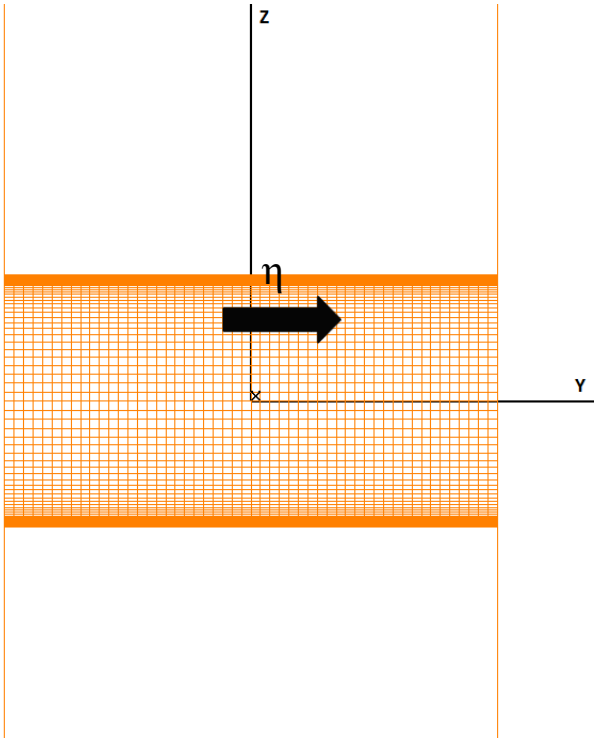

Figure 2.2 Grid of the AR = 1 case as seen from the y-z plane.

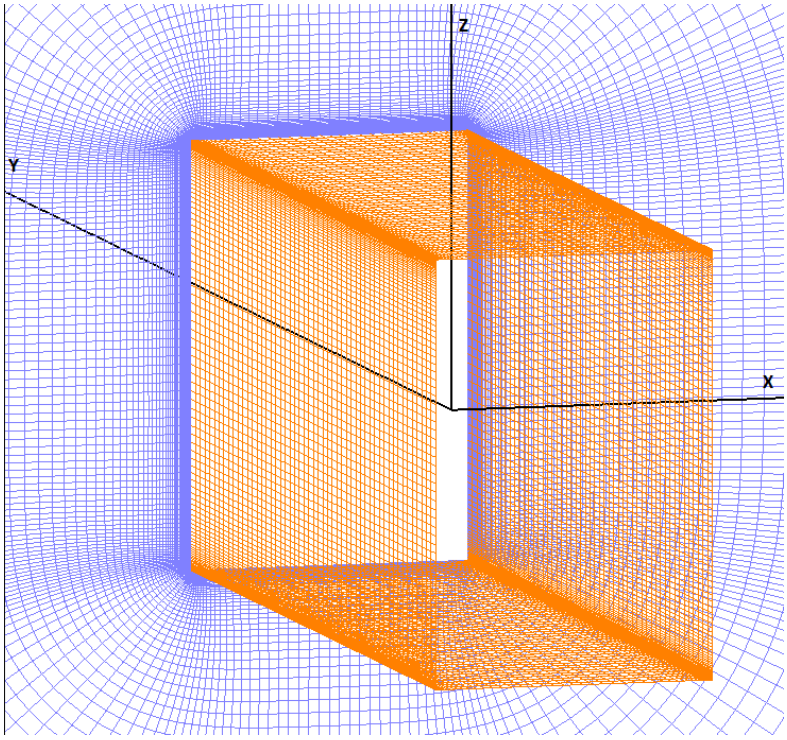

Figure 2.3 Completed 3-D grid for the AR = 1 case. Mesh in orange shows the surface grid. Mesh in blue shows one plane of the x-z plane.

Table 2.1 Number of grid points used in 2-D simulations at Re = 20,000

Aspect Ratio	J-Direction Points	K-Direction Points	L-Direction Points
0.0	401	3	301
0.1	601	3	301
0.3	701	3	301
0.5	801	3	301
0.62	801	3	301
0.8	801	3	301
1.0	801	3	301
1.5	901	3	301
2.0	1001	3	301
3.0	1201	3	301

Table 2.2 Number of grid points used in 3-D simulations at Re = 20,000

Aspect Ratio	J-Direction Points	K-Direction Points	L-Direction Points
0.0	201	53	151
0.1	241	53	151
0.3	261	53	151
0.5	281	53	151
0.62	301	53	151
0.8	301	53	151
1.0	341	53	151
1.5	361	53	151
2.0	321	53	151
2.5	361	53	151
3.0	401	53	151

Table 2.3 Summary of boundary conditions for 2-D and 3-D simulations

Simulation Type	**B. C. 1**	**B. C. 2**	**B. C. 3, 4**	**B. C. 5, 6**
2-D	Viscous wall at ζ_{min}	Characteristic outflow condition at ζ_{max}	Periodic at ξ_{min} and ξ_{max}	2-D condition in Y
3-D	Viscous wall at ζ_{min}	Characteristic outflow condition at ζ_{max}	Periodic at ξ_{min} and ξ_{max}	Inviscid wall at η_{min} and η_{max}

2.3 RANS EQUATIONS

While Overflow is capable of solving compressible flow, the simulations performed in this paper were run with the Mach number much less than 0.3, which is considered the upper limit for incompressible flow. To provide the reader an idea of the equations and variables being solved, it seems appropriate to provide a brief review of the Reynolds-Average Navier-Stokes Equations. The turbulence models will be discussed briefly, but specific details of each model will be left to their respective papers.

In deriving the Reynolds-Averaged Navier-Stokes equations, we begin by looking at the incompressible Navier-Stokes equations, which are given as:

$$\frac{\partial \boldsymbol{U}}{\partial t} + \boldsymbol{U} \cdot \nabla \boldsymbol{U} = -\frac{1}{\rho}\nabla p + \nu \nabla^2 \boldsymbol{U} \tag{2.7}$$

where $\boldsymbol{U}$ is the velocity vector, ρ is the density, p is the pressure and ν is the kinematic viscosity.

The Navier-Stokes equations are a set of non-linear, partial differential equations representing 3 equations with 4 unknowns, which are the pressure and 3 components of velocity. For closure, we consider the conservation of mass, which for an incompressible flow is given as:

$$\nabla \cdot \boldsymbol{U} = 0 \tag{2.8}$$

Reynolds decomposition is then used to separate the velocity into its average and fluctuating parts. Here, we lean on the explanation by Rodi whose explanation of Reynolds decomposition through triple decomposition provides a clear picture of the decomposed velocities [7]. The instantaneous velocity $\boldsymbol{U}$ can be decomposed into three separate quantities as follows:

$$\boldsymbol{U} = \overline{\boldsymbol{U}} + \widetilde{\boldsymbol{U}} + \boldsymbol{u}' \tag{2.9}$$

where $\overline{\boldsymbol{U}}$ is the time-mean value, $\widetilde{\boldsymbol{U}}$ is the periodic vortex-shedding component, and $\boldsymbol{u}'$ is the super-imposed stochastic turbulent fluctuation.

In RANS simulations, the ensemble average of the velocity $\langle \boldsymbol{U} \rangle$ is the primary solution variable along with the average pressure $\langle p \rangle$. The ensemble average of the velocity is equal to the sum of the time-mean value and the periodic vortex-shedding component shown in Eqn. 2.9. The ensemble average is then given as follows:

$$\langle \boldsymbol{U} \rangle = \overline{\boldsymbol{U}} + \widetilde{\boldsymbol{U}} \tag{2.10}$$

where $\langle \boldsymbol{U} \rangle$ is known as the ensemble average of the velocity.

Substituting Eqn. 2.10 into 2.9 brings us back to what is more commonly known as Reynolds decomposition, which is the sum of the ensemble average and the stochastic turbulent fluctuation. This is given as follows:

$$\boldsymbol{U} = \langle \boldsymbol{U} \rangle + \boldsymbol{u}' \tag{2.11}$$

The Reynolds-Average Navier-Stokes equations are derived by taking the ensemble average of the incompressible Navier-Stokes equations shown in Eqn. 2.7. It should be remembered that differentiation and averaging commute. Upon simplification, we arrive at the RANS equations, which are given as follows in index notation:

$$\frac{\partial\langle \boldsymbol{U_j}\rangle}{\partial t} + \langle \boldsymbol{U}\rangle \cdot \nabla\langle \boldsymbol{U_j}\rangle = -\frac{1}{\rho}\frac{\partial\langle p\rangle}{\partial \mathrm{x}_j} + \nu\nabla^2\langle \boldsymbol{U_j}\rangle - \frac{\partial\langle u_i u_j\rangle}{\partial x_i} \tag{2.12}$$

where $\langle \boldsymbol{U}\rangle$ is as defined above, $\langle p\rangle$ is the average pressure, and $\langle u_i u_j\rangle$ is the Reynolds stress, which is the term that needs to be modeled in turbulent flow.

Unlike the Navier-Stokes equations, the RANS equations represent 5 unknowns, but only 3 equations. The unknowns are the 3 components of velocity, the pressure, and the Reynolds stress, which was introduced through Reynolds decomposition. To begin closing the set of equations, first, we consider the conservation of mass. Taking the ensemble average of the mass conservation equation in Eqn. 2.8, we arrive at the following relation:

$$\nabla \cdot \langle \boldsymbol{U}\rangle = 0 \tag{2.13}$$

Finally, a turbulence model is employed to complete closure of the RANS equations. The details of each model vary, but each model is used to solve Reynolds stress through a series of approximations. The models in this paper employ the Boussinesq approximation, which introduces the concept of eddy viscosity [15]. The eddy viscosity is solved by either a series of relationships, 1 transport equation, or 2 transport equations. This leads to the classification of the turbulence models employed in this paper as algebraic, one equation, or two equation. The turbulence models considered in this paper are the Baldwin-Barth (B-B) model, the Spalart-Allmaras (S-A) model, and Menter's Shear Stress Transport (SST) model [16, 17, 18].

2.4 Simulation Parameters

Overflow is a non-dimensional, compressible flow solver. The parameters of the simulation that follow are consistent with that notation. The Reynolds number of the simulation was set to 20,000. The free-stream Mach number given as U_∞/a_∞ was set to 0.05. To force asymmetry in the flow, the angle of attack was set to 0.01 degrees and the side slip angle was set to 0.1 degrees. The other values were left as their default in Overflow as can be seen in the NAMELIST Input [12]. The right hand side of the RANS equations were solved with Euler central difference terms, while the

left hand side of the RANS equations were solved using the ARC3D Beam-Warming block tridiagonal scheme.

2.5 Results and Discussion

The results obtained in this section were collected from simulations that were allowed to run until a regular shedding pattern occurred in the force coefficients. Once a repetitive motion appeared, the simulations were stopped and the results were calculated. In this section, the results of 2-D and 3-D simulations are presented for rectangular cylinders at 20,000 and various turbulence models are employed. When the simulations were first run, how to properly simulate the aspect ratios less than 0.6 was unknown, but it was discovered through the failure of 2-D simulations to match experiment that 3-D simulations must be employed.

2.5.1 *2-D Simulations*

The drag coefficient vs. aspect ratio as determined by the 2-D simulations can be seen in Fig. 2.4. The experimental results of Nakaguchi, Hashimoto, and Muto showed that the drag coefficient as a function of aspect ratio peaks at a value of approximately 3 when the aspect ratio is 0.6. The 2-D simulations were successful at matching the experimental data for aspect ratios greater than or equal to 0.6 and this held true for all of the turbulence models employed. These results were consistent with the results of Shimada and Ishihara as well as Tian, Ong, Yang, and Murhaug [9, 19]. However, as can be seen, the 2-D simulations failed to be in good agreement with experiment for aspect ratios less than 0.6. This was again consistent with Tian et al. Shimada and Ishihara did not show results of simulations with the aspect ratio less than 0.6.

The Strouhal number vs. aspect ratio as determined by the 2-D simulations can be seen in Fig. 2.5. The sentiments on the Strouhal number mirror those of the drag coefficient. For aspect ratios greater than or equal to 0.62, the Strouhal number was captured quite well by all of the simulation. However, simulations of aspect ratios less than 0.62 were not in agreement with experiment.

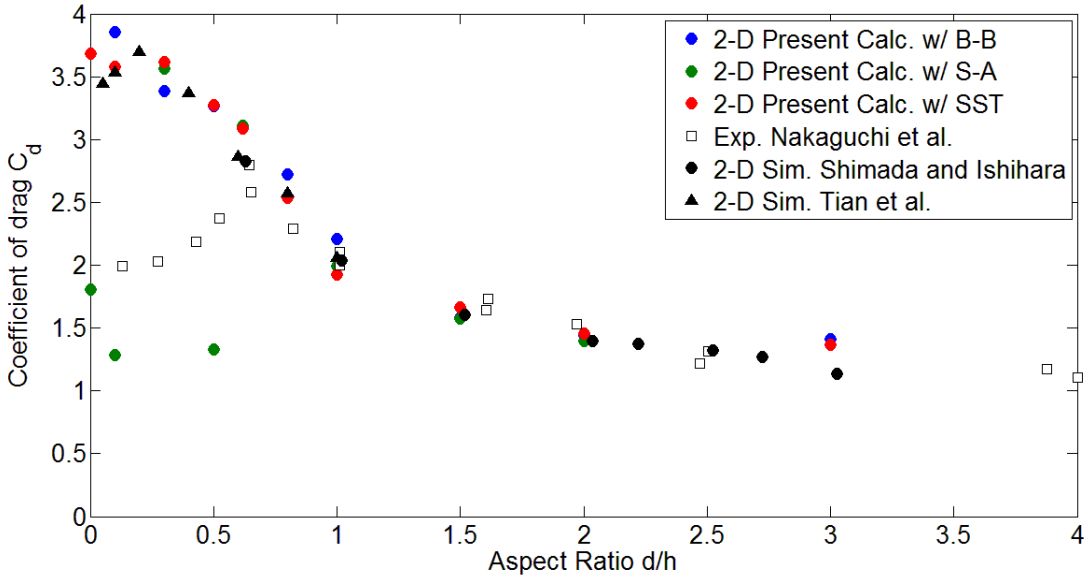

Figure 2.4 2-D simulation results of the drag coefficient vs. aspect ratio for rectangular cylinders at Re = 20,000.Experimental results from Nakaguchi, Hashimoto and Muto are shown along with simulation results of Shimada and Ishihara as well as Tian et al. [1, 9, 19].

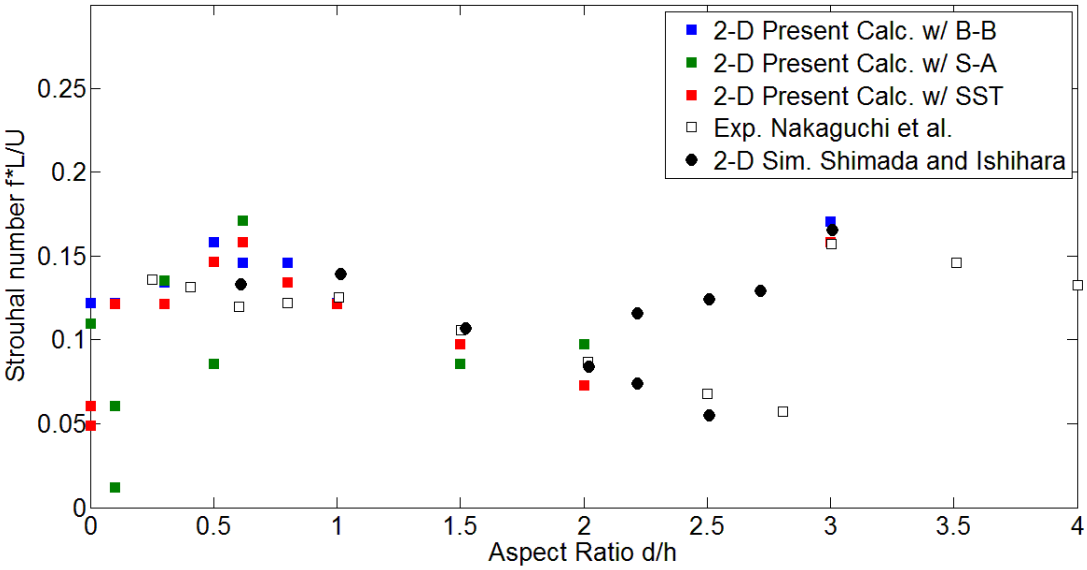

Figure 2.5 2-D simulation results of the Strouhal number vs. aspect ratio for rectangular cylinders at Re = 20,000.Experimental results from Nakaguchi, Hashimoto, and Muto are shown along with simulation results of Shimada and Ishihara [1, 9].

2.5.2 *3-D Simulations*

Upon the failure of the 2-D simulations to be in reasonable agreement with experiment over the entire range of aspect ratios, the shift to 3-D simulations was made. Literature on circular cylinders by Roshko as well as Williamson made it clear that the flow around the rectangular cylinders at that Reynolds number was inherently 3-D [20, 21]. For circular cylinders, instabilities in the spanwise direction have been observed to begin developing around a Reynolds number of 200. With the simulations and original experiment having a Reynolds number two orders of magnitude greater, it was deduced that failure to resolve the 3-D motions in the spanwise direction were the reason for the 2-D simulations inability to match experiment.

The drag coefficient vs. aspect ratio as determined by the 3-D simulations can be seen in Fig. 2.6. Unlike the 2-D simulations, the 3-D simulations were in good agreement with experiment over the entire range of aspect ratios simulated. In addition, the simulations with varying turbulence models were also in good agreement with one another, showing little variation in their results. Even though the approximation was inappropriate, 3-D laminar simulations were also run at Re = 20,000. The results of the simulations were similar to the 2-D simulations, where aspect ratios greater than 0.62 appear to be in good agreement with experiment, while aspect ratios less than that are not.

The Strouhal vs. aspect ratio as determined by the 3-D simulations can be seen in Fig. 2.7. All of the simulation results appear to be in reasonable agreement with experiment. Like the drag coefficient, the simulations run appear to be in agreement with one another across all turbulence models employed. However, for some of the results with the aspect ratios greater than 1, the Strouhal number is consistently lower than experiment. The cause of which not entirely known, but could be inherent to the RANS calculation where turbulent fluctuations in the velocity are neglected.

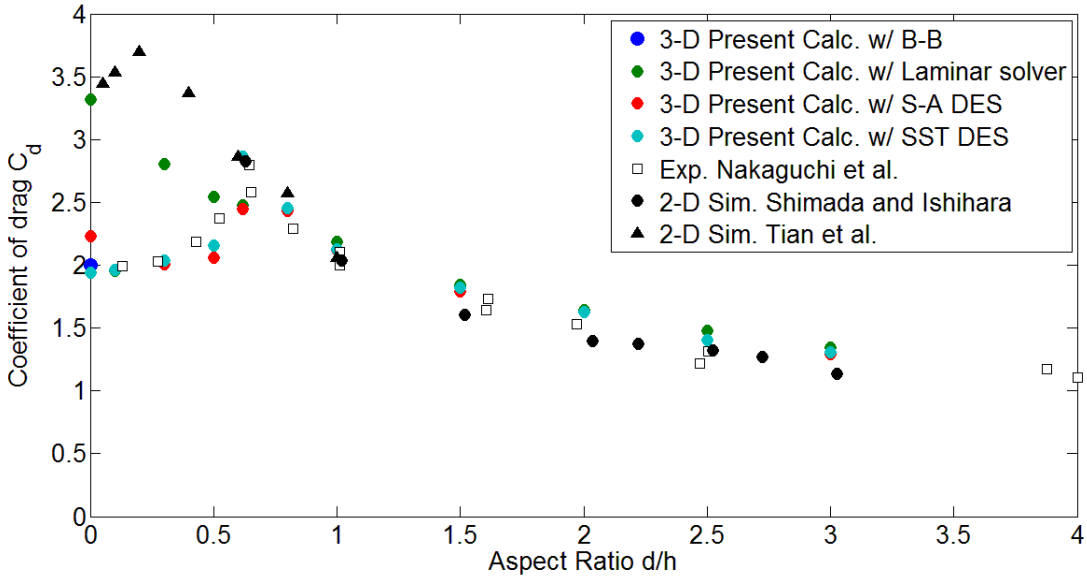

Figure 2.6 3-D simulation results of the drag coefficient vs. aspect ratio for rectangular cylinders at Re = 20,000.Experimental results from Nakaguchi, Hashimoto and Muto are shown along with simulation results of Shimada and Ishihara as well as Tian et al. [1, 9, 19].

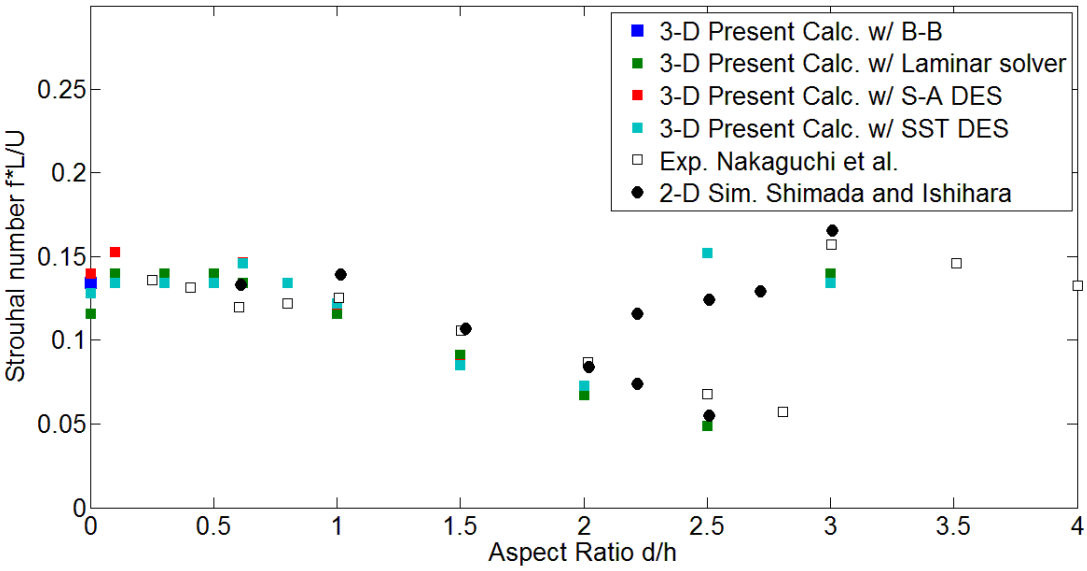

Figure 2.7 3-D simulation results of the Strouhal number vs. aspect ratio for rectangular cylinders at Re = 20,000.Experimental results from Nakaguchi, Hashimoto, and Muto are shown along with simulation results of Shimada and Ishihara [1, 9].

The success of the 3-D simulations warranted a closer look at the surface pressure coefficient. The results are shown in Fig. 2.8. As expected, the distribution of the pressure coefficient on the front face of the rectangular cylinders simulated is approximately the same. There exists a little variation for some of the aspect ratios going into the leading edge corners. On the back face, we see very different distributions of the pressure coefficient with the aspect ratio 0.62 case exhibiting the lowest average pressure.

While analyzing the pressure coefficient, sharp spikes in the pressure were observed in the vicinity of the corners. At the time, it was unclear if this was an artifact of the simulation or a feature that is supposed to exist. An example of the pressure spikes can be seen in Fig. 2.9. Consistently throughout rectangular cylinder literature regarding the pressure coefficient, no pressure spikes were found, which casted doubt on the present simulations. However, with the help of Dr. Spalart, it was discovered that the pressure spikes are a real feature that are supposed exist. The viscous flow at a sharp convex corner corner does not have to be regular, and in such corners, the Stokes equations produce singularities with infinite vorticity and most likely infinite pressure. A review of this is given by Moffat [22].

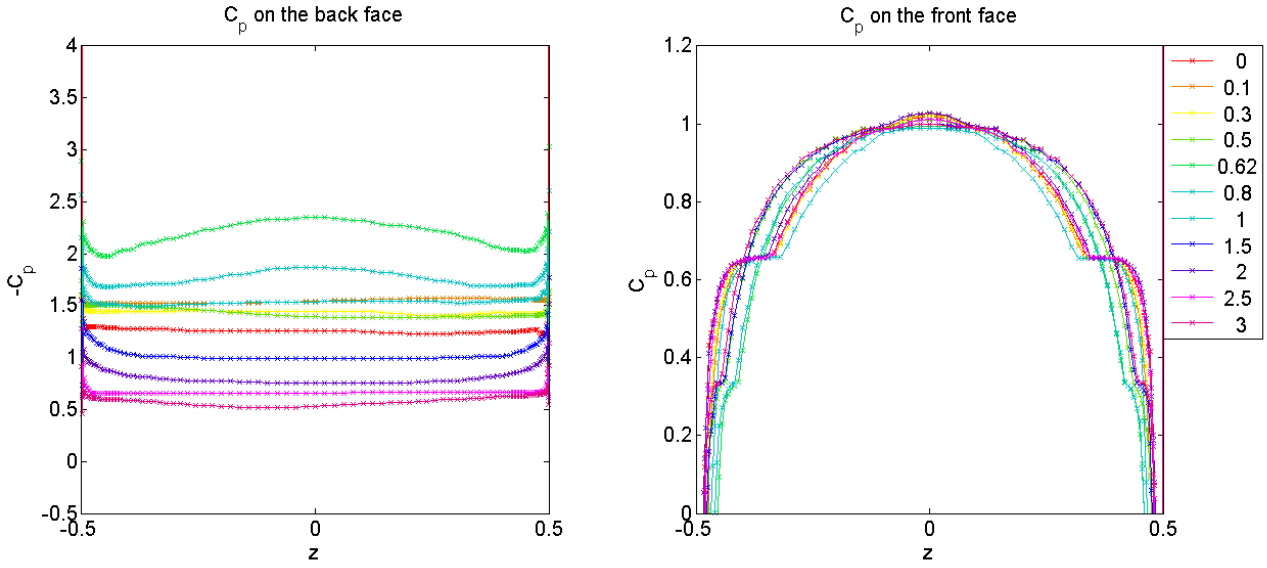

Figure 2.8 3-D simulation results of the pressure coefficient at Re = 20,000.

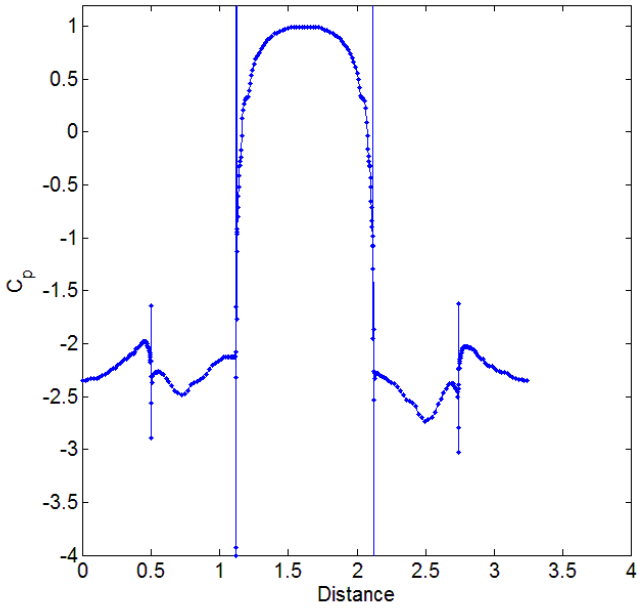

Figure 2.9 Pressure spikes as seen in the corners of a rectangular cylinder. Example is an aspect ratio 0.62 rectangular cylinder with Re = 20,000 using the SST model.

2.5.3 *Square Cylinder at Re = 20,000*

The square cylinder has become a benchmark for turbulent simulations of rectangular cylinders due to available experimental data that is directly comparable to simulation. Thus, it seems appropriate to show a more in-depth look at the results of the square cylinder simulation. The average stream-wise velocity component plotted along the centerline (z = 0) at center span (y = 0) is shown in Fig. 2.10. The simulation selected for the comparison of results was the 3-D simulation using the SST turbulence model. Of the simulations shown, it appears the present calculation is in closest agreement with the experimental results of Lyn et al. However, approximately $2h$ away from the body in the wake, velocity recovery to its free-stream value continues for the present calculation while the experiments of Lyn et al. appear to begin leveling off. This can be attributed to different free-stream conditions at the back end.

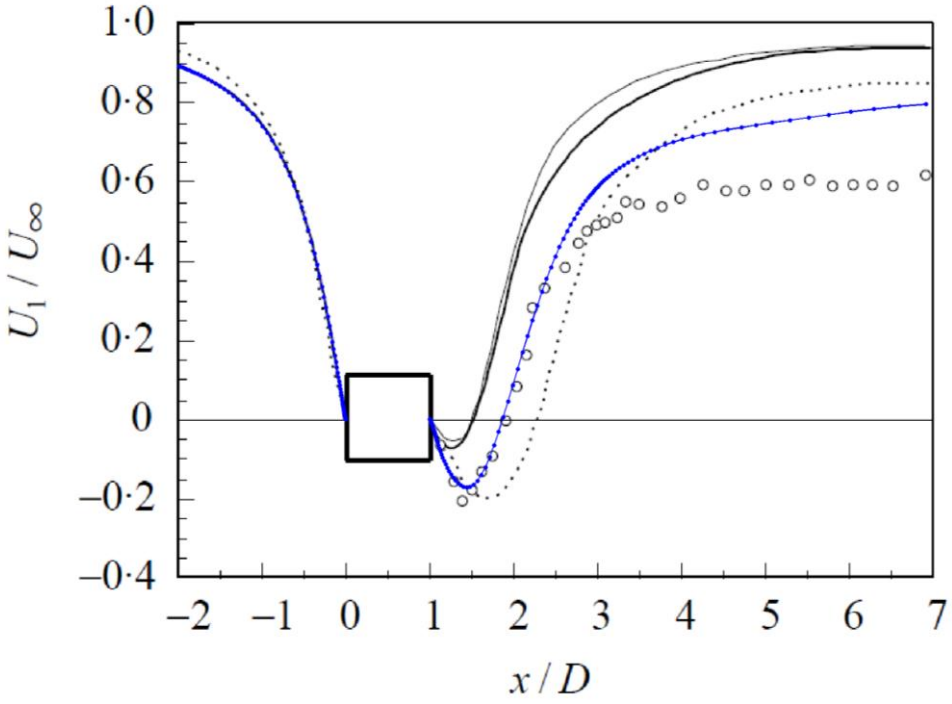

Figure 2.10 Comparison of square cylinder results at Re = 20,000. Present calculation is represented in blue. ‾, Shimada and Ishihara; ‾, Franke and Rodi [23]; ---, Kato and Launder [24]; °, experiment by Lyn [10]. Figure originally appeared in Shimada and Ishihara [9].

2.6 CONCLUSIONS

In this chapter, the results of simulations on rectangular cylinders of varying aspect ratios at a Reynolds number of 20,000 using various turbulence models were presented. In the process of performing the simulations, much was learned about the appropriate assumptions and method to simulating rectangular cylinder. 3-D simulations were found to be in complete agreement with experiment, but 2-D simulations proved to only be in agreement for aspect ratios greater than 0.6. The reasons for the discrepancy between the 2-D simulations and experiment were determined to be the failure of 2-D simulations to resolve motions in the spanwise direction, which was realized through work on circular cylinders by Roshko as well as Williamson [20, 21]. They showed that the two-dimensionality assumption only holds until the Reynolds number is approximately 200, which is 2 orders of magnitude less than the present simulation.

Furthermore, while the force coefficients were in good agreement with the 2-D simulations, there is reason to doubt the flow structures seen in the 2-D simulations. This is substantiated by the simulations of Sohankar, Norberg, and Davidson who performed 2-D and 3-D simulations of square cylinders at Re = 500 [8]. They too found that the drag coefficients calculated from their 2-D and 3-D simulations were in agreement, but that the flow structures were not. Time-averaged streamlines of the 2-D simulation revealed a flow structure that was asymmetric, while the 3-D simulation was not. For the purposes of this dissertation and the intention of discovering the physics of the increase in drag, 2-D simulations were determined to be a poor choice going forward.

Chapter 3. DNS OF RECTANGULAR CYLINDERS AT RE = 500

In this chapter, applying what was learned from the simulations at Re = 20,000, the simulations of rectangular cylinders at Re = 500 were performed. While performing these simulations and up to writing this dissertation, there is no other known collection of simulations or experiments on rectangular cylinders of the aspect ratios specified known to the author. During the literature search, only one set of simulation results for aspect ratio 1 was found.

3.1 MOTIVATION

For the simulations of the Bearman and Trueman experiment at Re = 20,000, a turbulence model was required in order to perform the simulations within a reasonable amount of time. In doing so, it can be said that the results of the simulations are not equivalent to the experiment and when trying to discover something new about the physics of the flow there can be some ambiguity in determining what is driving small scale features. In order to be completely equivalent to experiment, direct numerical simulations (DNS) needed to be performed. Unfortunately, at the Reynolds number of the original experiment, this is unfeasible. However, when the simulations are performed at a much lower Reynolds number, this becomes feasible and much of the more interesting physics of the original experiment can still be retained, such as shed vortices. With the preceding in mind, simulations at Re = 500 were performed.

3.2 GRIDS

Like the simulations presented in the previous chapter, we consider is the grid first. The methodology for making the grids was similar to the previous chapter, with the exception of the normal wall spacing and spacing into the corners. Since the grid was already discussed in great detail, the reader is pointed to Section 2.2. This section will discuss the change in grid spacing and the metrics of the grids.

The reduction in Reynolds number from 20,000 to 500 allows for an increase in the normal wall spacing. Although the spacing could be much larger, the dimensionless normal wall distance was set to 1.0×10^{-4}. This was done in anticipation of simulations to follow, where the rectangular

cylinders will be modified. At the spacing specified, it is small enough to resolve the turbulent boundary layers at the Reynolds number specified in the previous chapter. The spacing going into the corners on the surface of the rectangles was also selected to be 1.0×10^{-4}. In Table 3.1, the number of grid points with respect to aspect ratio is summarized for the simulations performed at Re = 500.

Table 3.1 Number of grid points used in 3-D DNS at Re = 500

Aspect Ratio	**J-Direction Points**	**K-Direction Points**	**L-Direction Points**
0.01	241	53	301
0.2	281	53	301
0.4	301	53	301
0.5	301	53	301
0.62	301	53	301
0.8	301	53	301
1.0	341	53	301

3.3 SIMULATION PARAMETERS

The Reynolds number of the simulation was set to 500 with the free-stream Mach number being set at 0.01. To force asymmetry in the flow, the angle of attack was set to 0.01 degrees, but for this set of simulations the side slip angle was 0 degrees. Again, the other values were left as their default as they appear in the Overflow manual. The laminar flow solver was selected and the non-dimensional time step ta_∞/L was increased to 0.01. The selected numerical methods of solving the problem were set to be the same as the turbulent solutions. The right hand side of the Navier-Stokes equations were solved with Euler central difference terms, while the left hand side of the Navier-Stokes equations were solved using the ARC3D Beam-Warming block tridiagonal scheme.

3.4 RESULTS

In this section, a collection of force coefficient traces and flow images are presented for rectangular cylinders of aspect ratio 0.05, 0.2, 0.4, 0.5, 0.62, 0.8, and 1.0. The results were collected from simulations that were allowed to run until a regular shedding pattern occurred in the force coefficient. The average flow fields were calculated using the last 150,000 iterations or, in normalized time, the last 15 tU_∞/L. Although the averages do not exactly start and end on an oscillation cycle, the number of oscillations used in the calculation provide a sufficient average.

3.4.1 *Aspect Ratio 0.01*

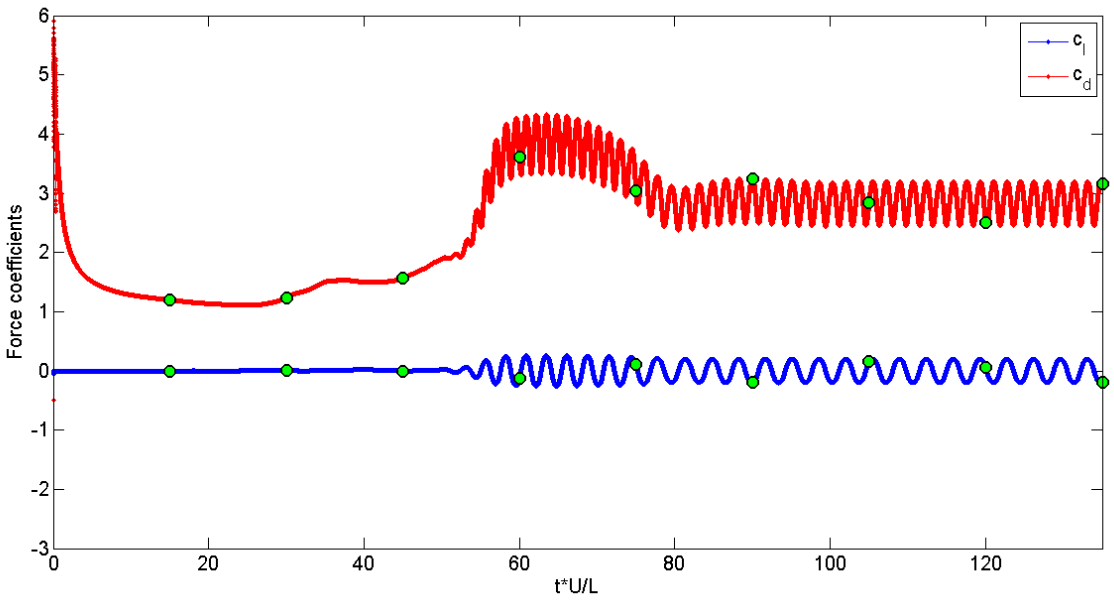

Figure 3.1 Time history for an aspect ratio 0.01 rectangular cylinder. The green dots correspond to times selected for the subsequent time series plots in the following figures (3.2-3.4).

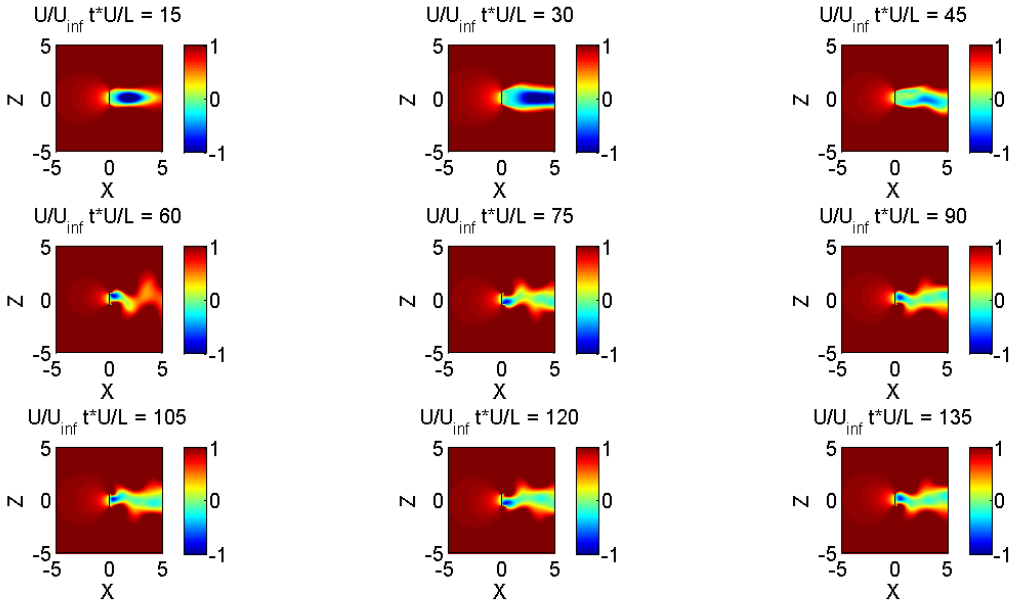

Figure 3.2 Time series of the normalized U velocity for aspect ratio 0.01.Images taken from the x-z plane at y = 0.

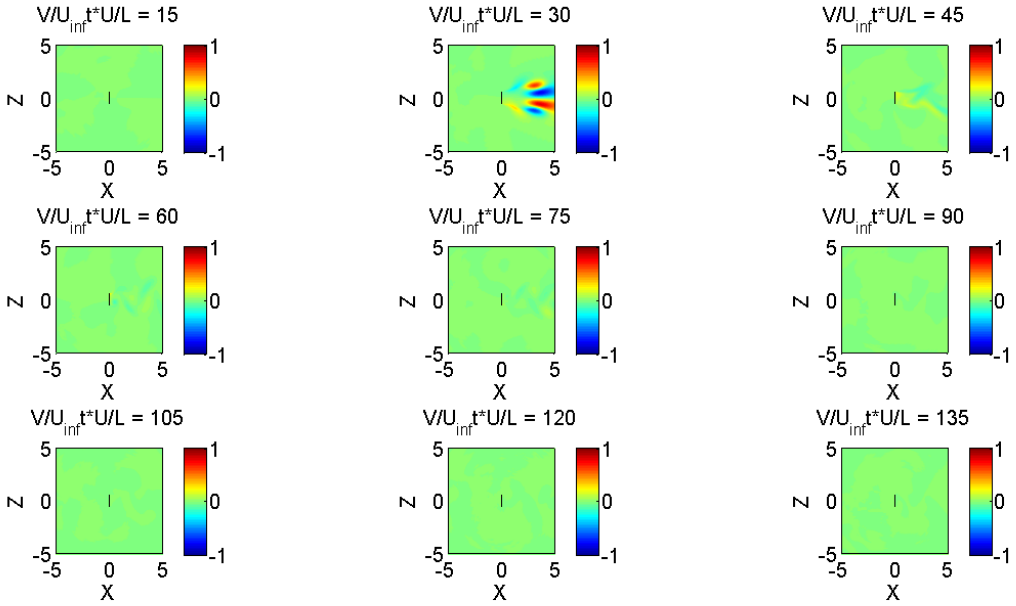

Figure 3.3 Time series of the normalized V velocity for aspect ratio 0.01.Images taken from the x-z plane at y = 0.

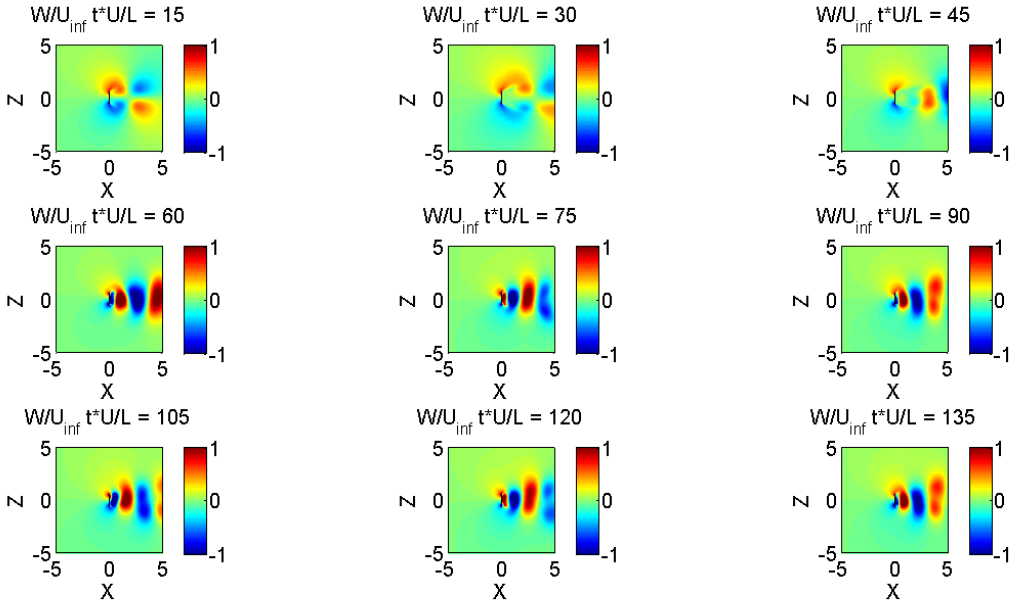

Figure 3.4 Time series of the normalized W velocity for aspect ratio 0.01.Images taken from the x-z plane at y = 0.

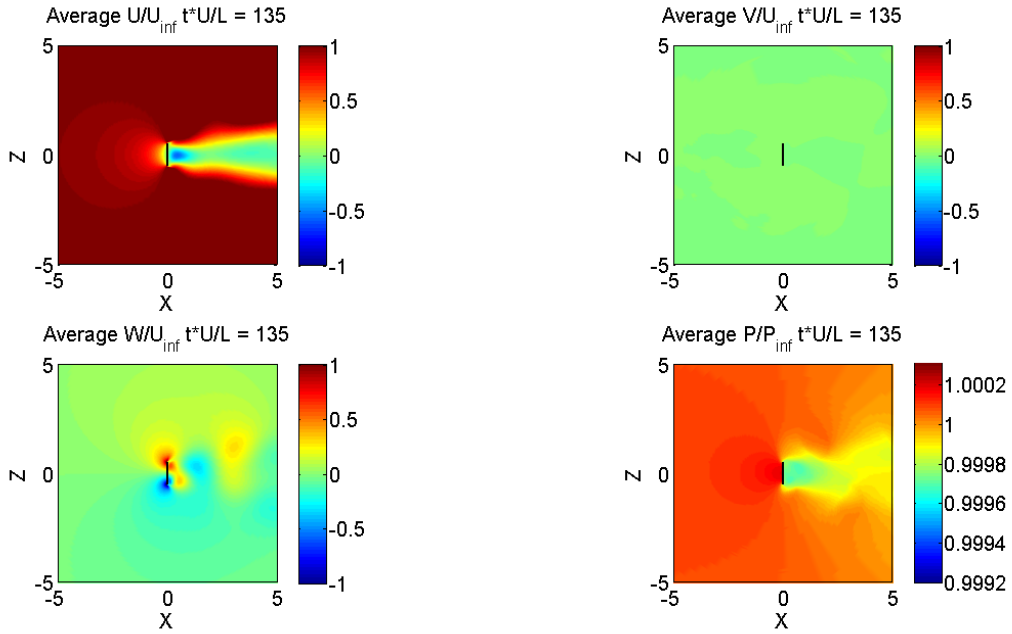

Figure 3.5 Averages of normalized flow quantities for aspect ratio 0.01. Top-left: U/U_∞, Top-right: V/V_∞, Bottom-left: W/W_∞, Bottom-right: P/P_∞. Images taken from the x-z plane at y = 0.

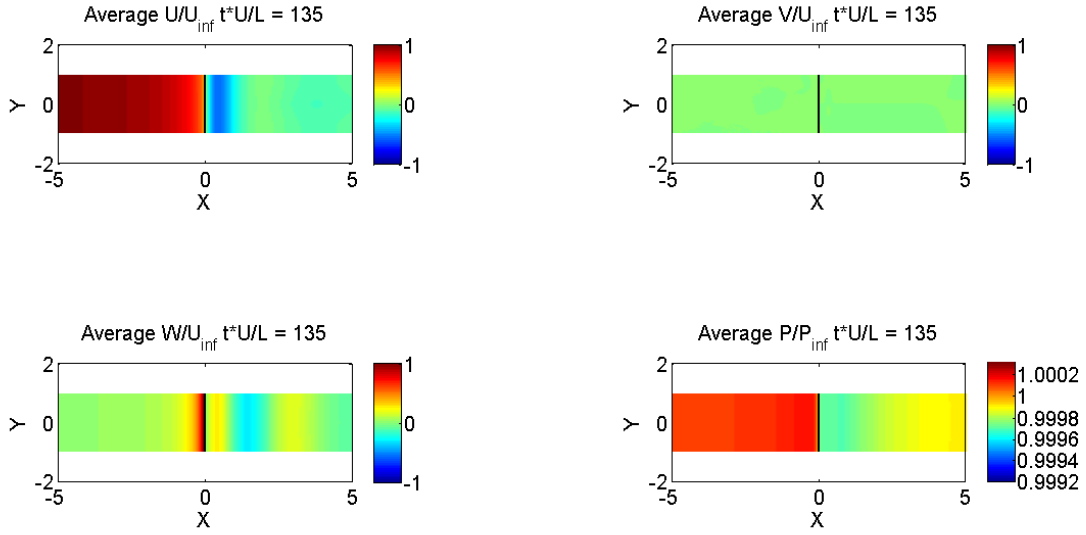

Figure 3.6 Averages of normalized flow quantities for aspect ratio 0.01. Top-left: U/U_∞, Top-right: V/V_∞, Bottom-left: W/W_∞, Bottom-right: P/P_∞. Images taken from the x-y plane at z = 0.

3.4.2 *Aspect Ratio 0.2*

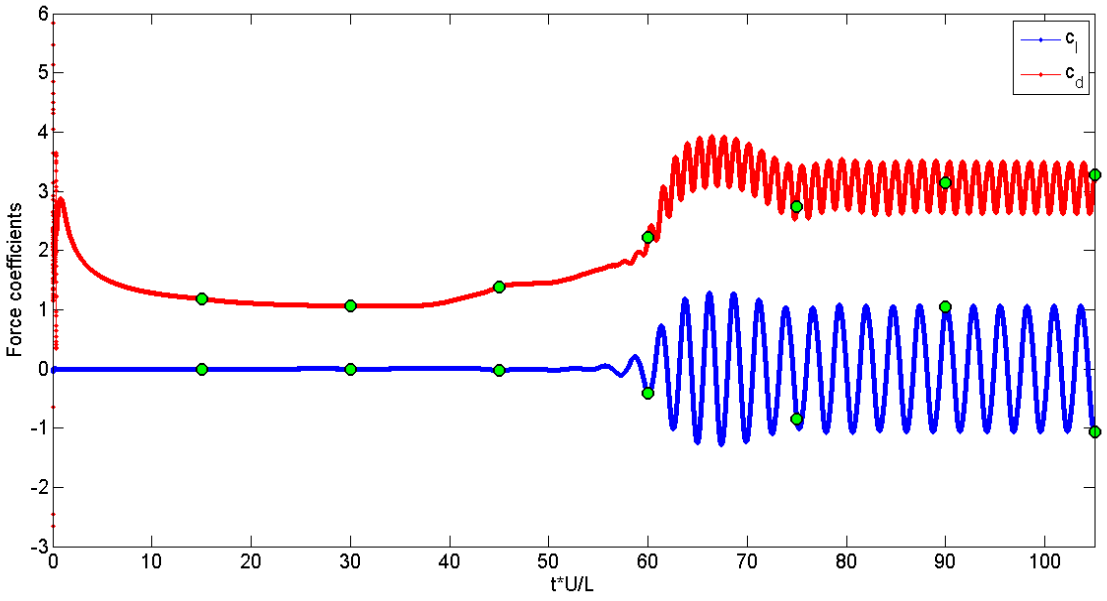

Figure 3.7 Time history for an aspect ratio 0.2 rectangular cylinder. The green dots correspond to times selected for the subsequent time series plots in the following figures (3.8-3.10).

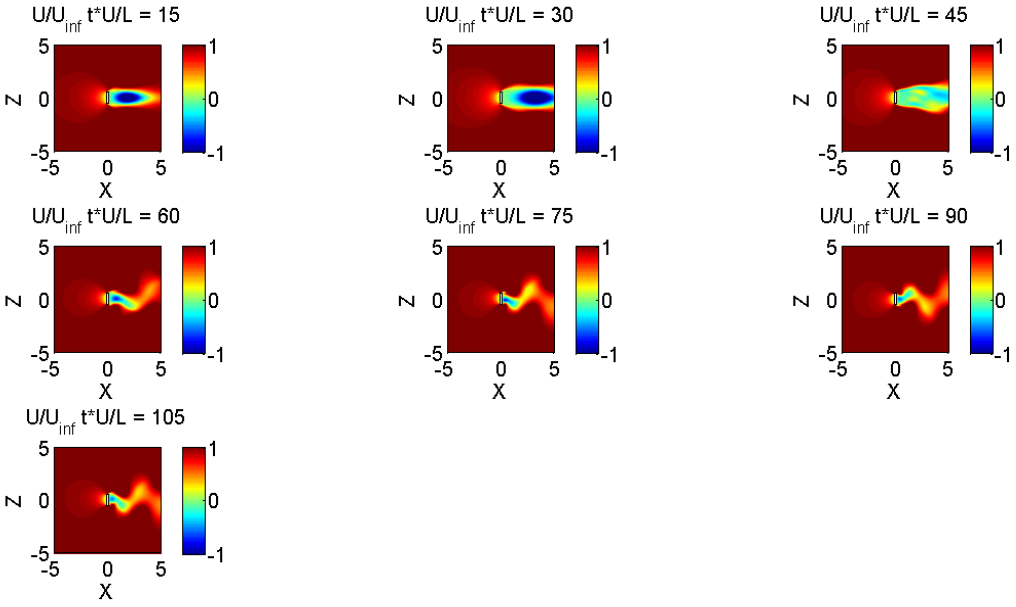

Figure 3.8 Time series of the normalized U velocity for aspect ratio 0.2.Images taken from the x-z plane at y = 0.

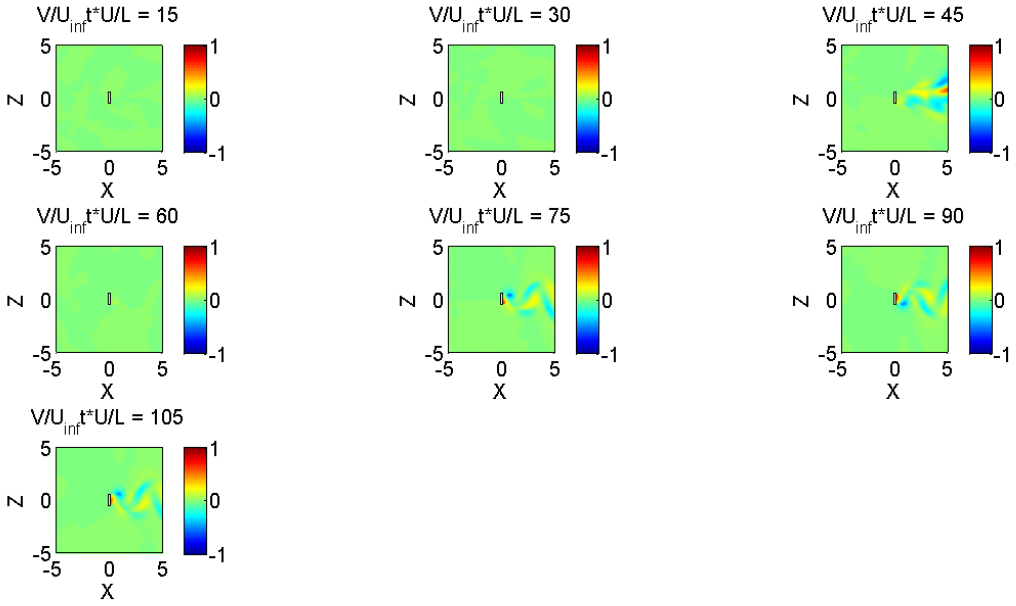

Figure 3.9 Time series of the normalized V velocity for aspect ratio 0.2.Images taken from the x-z plane at y = 0.

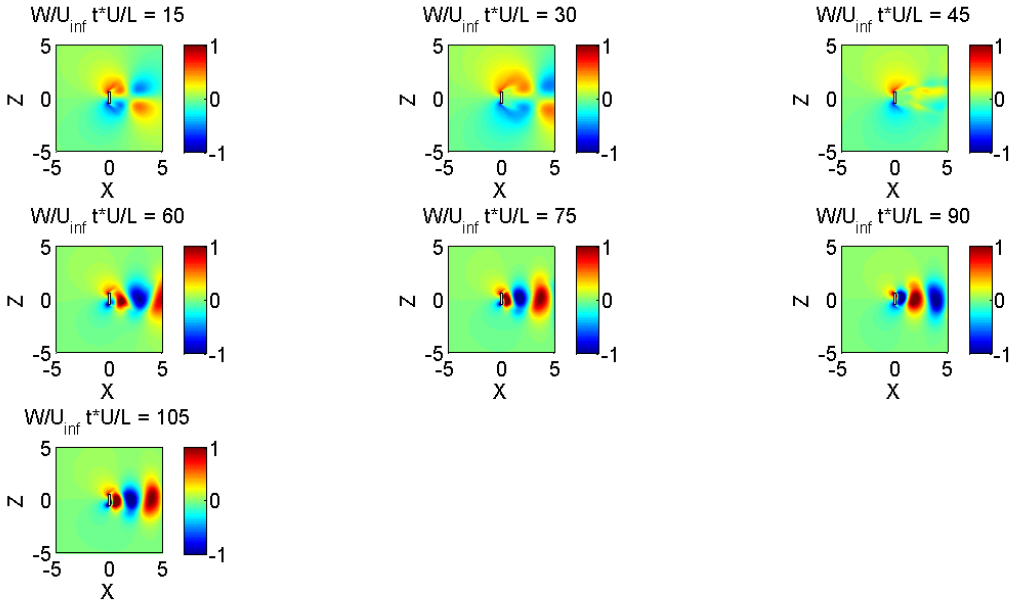

Figure 3.10 Time series of the normalized W velocity for aspect ratio 0.2.Images taken from the x-z plane at y = 0.

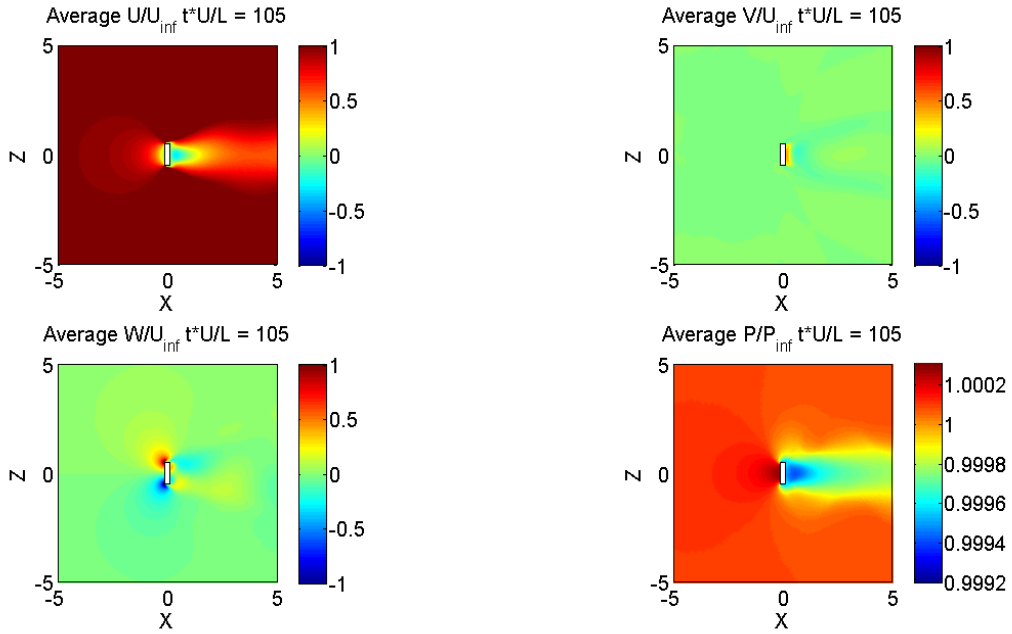

Figure 3.11 Averages of normalized flow quantities for aspect ratio 0.2. Top-left: U/U_∞, Top-right: V/V_∞, Bottom-left: W/W_∞, Bottom-right: P/P_∞. Images taken from the x-z plane at y = 0.

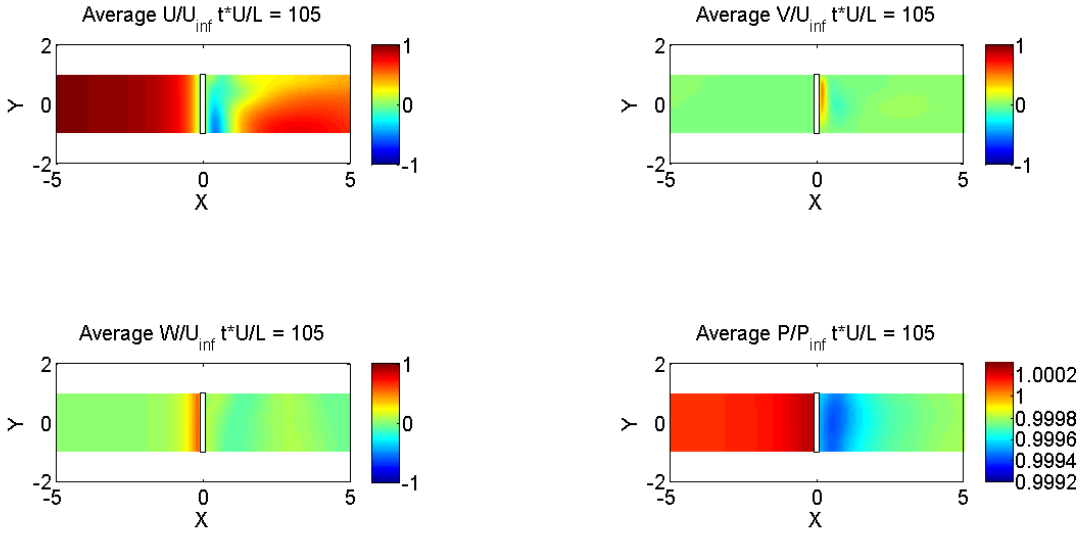

Figure 3.12 Averages of normalized flow quantities for aspect ratio 0.2. Top-left: U/U_∞, Top-right: V/V_∞, Bottom-left: W/W_∞, Bottom-right: P/P_∞. Images taken from the x-y plane at z = 0.

3.4.3 *Aspect Ratio 0.4*

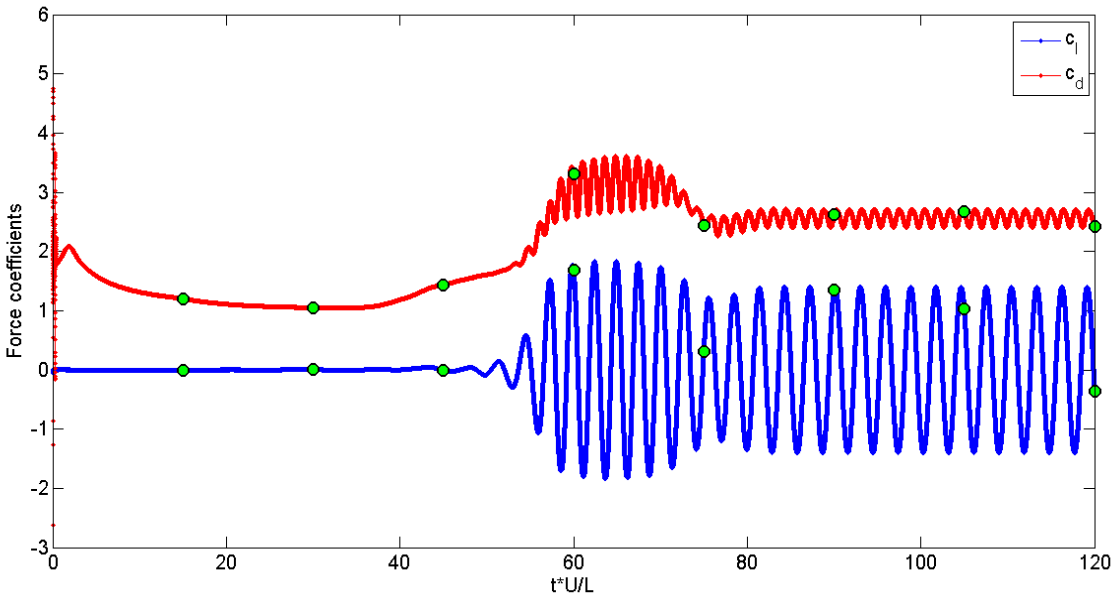

Figure 3.13 Time history for an aspect ratio 0.4 rectangular cylinder. The green dots correspond to times selected for the subsequent time series plots in the following figures (3.14-3.16).

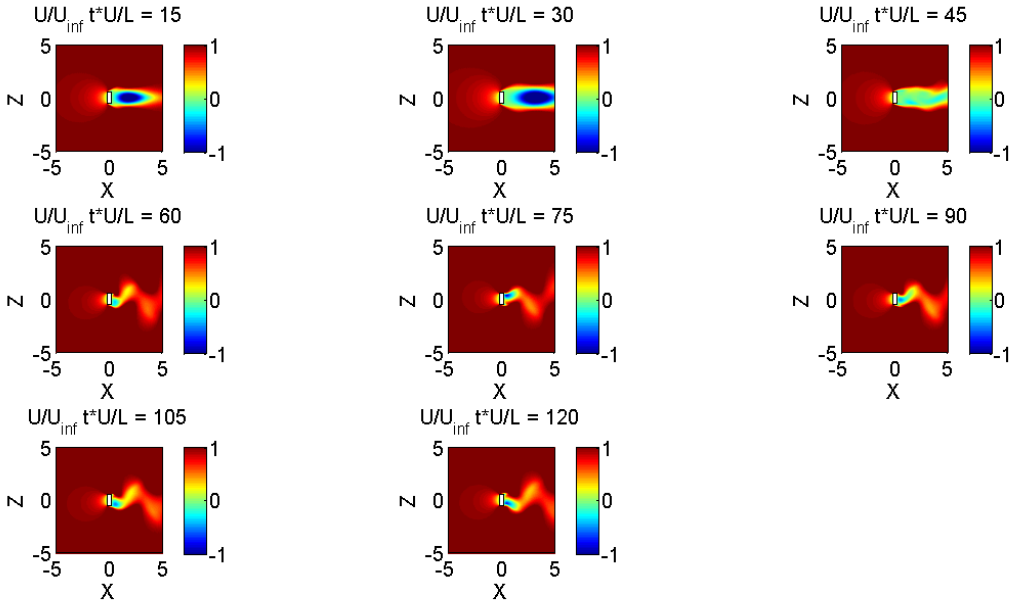

Figure 3.14 Time series of the normalized U velocity for aspect ratio 0.4.Images taken from the x-z plane at y = 0.

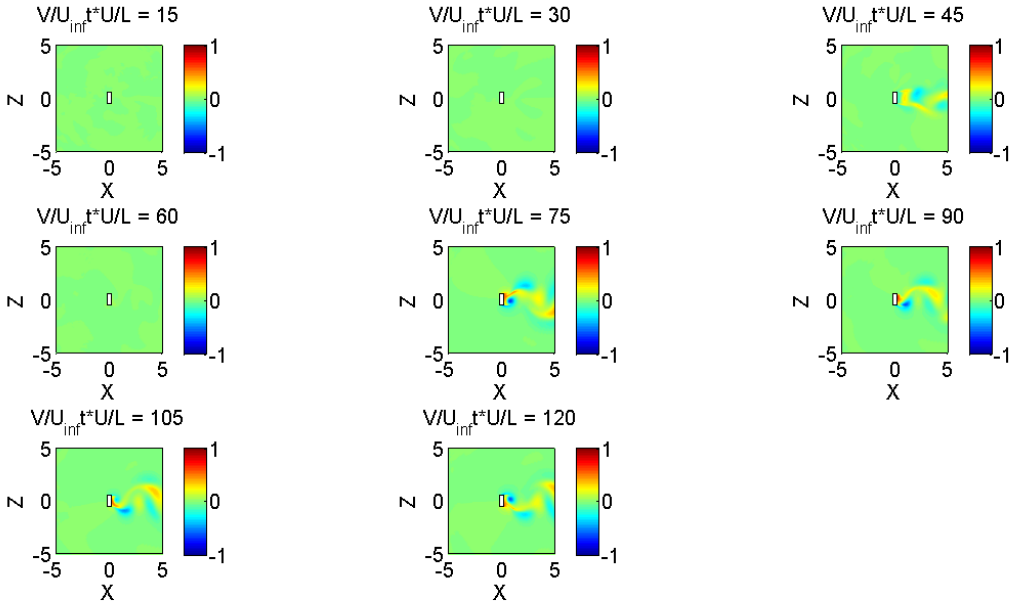

Figure 3.15 Time series of the normalized V velocity for aspect ratio 0.4.Images taken from the x-z plane at y = 0.

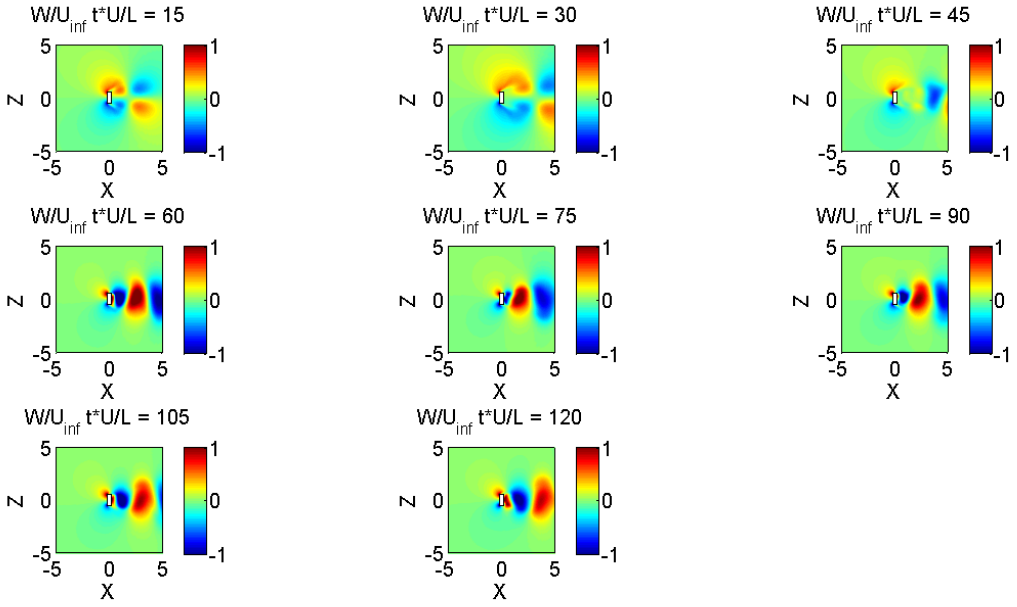

Figure 3.16 Time series of the normalized W velocity for aspect ratio 0.4.Images taken from the x-z plane at y = 0.

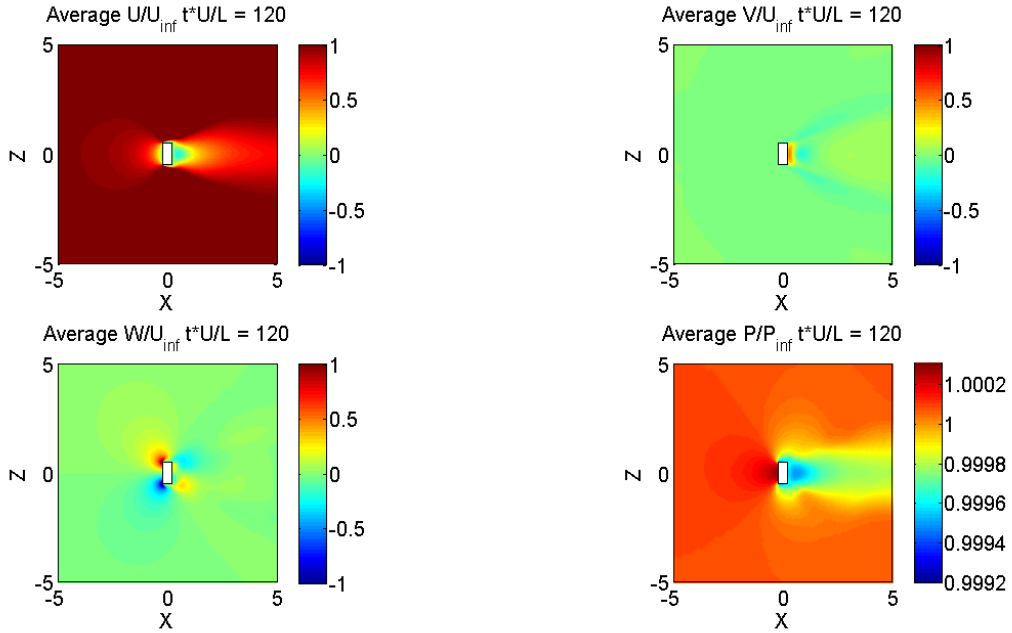

Figure 3.17 Averages of normalized flow quantities for aspect ratio 0.4. Top-left: U/U_∞, Top-right: V/V_∞, Bottom-left: W/W_∞, Bottom-right: P/P_∞. Images taken from the x-z plane at y = 0.

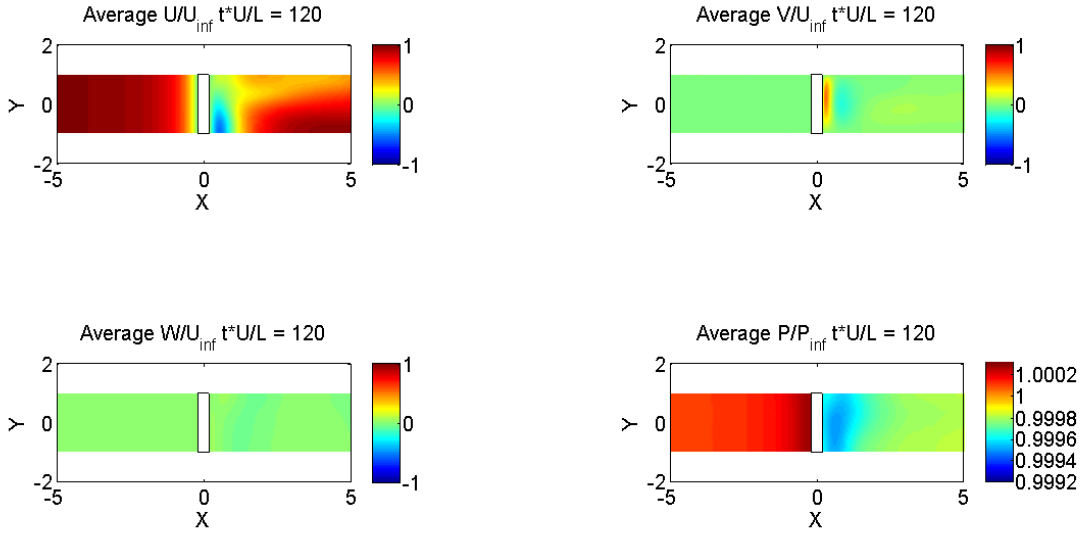

Figure 3.18 Averages of normalized flow quantities for aspect ratio 0.4. Top-left: U/U_∞, Top-right: V/V_∞, Bottom-left: W/W_∞, Bottom-right: P/P_∞. Images taken from the x-y plane at z = 0.

3.4.4 *Aspect Ratio 0.5*

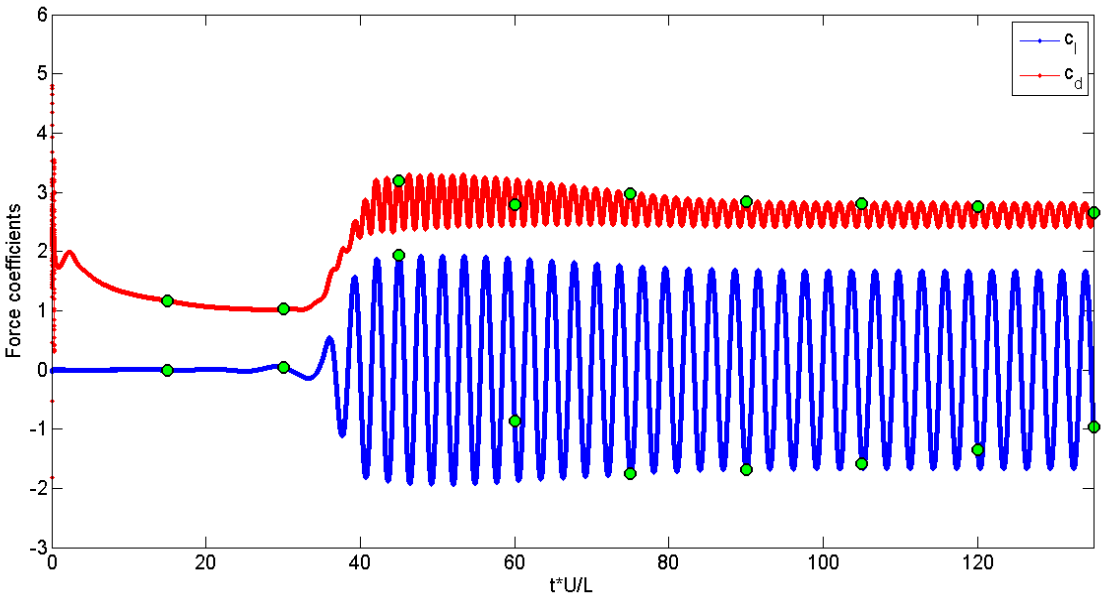

Figure 3.19 Time history for an aspect ratio 0.5 rectangular cylinder.The green dots correspond to times selected for the subsequent time series plots in the following figures (3.20-3.22).

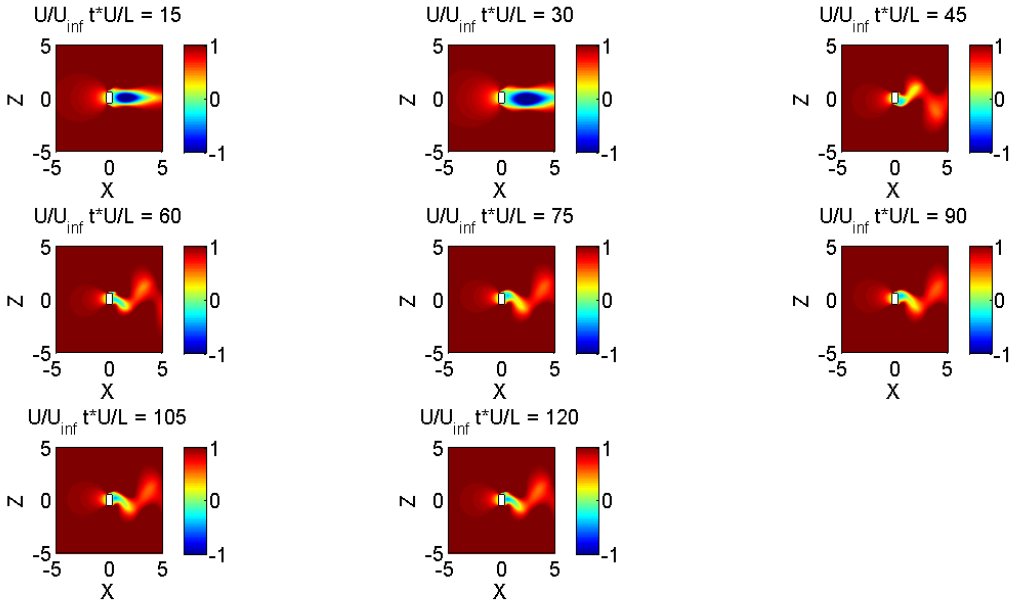

Figure 3.20 Time series of the normalized U velocity for aspect ratio 0.5.Images taken from the x-z plane at y = 0.

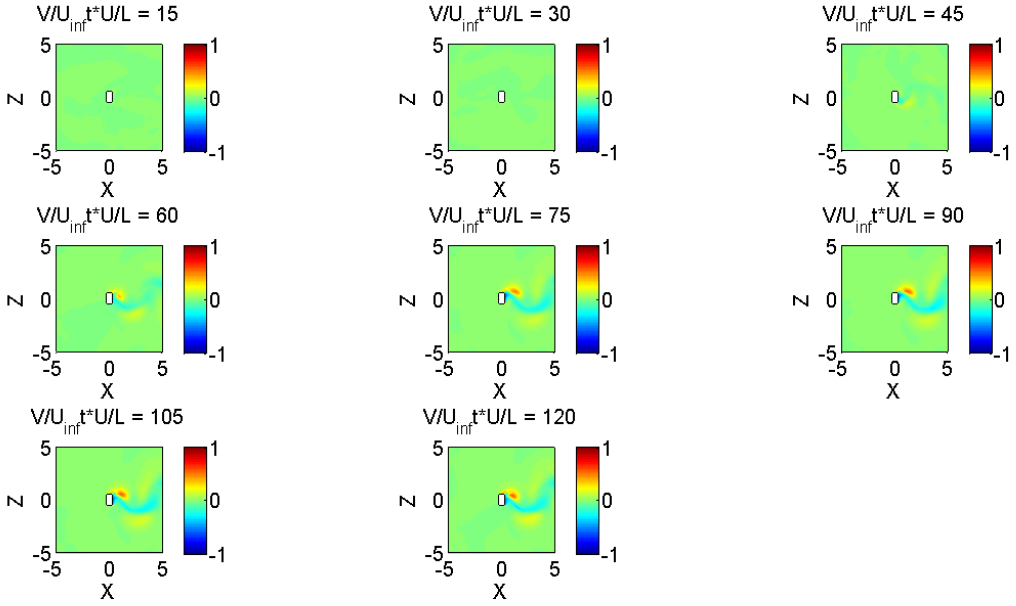

Figure 3.21 Time series of the normalized V velocity for aspect ratio 0.5. Images taken from the x-z plane at y = 0.

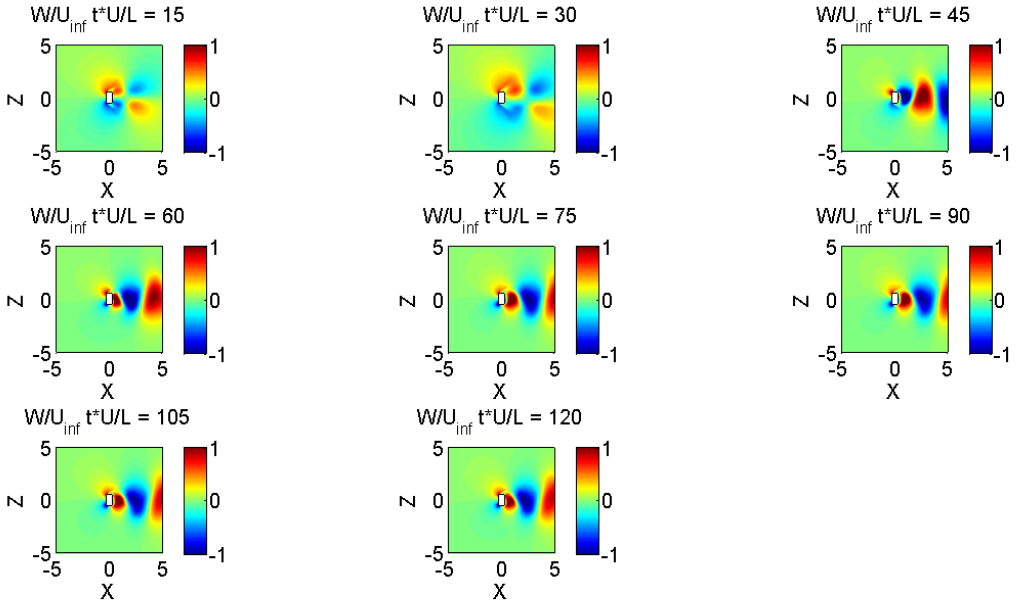

Figure 3.22 Time series of the normalized W velocity for aspect ratio 0.5. Images taken from the x-z plane at y = 0.

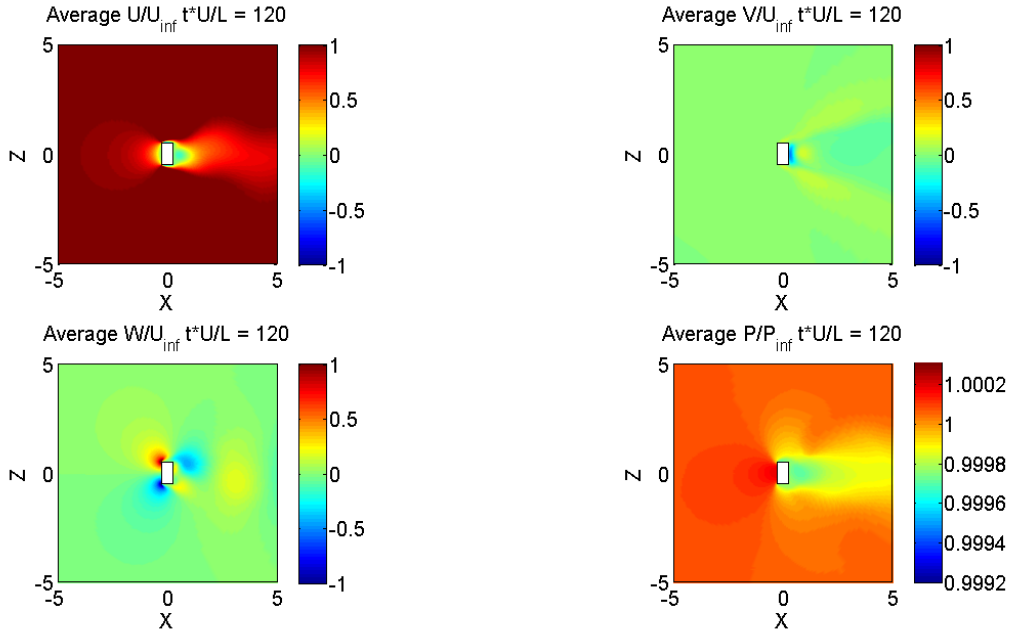

Figure 3.23 Averages of normalized flow quantities for aspect ratio 0.5. Top-left: U/U_∞, Top-right: V/V_∞, Bottom-left: W/W_∞, Bottom-right: P/P_∞. Images taken from the x-z plane at y = 0.

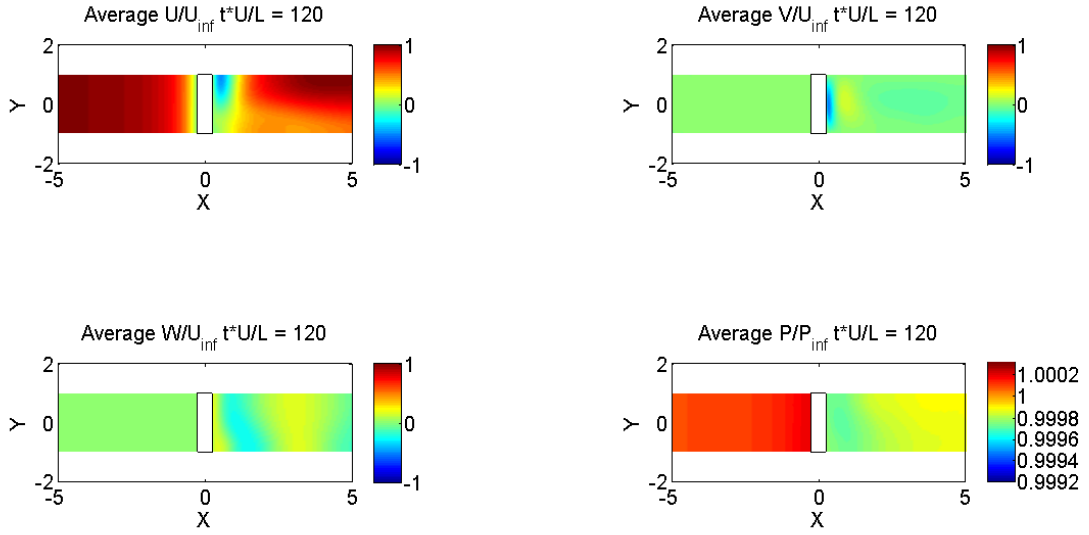

Figure 3.24 Averages of normalized flow quantities for aspect ratio 0.5. Top-left: U/U_∞, Top-right: V/V_∞, Bottom-left: W/W_∞, Bottom-right: P/P_∞. Images taken from the x-y plane at z = 0.

3.4.5 *Aspect Ratio 0.62*

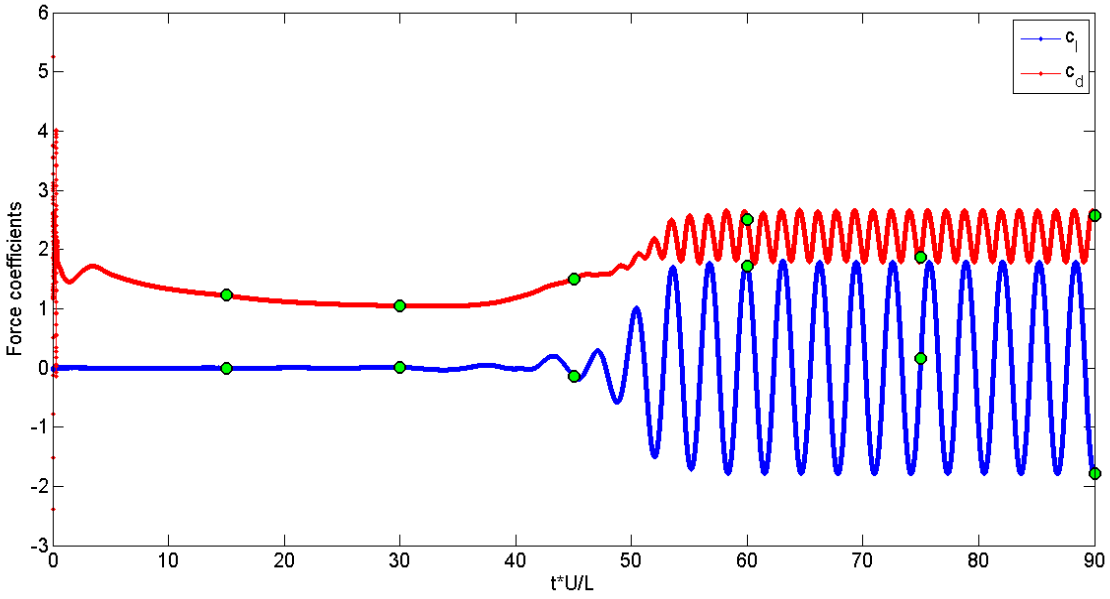

Figure 3.25 Time history for an aspect ratio 0.62 rectangular cylinder.The green dots correspond to times selected for the subsequent time series plots in the following figures (3.26-3.28).

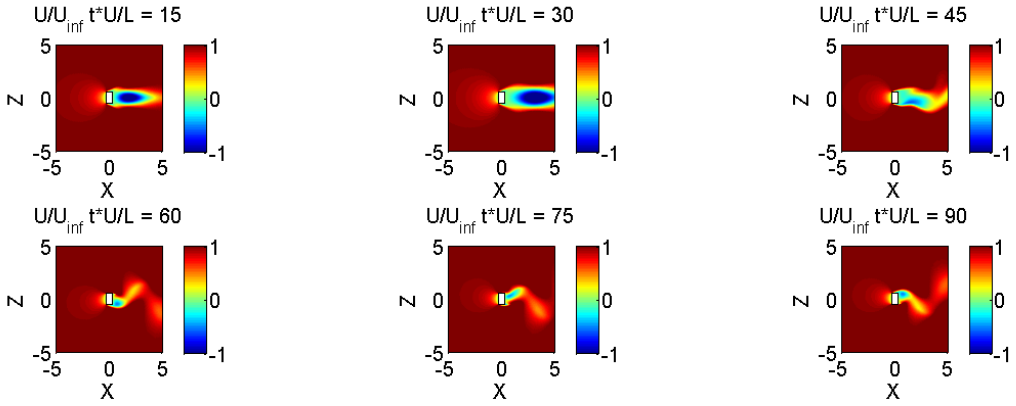

Figure 3.26 Time series of the normalized U velocity for aspect ratio 0.6.Images taken from the x-z plane at y = 0.

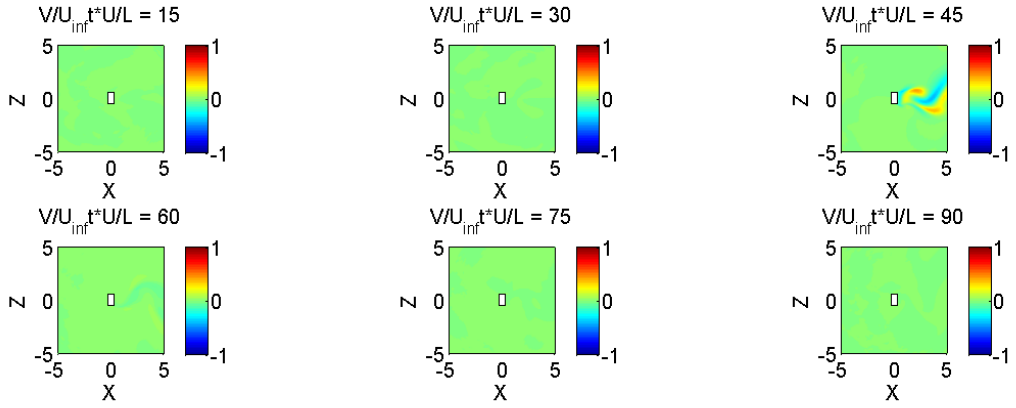

Figure 3.27 Time series of the normalized V velocity for aspect ratio 0.62.Images taken from the x-z plane at y = 0.

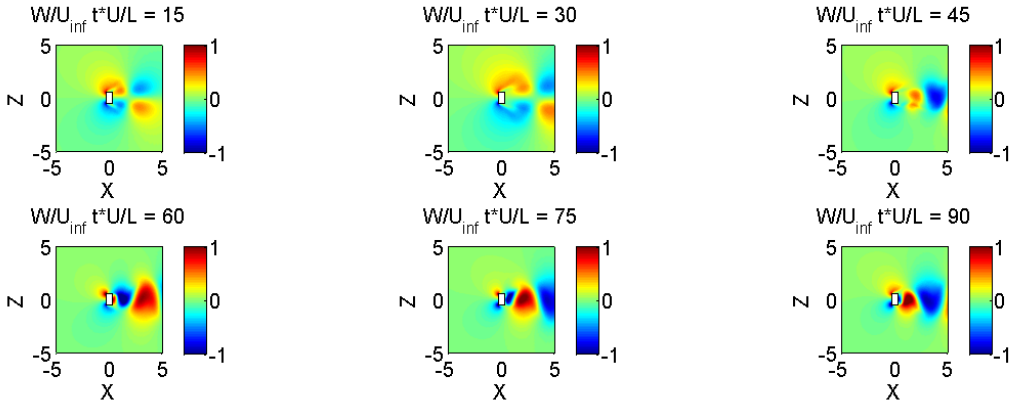

Figure 3.28 Time series of the normalized W velocity for aspect ratio 0.62.Images taken from the x-z plane at y = 0.

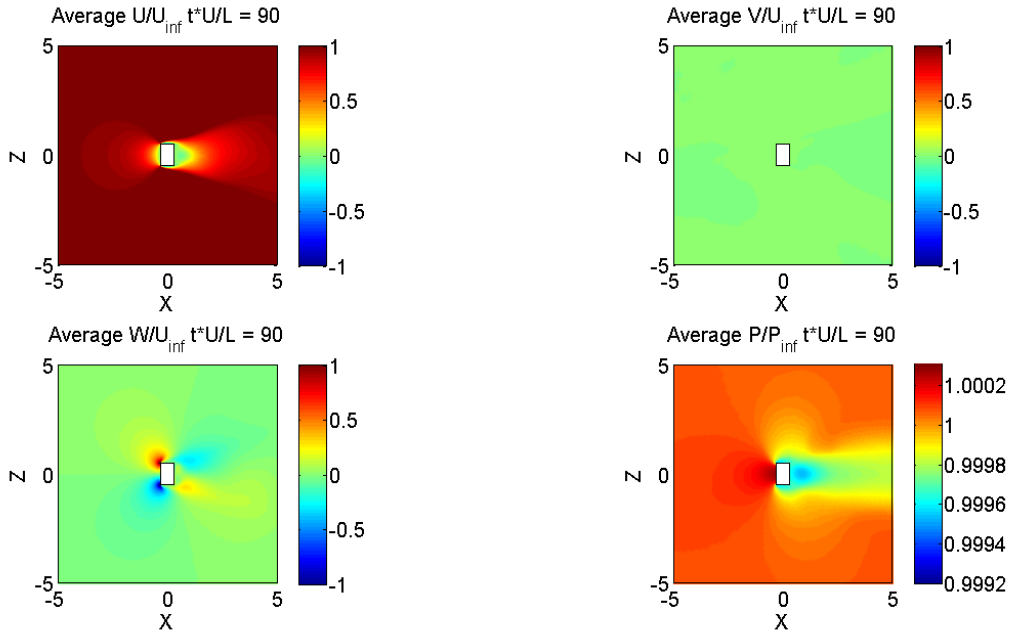

Figure 3.29 Averages of normalized flow quantities for aspect ratio 0.62. Top-left: U/U_∞, Top-right: V/V_∞, Bottom-left: W/W_∞, Bottom-right: P/P_∞. Images taken from the x-z plane at y = 0.

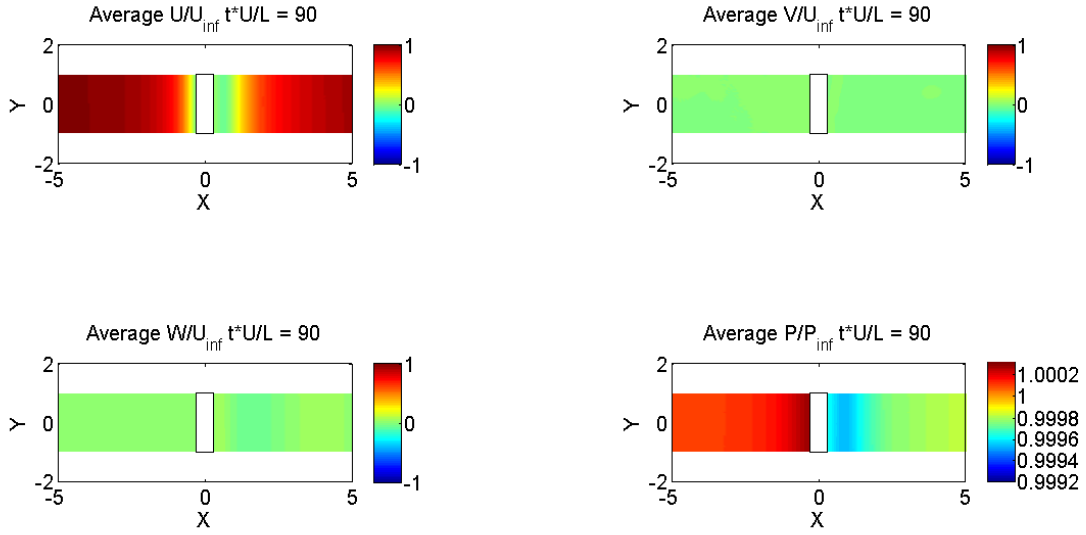

Figure 3.30 Averages of normalized flow quantities for aspect ratio 0.62. Top-left: U/U_∞, Top-right: V/V_∞, Bottom-left: W/W_∞, Bottom-right: P/P_∞. Images taken from the x-y plane at z = 0.

3.4.6 *Aspect Ratio 0.8*

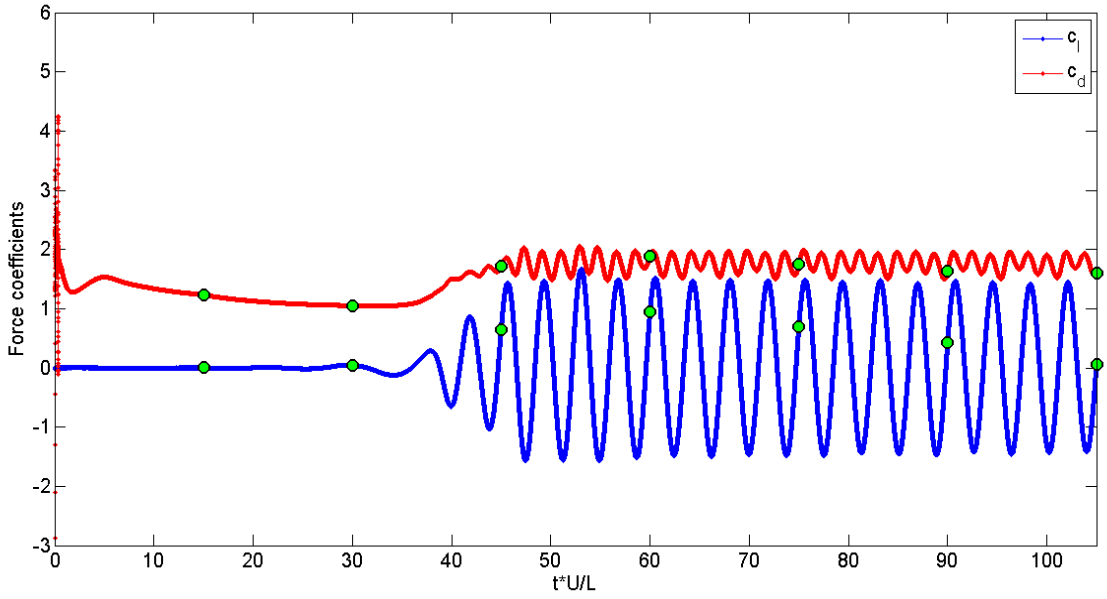

Figure 3.31 Time history for an aspect ratio 0.8 rectangular cylinder. The green dots correspond to times selected for the subsequent time series plots in the following figures (3.32-3.34).

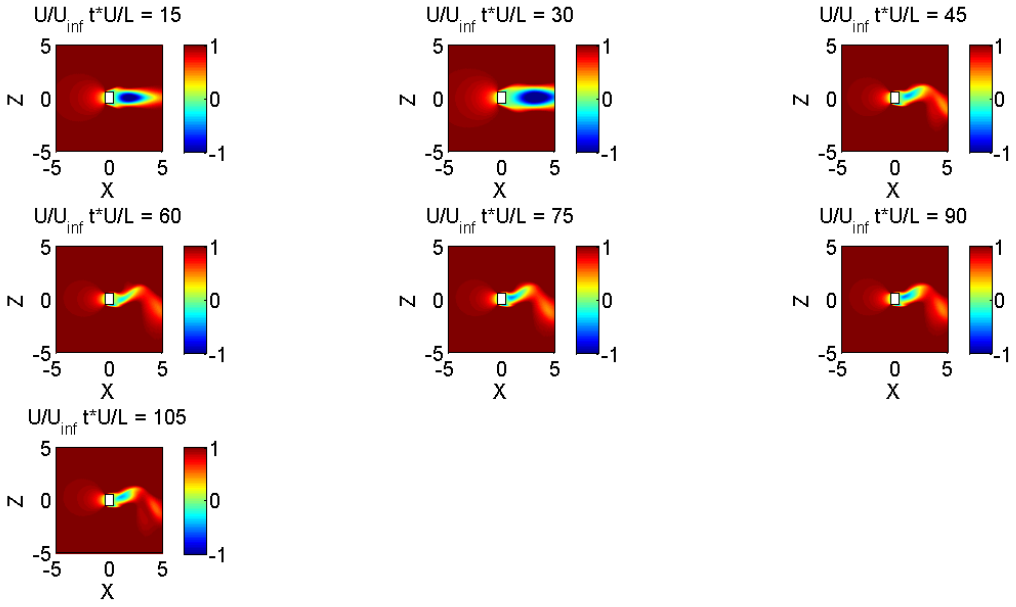

Figure 3.32 Time series of the normalized U velocity for aspect ratio 0.8.Images taken from the x-z plane at y = 0.

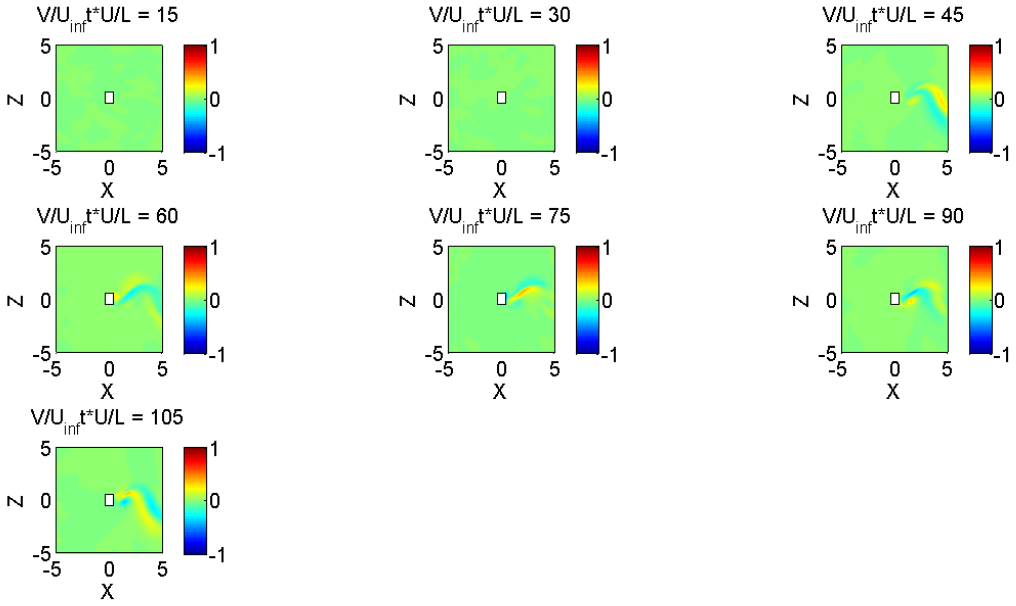

Figure 3.33 Time series of the normalized V velocity for aspect ratio 0.8.Images taken from the x-z plane at y = 0.

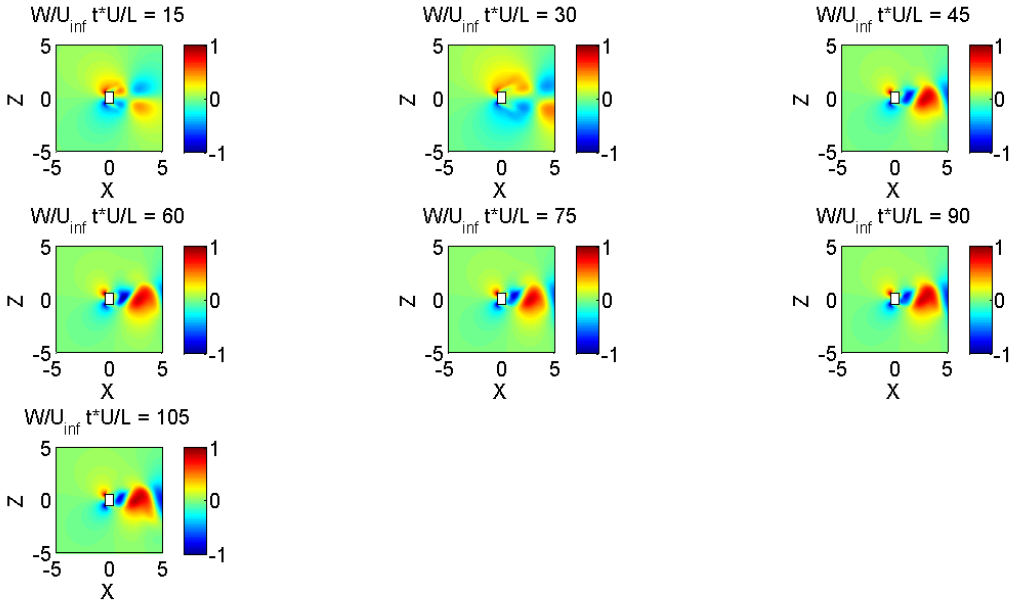

Figure 3.34 Time series of the normalized W velocity for aspect ratio 0.8.Images taken from the x-z plane at y = 0.

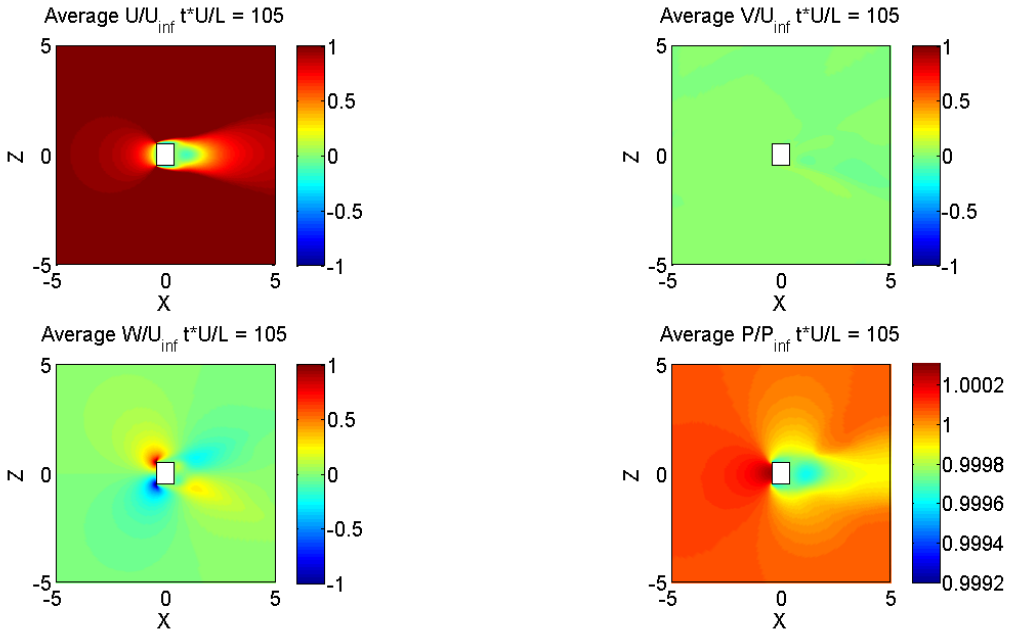

Figure 3.35 Averages of normalized flow quantities for aspect ratio 0.8. Top-left: U/U_∞, Top-right: V/V_∞, Bottom-left: W/W_∞, Bottom-right: P/P_∞. Images taken from the x-z plane at y = 0.

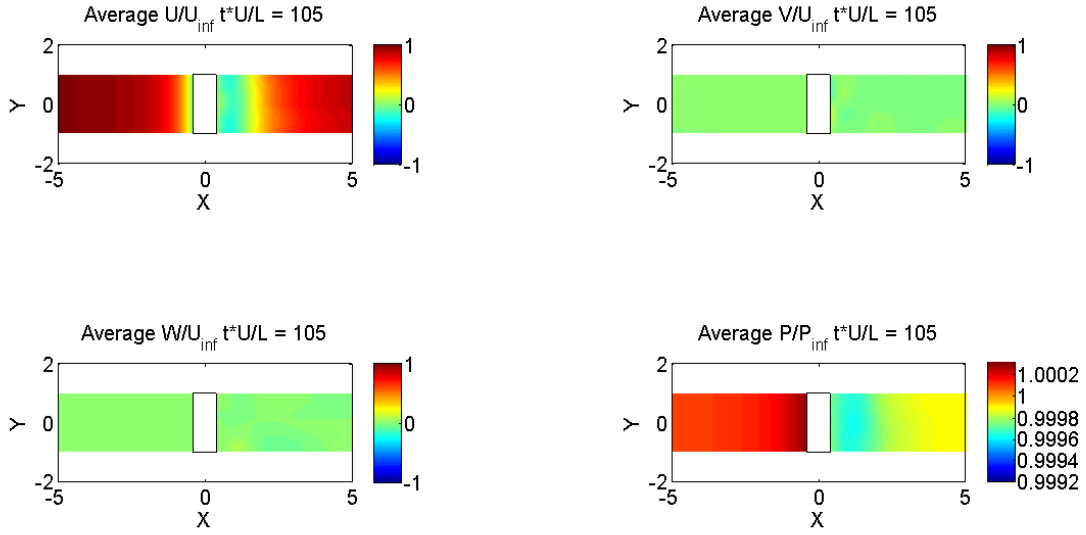

Figure 3.36 Averages of normalized flow quantities for aspect ratio 0.8. Top-left: U/U_∞, Top-right: V/V_∞, Bottom-left: W/W_∞, Bottom-right: P/P_∞. Images taken from the x-y plane at z = 0.

3.4.7 *Aspect Ratio 1.0*

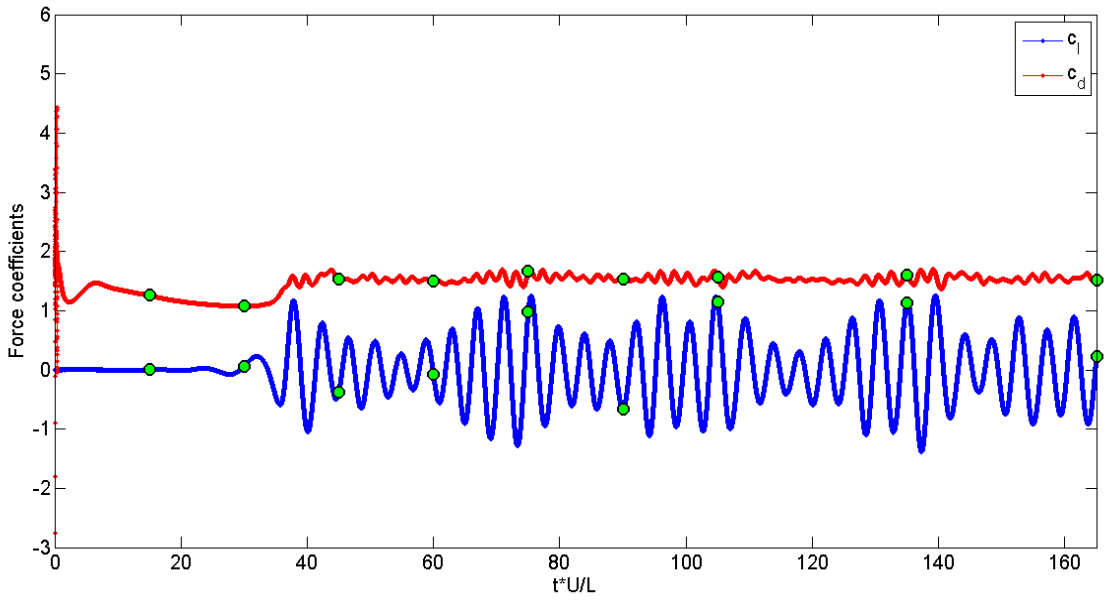

Figure 3.37 Time history for an aspect ratio 1.0 rectangular cylinder. The green dots correspond to times selected for the subsequent time series plots in the following figures (3.38-3.40).

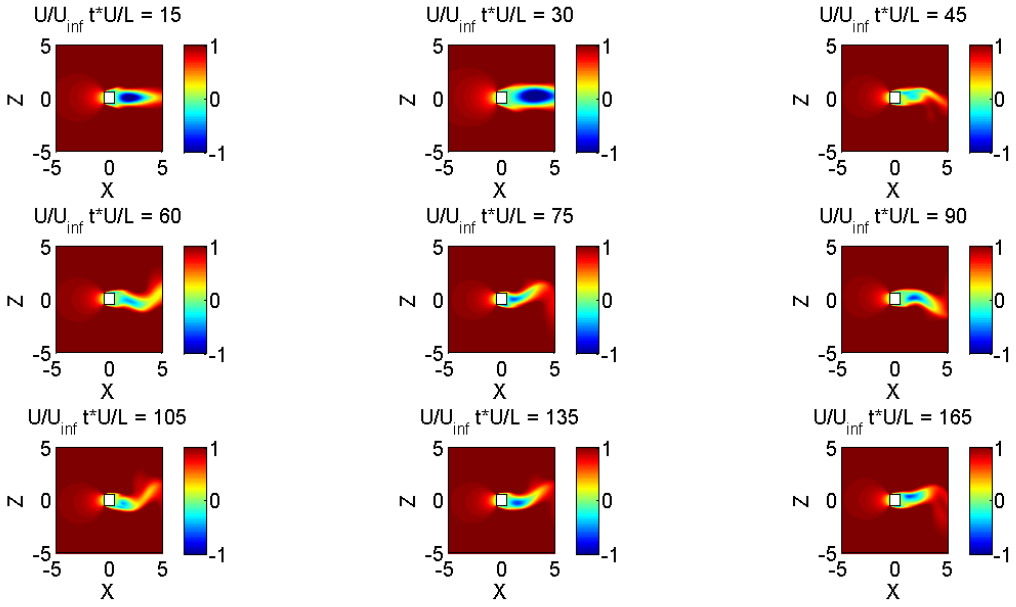

Figure 3.38 Time series of the normalized U velocity for aspect ratio 1.0.Images taken from the x-z plane at y = 0.

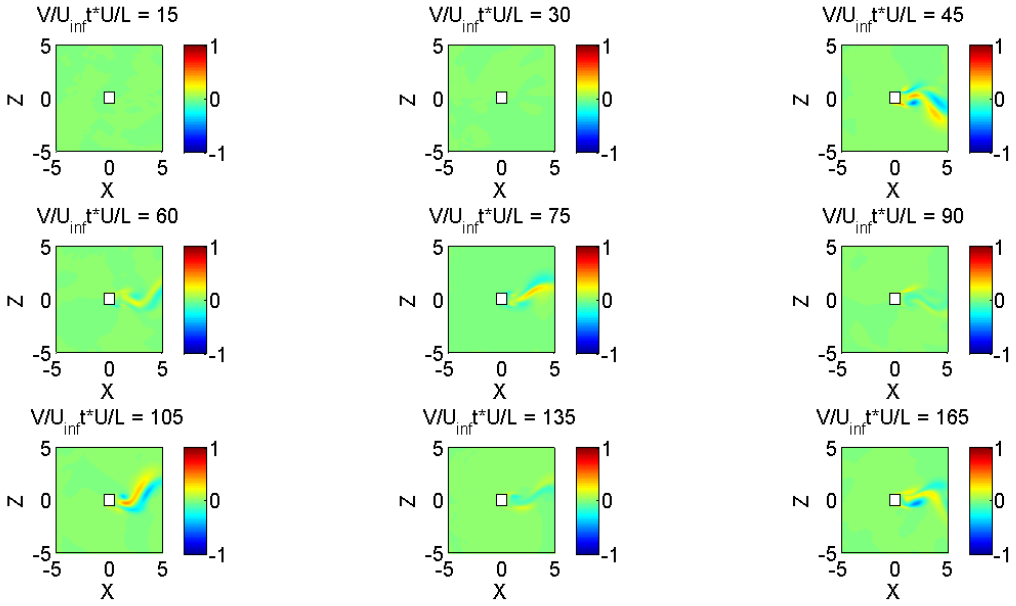

Figure 3.39 Time series of the normalized V velocity for aspect ratio 1.0.Images taken from the x-z plane at y = 0.

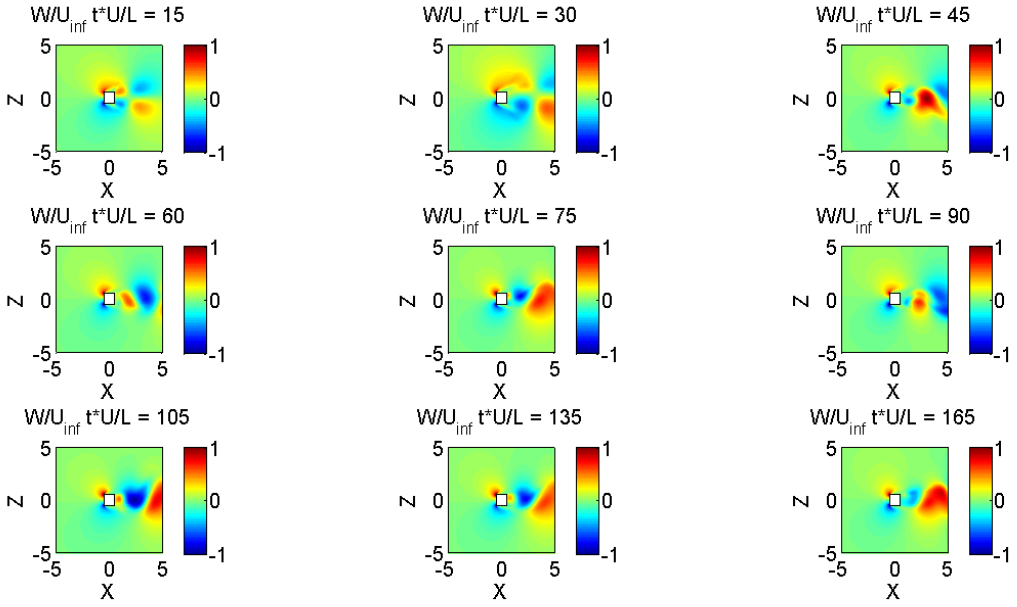

Figure 3.40 Time series of the normalized W velocity for aspect ratio 1.0.Images taken from the x-z plane at y = 0.

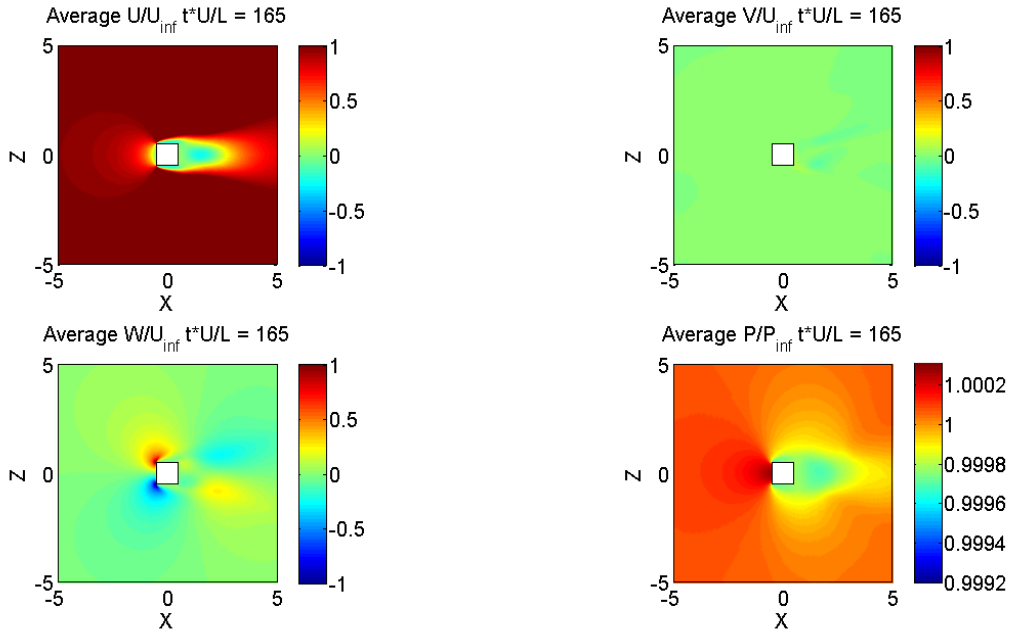

Figure 3.41 Averages of normalized flow quantities for aspect ratio 1.0. Top-left: U/U_∞, Top-right: V/V_∞, Bottom-left: W/W_∞, Bottom-right: P/P_∞. Images taken from the x-z plane at y = 0.

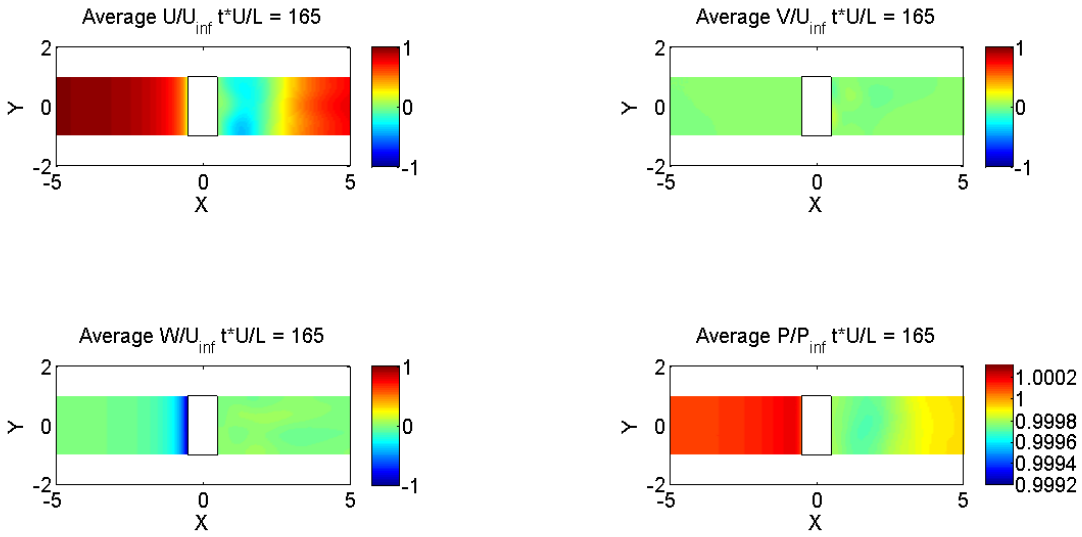

Figure 3.42 Averages of normalized flow quantities for aspect ratio 1.0. Top-left: U/U_∞, Top-right: V/V_∞, Bottom-left: W/W_∞, Bottom-right: P/P_∞. Images taken from the x-y plane at z = 0.

3.5 Analysis and Discussion

Using the results shown in Section 3.4, the mean drag coefficient, Strouhal number, and other flow quantities of interest are calculated. In addition, discussion of the mechanism which causes the increase in drag is discussed and observations of the spanwise flow and its relationship to the drag peak are discussed.

3.5.1 *Mean Drag Coefficient*

The mean drag coefficient was calculated using the time histories of the force coefficients shown in Section 3.5.2. The integration output program was set to record every 10th data point and the mean was taken using output of the last 150,000 iterations, or in non-dimensional time units 15 tU_∞/L. The results of this are summarized in Table 3.2 and Fig. 3.43.

The simulations of rectangular cylinders show that a peak in the drag coefficient still exists at Re = 500. However, the peak has shifted from an aspect ratio of 0.62 at Re = 20,000 to an aspect ratio of 0.2 at Re = 500. Unlike the Bearman and Trueman experiment, the mean drag does not monotonically increase to the peak then monotonically decrease. Instead, the drag coefficient increases to a peak at aspect ratio 0.2, decreases, then again increases at aspect ratio 0.5 before continuing to decrease for the remainder of the aspect ratios simulated. In a subsequent section, the drag increase will be discussed in further detail and the mechanics behind it.

Table 3.2 Drag coefficient vs. aspect ratio for rectangular cylinders at Re = 500

Aspect Ratio	Mean Drag Coefficient
0.01	2.861
0.2	3.093
0.4	2.569
0.5	2.636
0.62	2.259
0.8	1.767
1.0	1.544

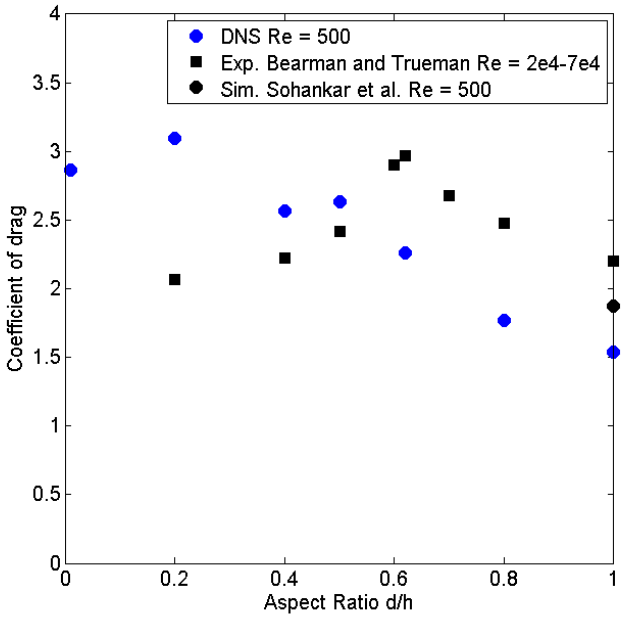

Figure 3.43 Drag coefficient vs. aspect ratio for rectangular cylinders at Re = 500. Experimental data from Bearman and Trueman as well as the simulation result from Sohankar, Norberg, and Davidson are shown [2, 8].

3.5.2 *Strouhal Number*

The Strouhal number was calculated using the time history of the force coefficients seen in Figs. 3.44 – 3.50. The power spectra corresponding to each time history is also shown from which the Strouhal number of each aspect ratio was determined. The power spectras as determined by the lift and drag coefficients are provided. For the majority of the aspect ratios tested, the lift coefficient provided much larger values in the power spectra. The results of the Strouhal number calculations can be seen summarized in Table 3.3 and Fig. 3.51.

For the sake of completeness, the relationship between vortex shedding, the drag coefficient and the lift coefficient was determined to be:

$$f_s = \frac{f_L}{2} = \frac{f_D}{4} \tag{3.1}$$

where f_L is the frequency of the lift coefficient and f_D is the frequency of the drag coefficient.

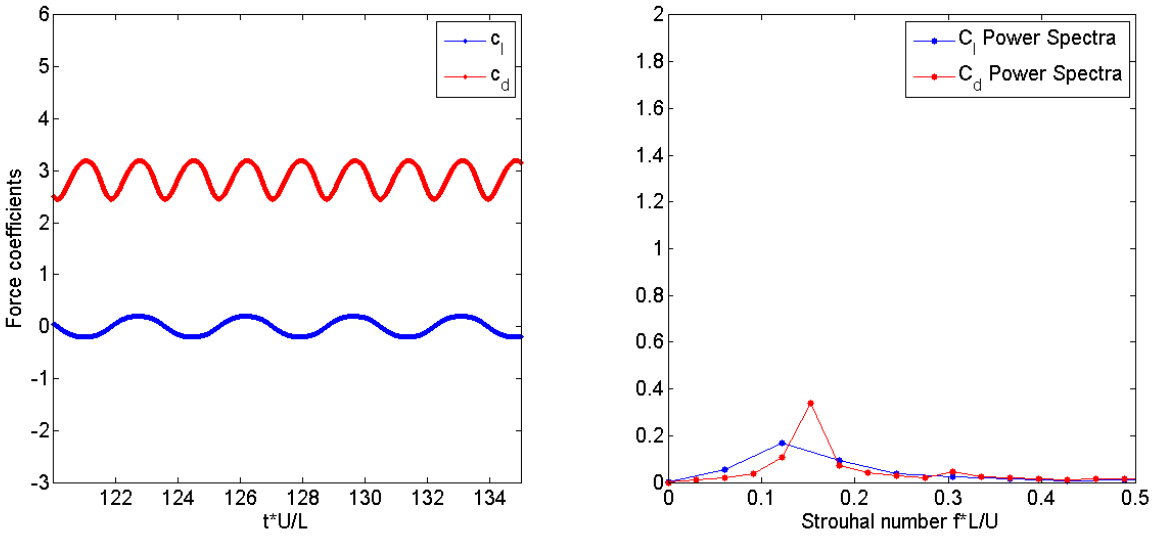

Figure 3.44 Time history and power spectra for aspect ratio 0.01

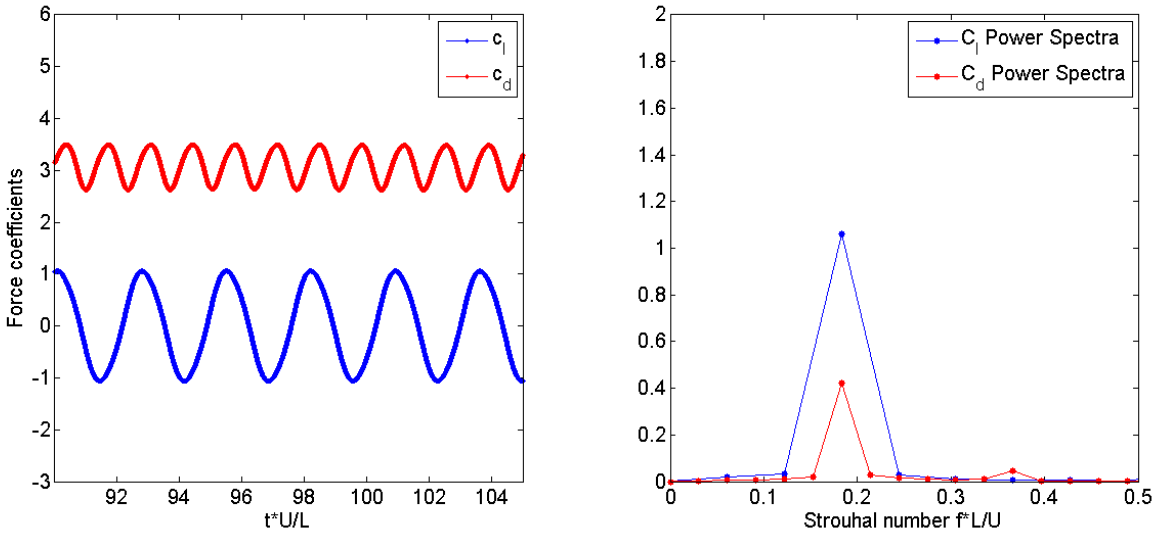

Figure 3.45 Time history and power spectra for aspect ratio 0.2

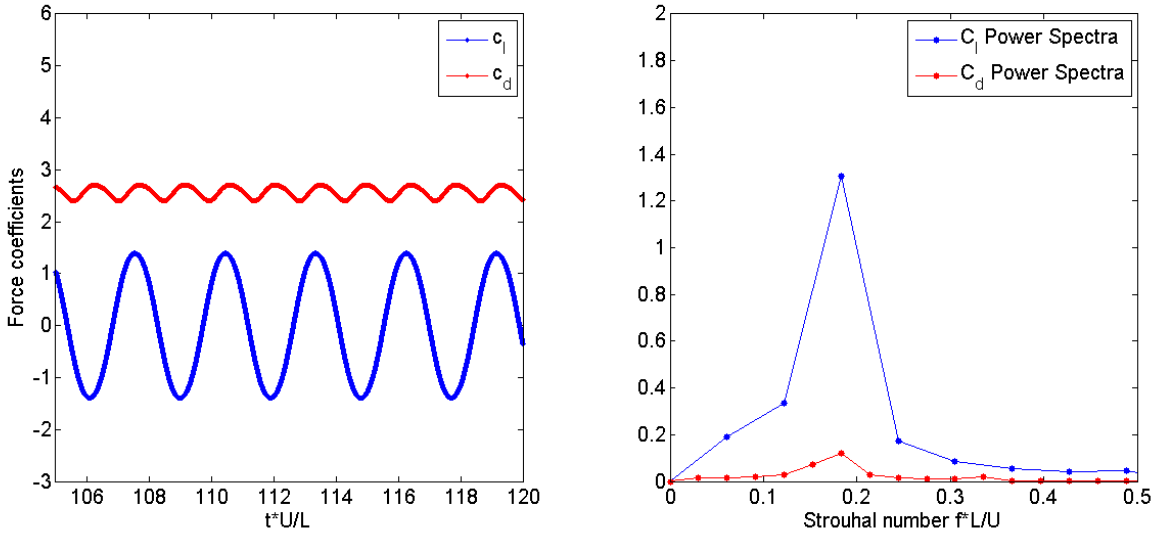

Figure 3.46 Time history and power spectra for aspect ratio 0.4

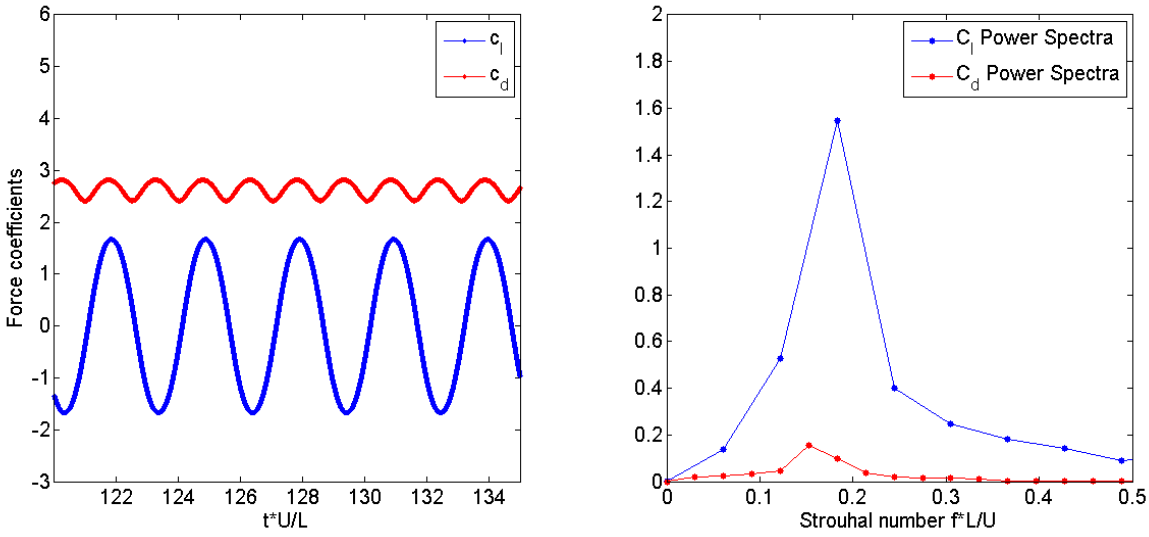

Figure 3.47 Time history and power spectra for aspect ratio 0.5

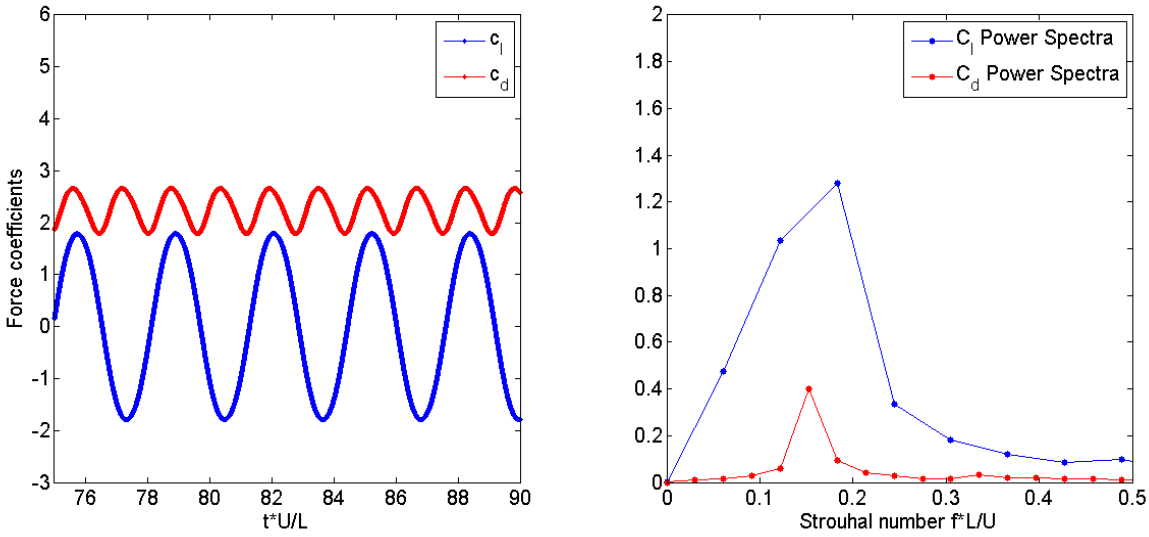

Figure 3.48 Time history and power spectra for aspect ratio 0.62

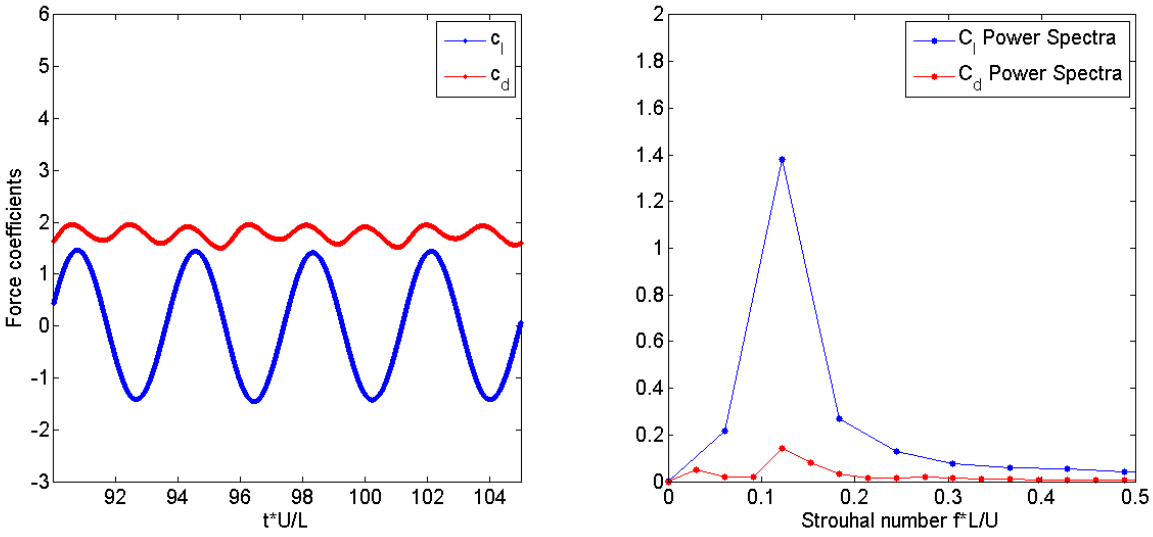

Figure 3.49 Time history and power spectra for aspect ratio 0.8

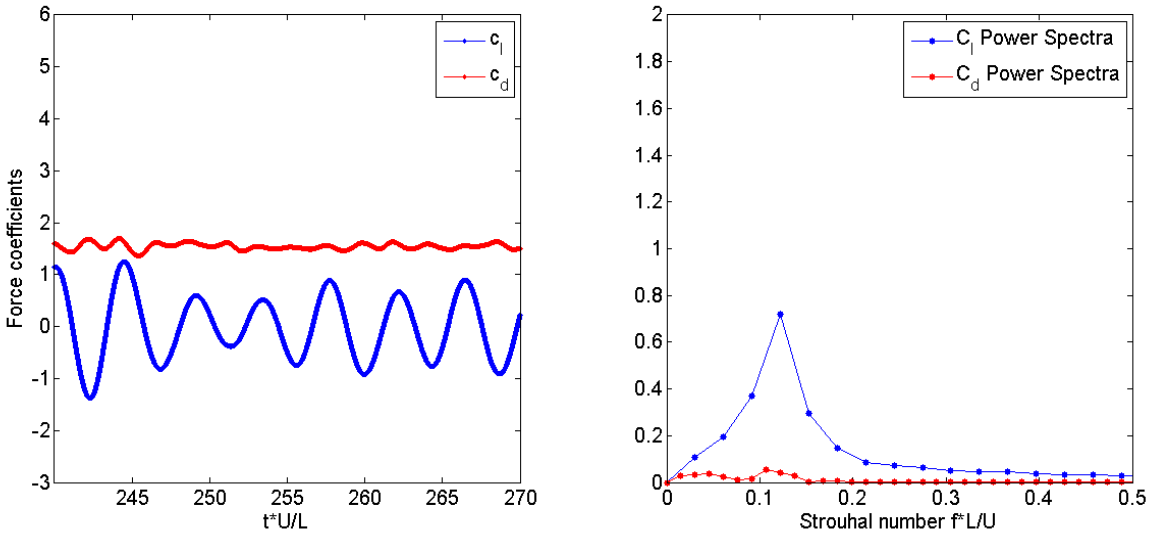

Figure 3.50 Time history and power spectra for aspect ratio 1.0

Table 3.3 Aspect ratio vs. Strouhal number for rectangular cylinders at Re = 500

Aspect Ratio	Strouhal Number
0.01	0.1210
0.2	0.1832
0.4	0.1832
0.5	0.1832
0.62	0.1855
0.8	0.1210
1.0	0.1210

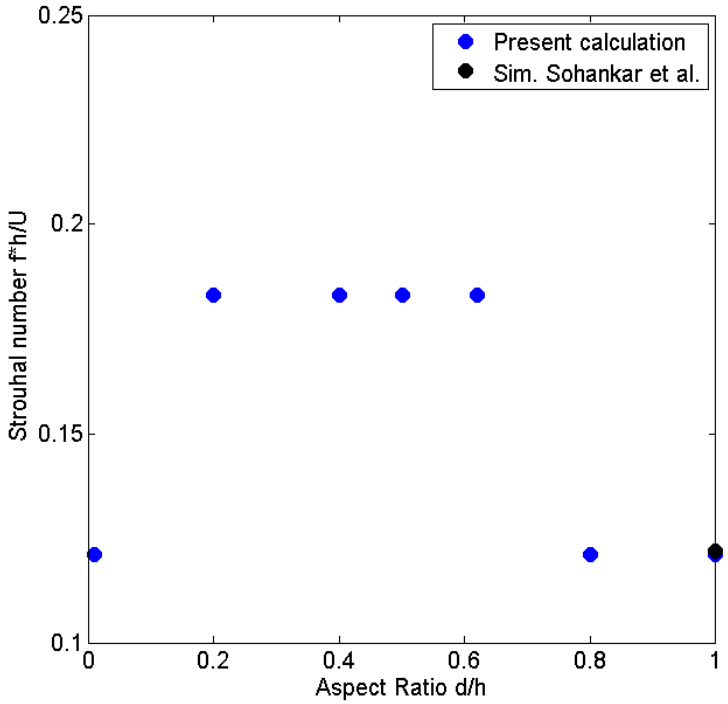

Figure 3.51 Strouhal number vs. aspect ratio for rectangular cylinders at Re = 500.Simulation result from Sohankar, Norberg, and Davidson [8].

3.5.3 *Fluctuating Lift and Drag Coefficients*

The fluctuating lift and drag coefficients were calculated using the following definitions:

$$C_L' = C_{L,RMS} \tag{3.2}$$

$$C_D' = \left(C_D - C_{D,mean}\right)_{RMS} \tag{3.3}$$

Physically, the quantities are representations of the oscillation amplitudes. The largest values of fluctuating lift were found to correspond to aspect ratios closest to the local increase in drag near aspect ratio 0.5 with aspect ratio 0.62 having the highest fluctuating lift coefficient. The fluctuating drag coefficient was found to be close to its smallest values near aspect ratio 0.5. The aspect ratio 1 case was not found to be in good agreement with the simulations by Sohankar, Norberg, and Davidson. An in-depth explanation of the square cylinder flow is reserved for Section 3.5.4.

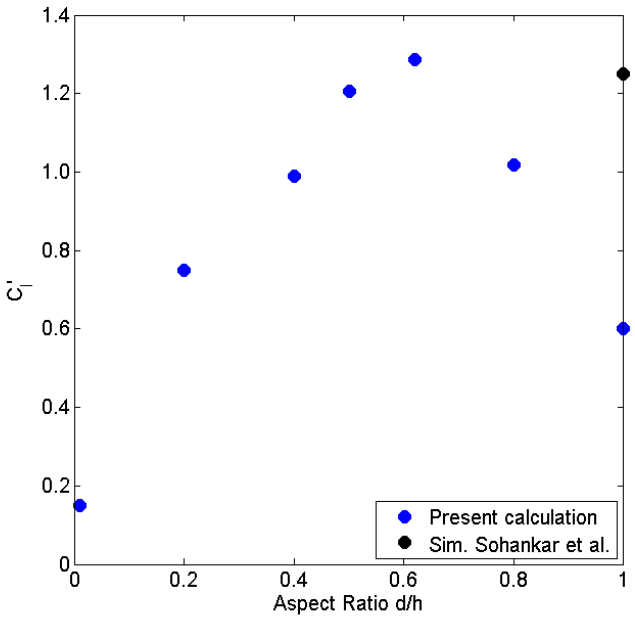

Figure 3.52 Fluctuating lift coefficient vs. aspect ratio for rectangular cylinders at Re = 500. Simulation result from Sohankar, Norberg, and Davidson [8].

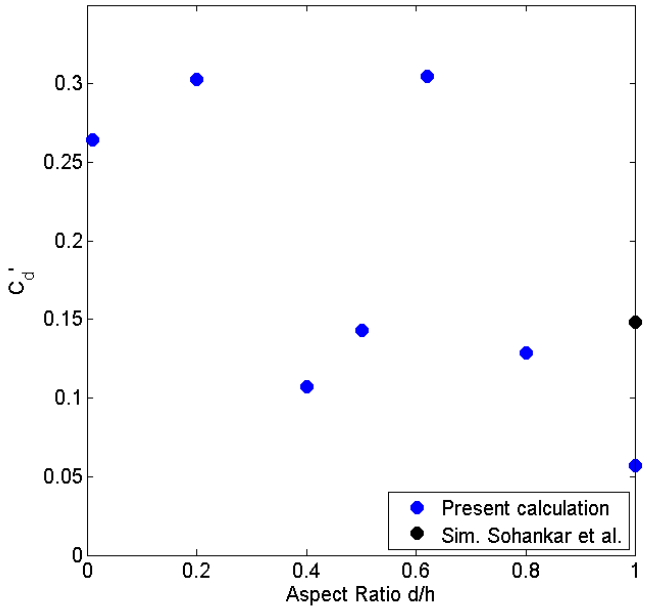

Figure 3.53 Fluctuating drag coefficient vs. aspect ratio for rectangular cylinders at Re = 500. Simulation result from Sohankar, Norberg, and Davidson [8].

3.5.4 *Square Cylinder at Re = 500*

In this section we consider the square cylinder, which is frequently used as a base test case. The Strouhal number of the present calculation was found to be in good agreement with the available experimental and simulation results. This can be seen in Fig. 3.54 and Table 3.4. As for the mean drag, fluctuating drag, and fluctuating lift, there were discrepancies between the present calculation and the simulation performed by Sohankar, Norberg, and Davidson.

Upon closer inspection, differences were found in the grid and the free stream boundary condition. The grid considered in this paper was $341 \times 53 \times 301$, while the grid by Sohankar, Norberg, and Davidson was $169 \times 121 \times 41$. During the initial trial simulations performed, the number of grid points in the spanwise direction was found to have mattered. In solving the turbulent simulations presented in the previous chapter, when too few grid points were used in the spanwise direction the simulation behaved like it was 2-D with a drag coefficient to match. In addition, there appears to be differences between the backend free-stream conditions of the two simulations. Fig. 3.55 shows the pressure coefficient and normalized velocity U/U_∞ on the centerline as a function of

downstream distance. In the present calculation, the pressure coefficient can be seen to recovering to a peak value then decreasing as it goes to the free-stream. This points the pressure gradient towards the free-stream. The simulations by Sohankar, Norberg, and Davidson show a pressure coefficient whose value is highest in the free-stream, which suggests there is a slight pressure gradient pointing in the direction towards the body. It has been shown that differences in the backend pressure can cause some variation in the drag coefficient.

In comparing the time history of the force coefficients, the simulations by Sohankar, Norberg, and Davidson did achieve a regular oscillatory pattern in the drag coefficient, while the present calculation did not. The time history of the simulation by Sohankar, Norberg, and Davidson is shown in Fig. 3.56, while the time history of the present calculation is shown in Fig. 3.37. This suggests that different wake patterns were observed in the two simulations, but it is unclear if this is a result of the different back end free-stream conditions, the differences in gridding, or some combination of both. The wake pattern in the present calculation showed two free shear layers that had a weak interaction and shed vortices far downstream of the body. The vortices were so far downstream that the amplitudes in the drag coefficient were quite small as can be seen in Fig. 3.50.

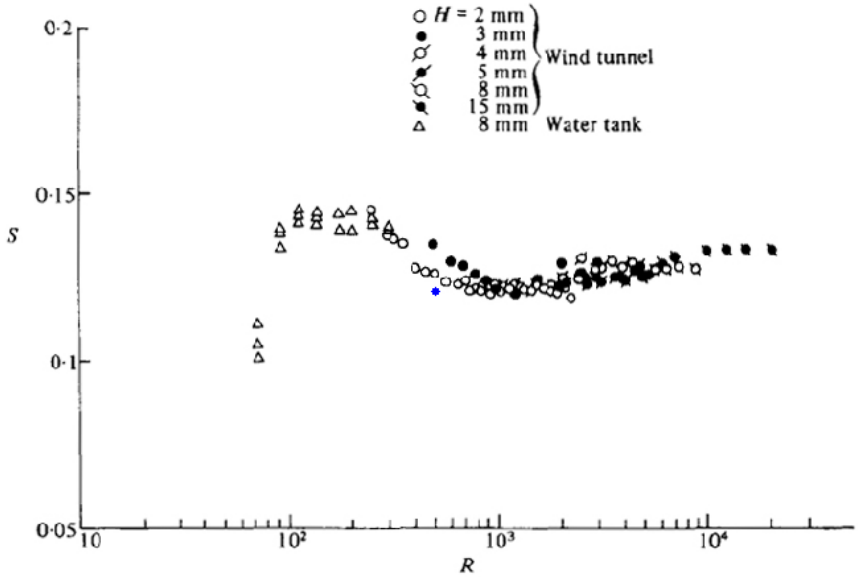

Figure 3.54 Strouhal number vs. Reynolds number for a square cylinder. Blue point is the present calculation. Image and experimental results originally from Okajima [4].

Table 3.4 Comparison of square cylinder simulation results with Sohankar, Norberg, and Davidson [8].

Simulation	C_d	St	C_d'	C_L'
Present Calculation	1.544	0.121	0.057	0.600
Sohankar, Norberg, and Davidson	1.87	0.122	0.148	1.25

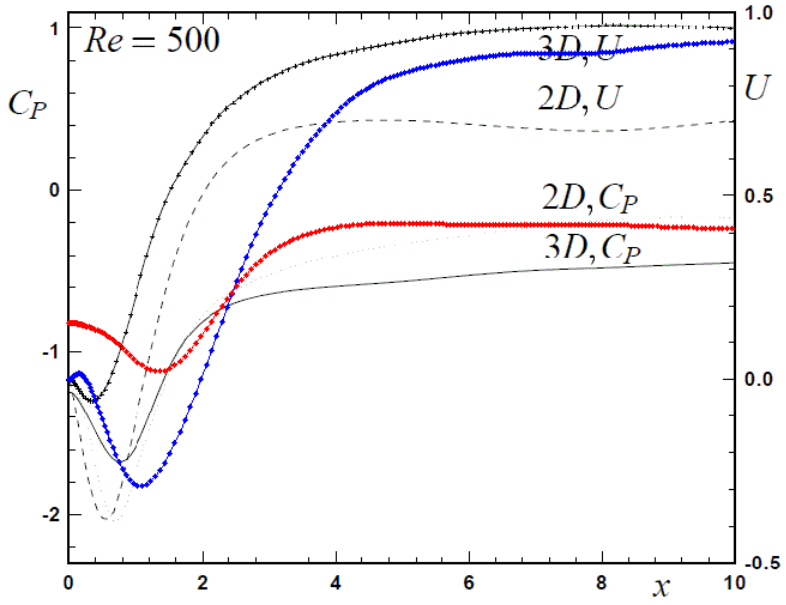

Figure 3.55 Pressure coefficient and normalized velocity vs. downstream distance on the centerline. The blue curve is U/U_∞ for the present calculation, while the red curve is C_P. Image is originally from Sohankar, Norberg, and Davidson [8].

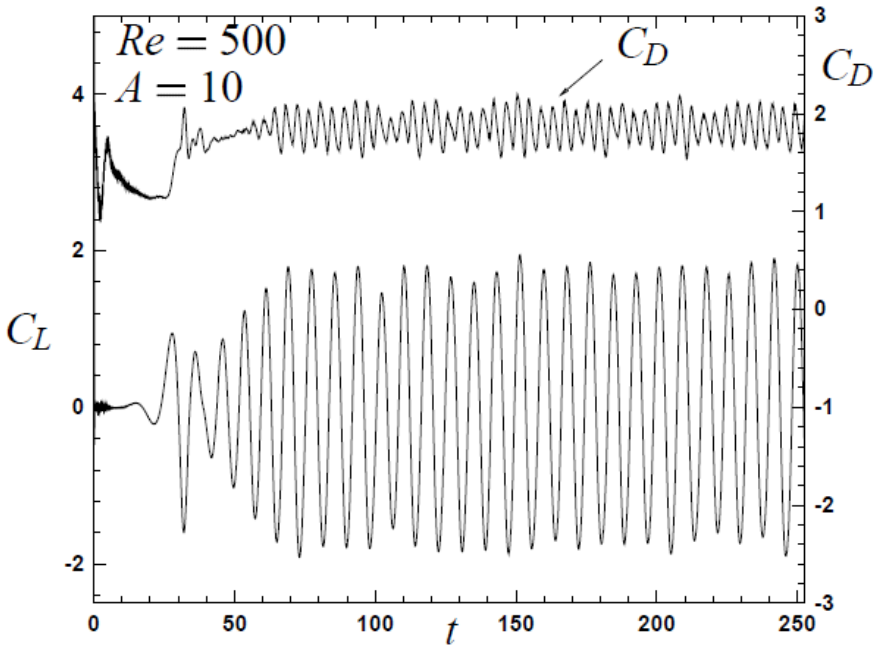

Figure 3.56 Time history of the force coefficients from the simulation of a square cylinder at Re = 500 by Sohankar, Norberg, and Davidson. Image originally from Sohankar, Norberg, and Davidson [8].

3.5.5 *Discussion of the flow physics*

When discussing the drag of rectangular cylinders, it can be said that the physics are much simpler when compared to a circular cylinder. This can be attributed to the fixed separation points of a rectangular cylinder at the leading edge corners versus the moving separation points of a circular cylinder that are a function of Reynolds number. As a result, the reasons for the changes in the drag coefficient of rectangular cylinders are easier to determine. For the Reynolds numbers considered (500 and 20,000), the pressure distribution on the front face is approximately the same for all aspect ratios and is independent of Reynolds number. The skin friction on the top and bottom surfaces is negligible and make no appreciable contribution to the drag of the object. Thus, it can be concluded that any change in the drag coefficient is determined by what happens after separation at the leading edge corner.

Separation of the front face boundary layers at the leading edge corners leads to the formation of two free shear layers, which interact and develop an instability. At the Reynolds numbers considered, the instability leads to the formation of shed vortices in the wake, which is known as

the von Karman vortex street. The free shear layer is known to have three different interactions with the rectangular cylinder and there is a difference between the low Reynolds number case and the high Reynolds number case. A cartoon depiction to distinguish the two is shown in Fig. 3.57. At high Reynolds number, it has been observed that the three interactions are the free shear layer stays unattached, the free shear layer intermittently reattaches, and the free shear layer reattaches and separation occurs again at the trailing edge corners. While these interactions are most certainly the same at lower Reynolds numbers, the aspect ratios where they occur are very different.

In the high Reynolds number case, the shed vortex was observed to be closest when the drag was the highest. This appeared to coincide with intermittent reattachment of the free shear layer, which happened at an aspect ratio of 0.6. For the other aspect ratios, the vortex was never as close and the resulting drag coefficients were much lower. In the low Reynolds number case, max drag occurred at an aspect ratio of 0.2. The shed vortex was also observed to be closest at this aspect ratio, which is quite different than the high Reynolds number case. At that aspect ratio, the free shear layer is still unattached. This suggests that there is a change in the curvature of the free shear layer between the low Reynolds number case and the high Reynolds number case. It has been observed that when the curvature of the free shear layer increases, only then is the shed vortex able to form close to the rear face.

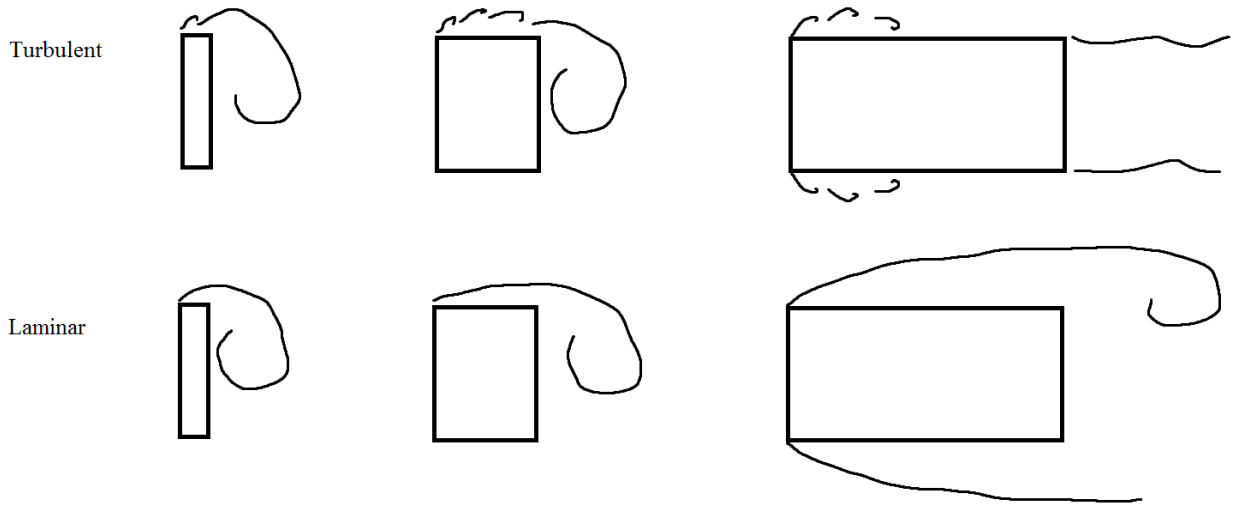

Figure 3.57 Cartoon depiction of the flow with a turbulent free shear layer vs. a laminar free shear layer.

To explore this further, we compare the flow visualization images of Bearman and Trueman (not shown due to copyright) to the images of the y-vorticity at max drag during an oscillation cycle as shown in Figs. 3.60 – 3.65. From the two sets of images, it is possible to make an estimate of the distance to formation of the shed vortex for a given aspect ratio. The definition of the length scales considered is shown in Fig. 3.58. The length R is the distance to formation of the shed vortex from the rear face and parallel to the x-axis. Ten samples were taken for each image and the average normalized distance to shed vortex formation R/h was determined. The results are shown in Fig. 3.59. For the images presented by Bearman and Trueman, we see the expected result of the aspect ratio 0.6 case having the smallest distance to shed vortex formation. This is consistent with the observation that this occurs when the drag is highest. For the low Reynolds number case, we see a similar result. The aspect ratio 0.2 case, which also had high drag, had the smallest distance to shed vortex formation. In comparing the two cases, the low Reynolds number case consistently had a smaller distance to shed vortex formation than the images representing the high Reynolds number case by Bearman and Trueman. This suggests that the curvature is certainly different between the higher Reynolds number case and the lower Reynolds number case. However, it should be considered that the images by Bearman and Trueman were from a water tunnel at an unknown Reynolds number and its time during the shedding cycle is unknown. The original experiments and the simulations presented in this paper were performed with air as the primary fluid and the Reynolds numbers were well documented.

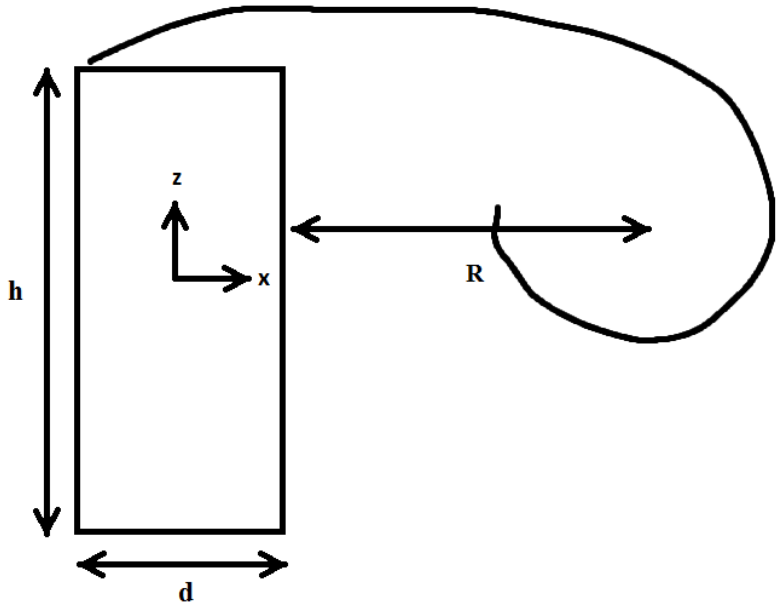

Figure 3.58 Cartoon of the rectangular cylinder and distance estimate to shed vortex center.

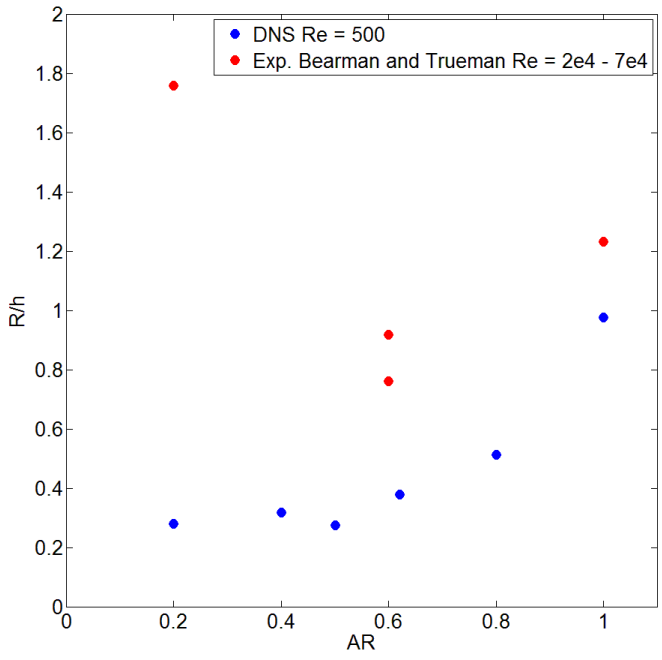

Figure 3.59 Distance to shed vortex center vs. aspect ratio.

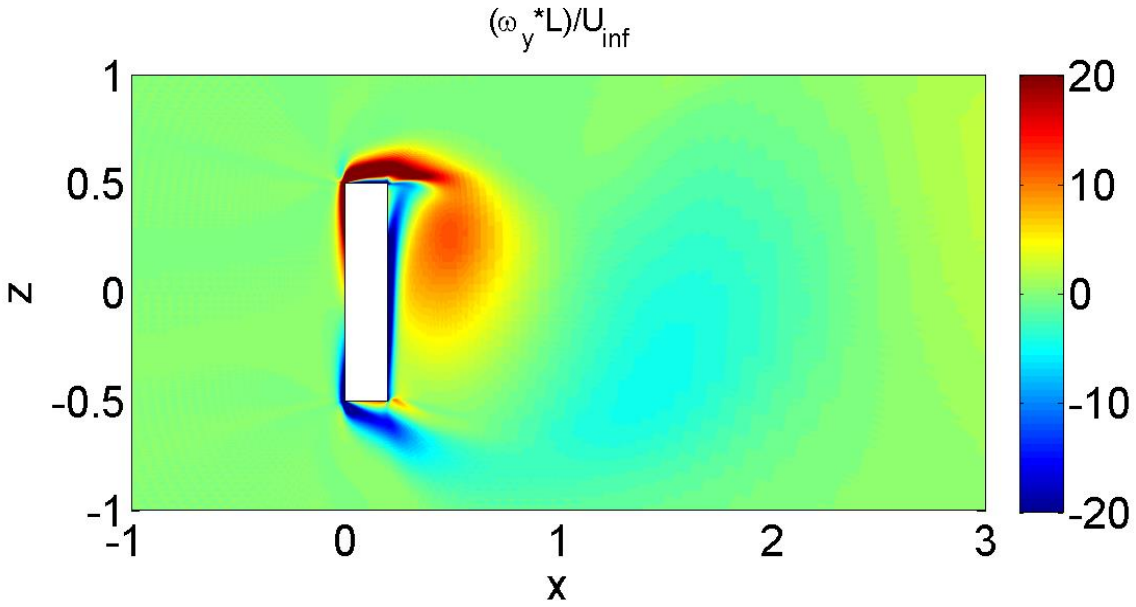

Figure 3.60 Normalized y-vorticity for the aspect ratio 0.2 case.Image is of the x-z plane at mid-span.

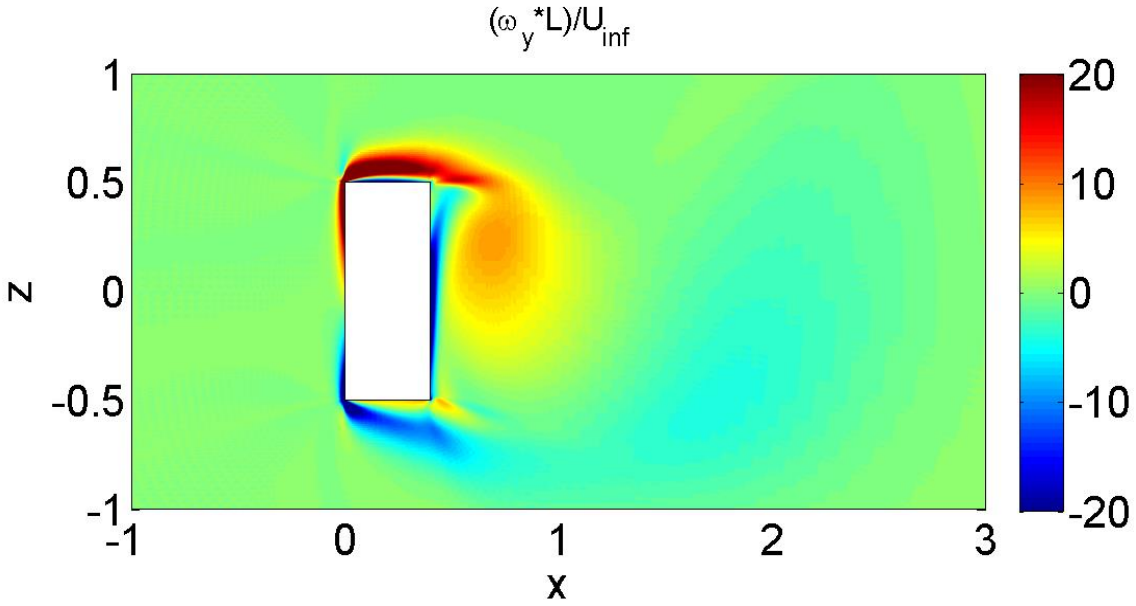

Figure 3.61 Normalized y-vorticity for the aspect ratio 0.4 case.Image is of the x-z plane at mid-span.

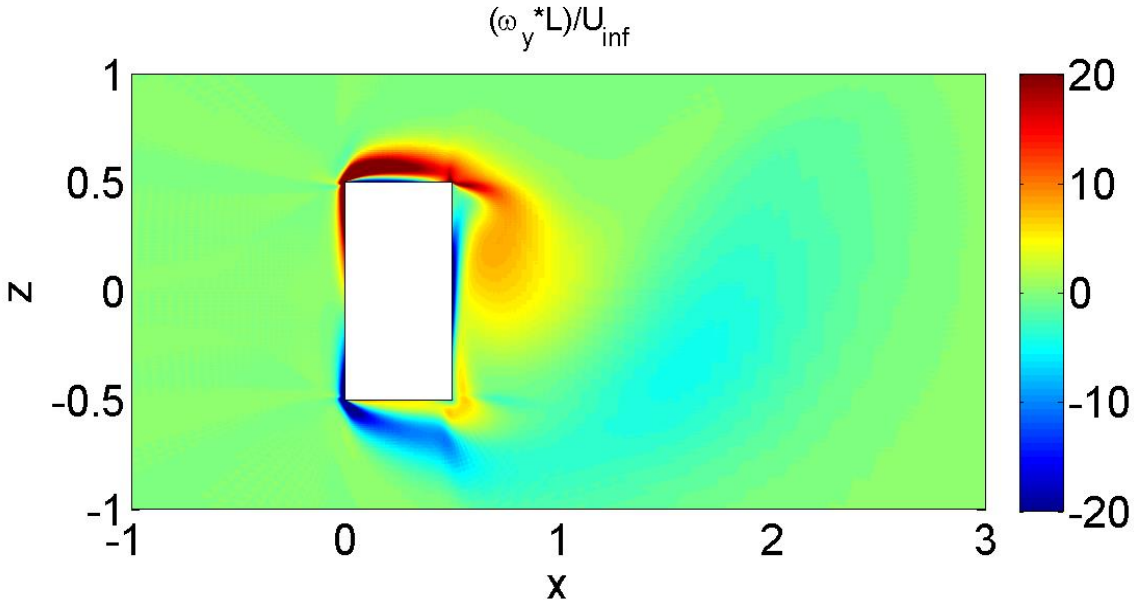

Figure 3.62 Normalized y-vorticity for the aspect ratio 0.5 case.Image is of the x-z plane at mid-span.

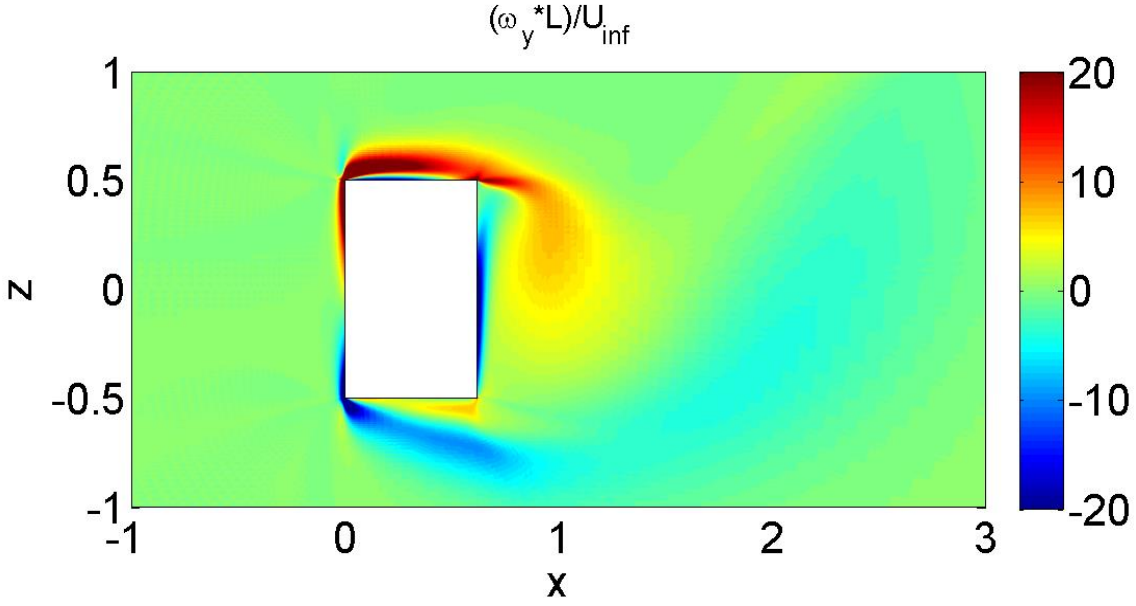

Figure 3.63 Normalized y-vorticity for the aspect ratio 0.62 case.Image is of the x-z plane at mid-span.

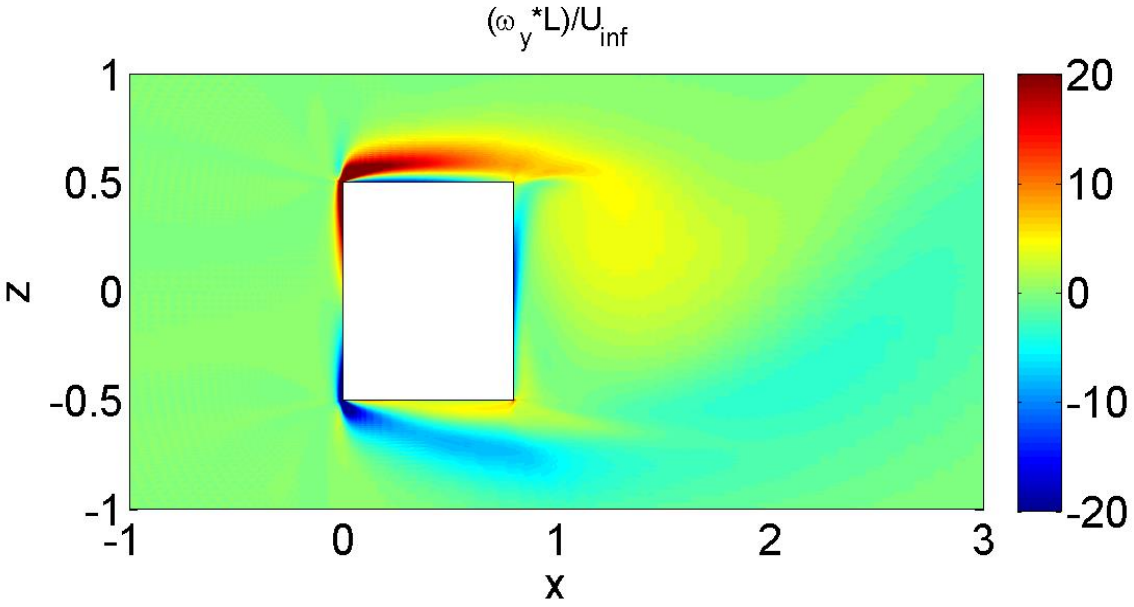

Figure 3.64 Normalized y-vorticity for the aspect ratio 0.8 case.Image is of the x-z plane at mid-span.

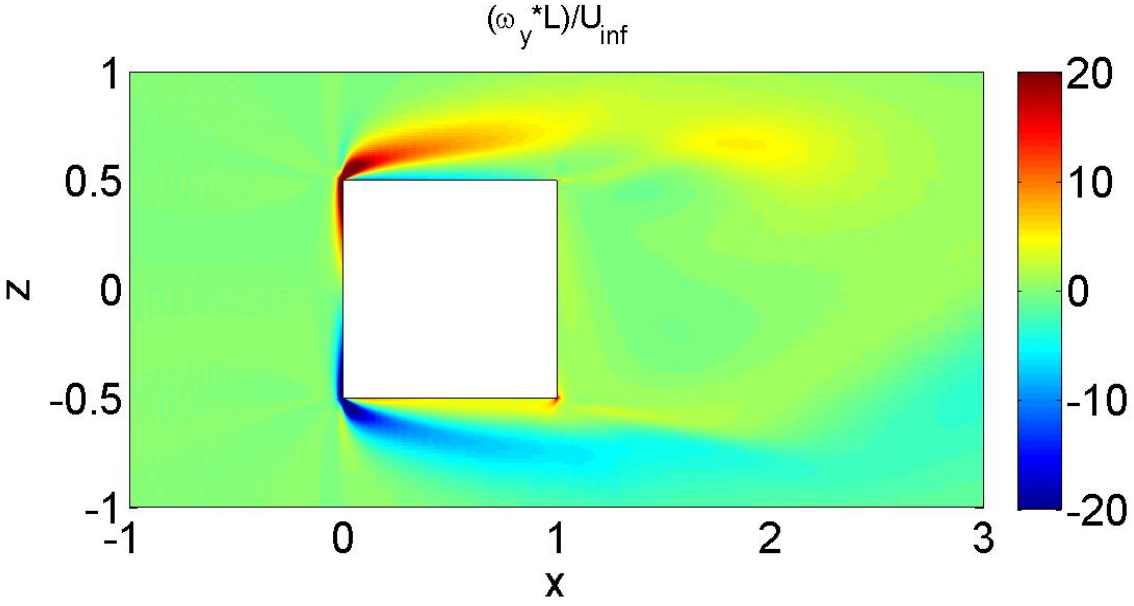

Figure 3.65 Normalized y-vorticity for the aspect ratio 1.0 case.Image is of the x-z plane at mid-span.

While the result in Fig. 3.59 is not definitive, it does suggest that the free shear layer curvature is most likely quite different between the high and low Reynolds number cases and is due to an effect that occurs at one Reynolds number, but not the other. The only other known effect that could cause this was determined to be vortex roll-up in the free shear layer, which is known to occur at higher Reynolds numbers. Unfortunately, the flow visualization images of Bearman and Trueman do not show the roll-up of vortices in the free shear layer, which is because the images were taken in a water tunnel, thus making their free shear layers appear to be laminar. This most certainly would not be the case at higher Reynolds number in a wind tunnel. Fortunately, vortex roll-up in air has been shown by Koenig and Roshko in their experiments on bluff bodies in tandem at a similar Reynolds number to the original experiment [25]. It is believed that vortex roll-up accounts for the difference seen in the flow patterns at the high and low Reynolds numbers considered.

The qualitative explanation of the flow physics will be broken down into two parts. First, the reason the free shear layer curves tightly around the body, and second, the effect vortex roll-up has on the free shear layer. We'll begin with the free shear layer curving around the body.

If we simplify the problem to potential flow and the free shear layer to a vortex sheet, it can be shown that the vortex sheet will want to wrap around the body and almost certainly as tight as possible. Consider a vortex in the presence of a wall in potential flow. To satisfy the boundary conditions, the well-known result is an image vortex of opposite sign and equal strength is placed on the other side of the wall and the induced velocity of the vortices on one another propel each other through the fluid. However, it has been shown by Saffman that the boundary conditions can be satisfied by any number of vorticity distributions, so long as there is no flow normal to the wall at the wall [26]. A possible distribution that satisfies the boundary conditions is shown in Fig. 3.66. If the same distribution is applied to half a rectangular cylinder extending to infinity in the presence of a vortex sheet, we see that the velocity induced by the boundary conditions will guide the vortex sheet around the corner as shown in Fig. 3.67.

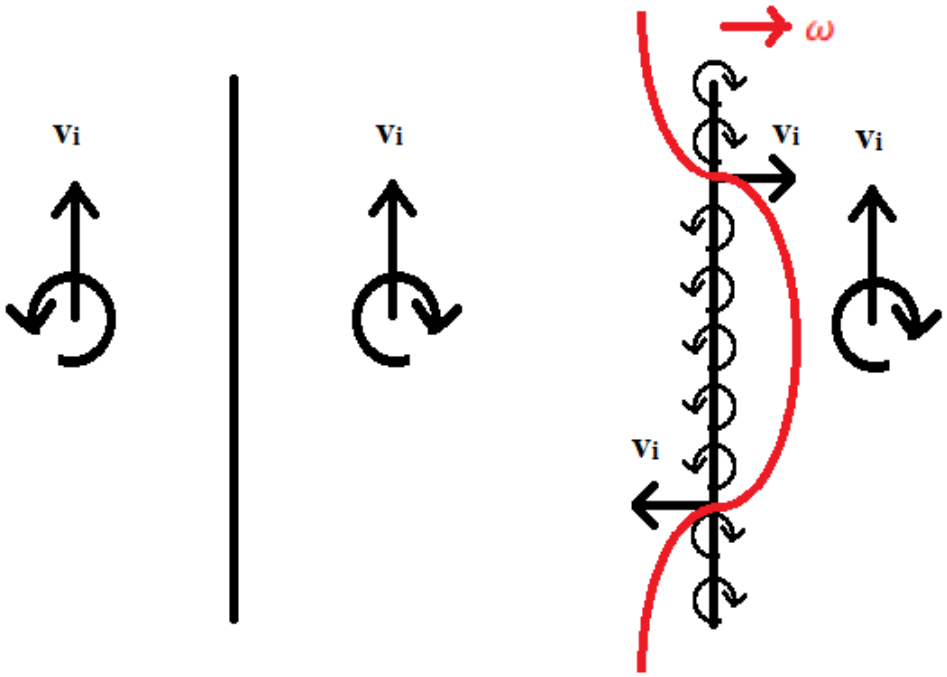

Figure 3.66 Illustration of possible boundary conditions to satisfy a vortex next to an infinite wall in potential flow.The classic solution of a vortex and its image are shown on the left, while another possible distribution of vorticity is shown on the right.

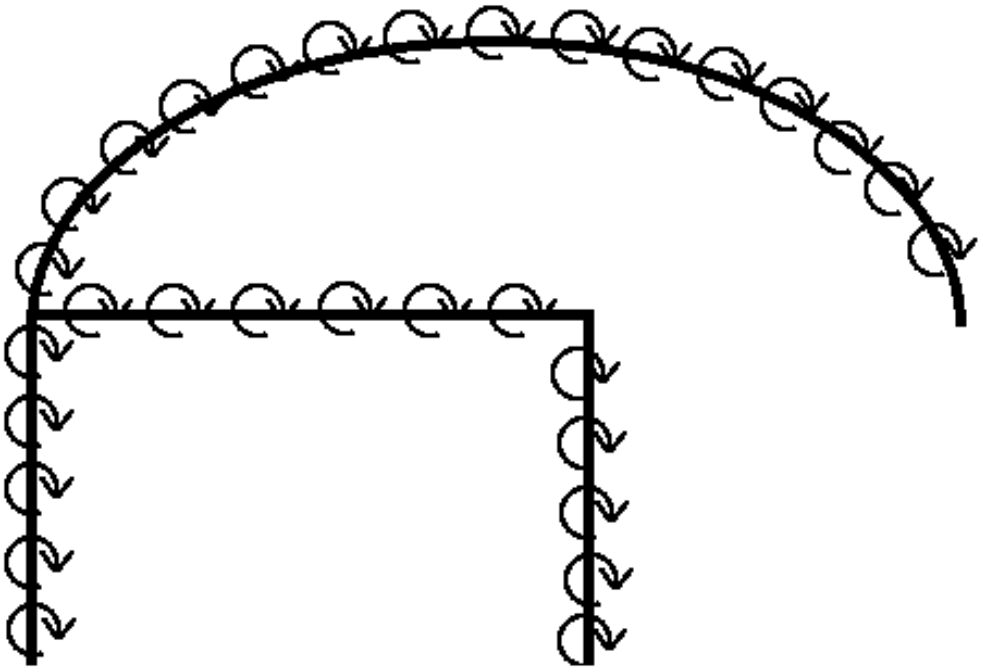

Figure 3.67 Illustration of a vortex sheet going around a corner due to the boundary conditions.

As has been demonstrated, it is believed that the boundary conditions will make the free shear layer wrap around the body as tightly as possible if left unhindered. At higher Reynolds number, it has been observed that for relatively short bodies, where the free shear layer remains unattached, that the curvature of the free shear layer is reduced making the shed vortex form farther away from the rear face than it would at lower Reynolds numbers. This was attributed to the effect of vortex roll-up within the free shear layer.

Vortex roll-up within the free shear layer entrains fluid from above and below the free shear layer. Above the free shear layer, the available volume of fluid is from the free stream, which can supply an endless amount. However, on the low speed side of the free shear layer, there is a finite volume of available fluid on the top and bottom surface of the rectangular cylinder. Depending on the aspect ratio, more fluid can be supplied to the volume from the back side. The introduction of additional fluid into this volume is determined by the free shear layer. As it was shown earlier, the boundary conditions of the flow make the free shear layer curve around the body, and as the aspect ratio increases, the free shear layer can intermittently or permanently reattach to the rectangular cylinder. This would cut off the supply of additional fluid into the volume underneath the free shear layer. From what has been determined, this volume of fluid can drastically change the trajectory of the free shear layer. For small aspect ratios, where the free shear layer remains unattached, the supply of fluid into the volume is not limited and the resulting reverse flow to satisfy entrainment of vortex roll-up in the free shear layer must be small. Pressure above the free shear layer becomes lower than it normally would be in the absence of vortex roll-up and lifts the free shear layer away from the body and reduces its curvature. This results in the increase in distance to shed vortex formation and the decrease in the drag coefficient that we see at higher Reynolds number for the small aspect ratios. As the aspect ratio increases, the area dividing the volume of fluid on the top and bottom surfaces and the supply of fluid from the rear side decreases due to the free shear layer. Since the entrainment rate of the vortices does not change, the reverse flow must increase to satisfy the entrainment rate. This decreases pressure on the underside of the free shear layer such that the free shear layer is pulled back towards the body, thus increasing the curvature of the free shear layer.

The explanation of the free shear layer for larger aspect ratios is consistent with the following explanation. The distance to initial roll-up of a vortex $S_{roll-up}$ in the free shear layer is proportional to the momentum thickness of the laminar boundary layer θ_o on the front face as shown in Eqn. 3.4. The momentum thickness is also proportional to $\sqrt{\nu t}$, which is proportional to the thickness of the laminar boundary layer that occurs on the front face. From the parameters of the problem, we can form the time scale $t = h/U_\infty$ and inserting this timescale, we get the relationship shown in Eqn. 3.5. Using the definition of Reynolds number with length scale h in Eqn. 1.2, we arrive at the expressions seen in Eqns. 3.6 and 3.7. These expressions show that as the Reynolds number increases, the distance to roll-up decreases. The decrease in distance to roll-up increases the distance over which entrainment can occur because entrainment begins sooner. To satisfy the increase in entrainment, reverse flow on the surface must increase, but this slows down the convective speed of the rolled-up vortices within the free shear layer. This results in vortices becoming larger much sooner and the spreading angle of the free shear layer being increased.

$$S_{roll-up} = const. \times \theta_o \tag{3.4}$$

$$\theta_o = const. \times \sqrt{\nu \frac{h}{U_\infty}} \tag{3.5}$$

$$\frac{\theta_o}{h} = \text{const.} \times Re^{-1/2} \tag{3.6}$$

or

$$\frac{S_{roll-up}}{h} = \text{const.} \times Re^{-1/2} \tag{3.7}$$

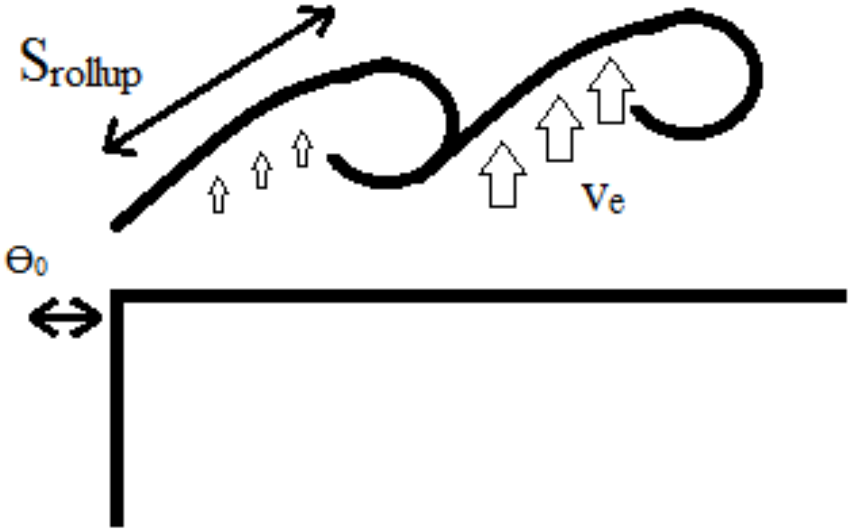

Figure 3.68 Cartoon relating the momentum thickness to distance of initial vortex roll-up

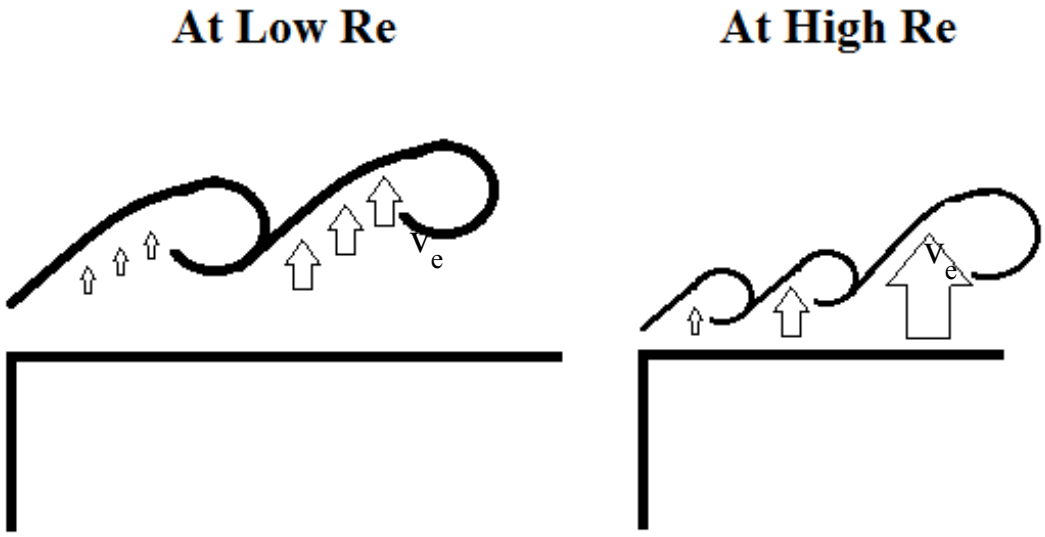

Figure 3.69 Cartoon showing the relationship between Reynolds number and vortex entrainment velocity. At higher Reynolds number, the entrainment velocity of the vortices is higher, which results in thinner boundary layers.

The qualitative explanation of the flow around the rectangular cylinder is believed to be consistent with itself and the results presented. In the low Reynolds number case and the absence of vortex roll-up in the free shear layer, the free shear layer tries to curl around the body as tightly as possible as soon as possible. This results in a free shear layer with high curvature forming a shed vortex as close to the rear face as possible. As the aspect ratio is increased further, free shear layer impingement was observed at aspect ratio 0.5 and the free shear layer becomes parallel to the top and bottom surfaces for the aspect ratios 0.8 and 1.0. In the high Reynolds number case and the presence of vortex roll-up in the free shear layer, the free shear layer is initially lifted away from the body more so than the low Reynolds number case. As the aspect ratio is increased further, reverse flow increases and the free shear layer curvature is increased. The combination of the initial deflection of the free shear layer and the increased curvature as the aspect ratio increases delays free shear layer impingement to aspect ratio 0.6 at higher Reynolds numbers. For aspect ratios greater than 0.6, eventually reattachment occurs and separation occurs again at the trailing edge corner. The aspect ratio where reattachment occurs at higher Reynolds number is most certainly less than the lower Reynolds number case.

3.5.6 *Comment on Spanwise Flow and Three-Dimensionality*

In searching for the cause of the drag increase, the mean spanwise flow was observed. A localized increase in drag has been observed to occur between aspect ratios 0.4 and 0.5. As can be seen in Fig. 3.70, the last aspect ratio exhibiting a mean spanwise flow was aspect ratio 0.5. As this was considered further, it was remembered that in the higher Reynolds number regime that some aspect ratios were successfully simulated as 2-D, while others were not. The aspect ratios not exhibiting a mean spanwise flow are 2-D flows on average and most likely the reason why it is acceptable to simulate them as 2-D.

As this was considered further, the drag coefficient of rectangular cylinders was plotted as a function of its Reynolds number and aspect ratio as can be seen in Fig. 3.71. The 3-D surface was formed using the data from Bearman and Trueman and the simulation results of the present calculations. In addition, the transition point from 2-D to 3-D flow for circular cylinders was considered as an approximation for the normal flat plate. This occurs around a Reynolds number

of 200. Projecting this surface onto the Reynolds number-aspect ratio plane and highlighting the last aspect ratio at each Reynolds number where mean spanwise flow is thought to exist, a curve can be formed showing the relationship between the Reynolds number, aspect ratio, and the existence of a mean spanwise flow. This is shown in Fig. 3.72. This figure potentially provides guidance for future simulations as to where it may be acceptable to make the 2-D assumption even at higher Reynolds number. This awaits confirmation through future research.

Furthermore, there is no reason to believe that the direction of the spanwise flow is unique. Two simulations on the aspect ratio 0.5 case were run with different initial conditions. The first initial condition was a mound of positive vorticity with positive spanwise velocity was allowed to flow over the body. The second initial condition was a mound of negative vorticity with negative spanwise velocity. The mean spanwise flow for each case is shown in Fig. 3.73.

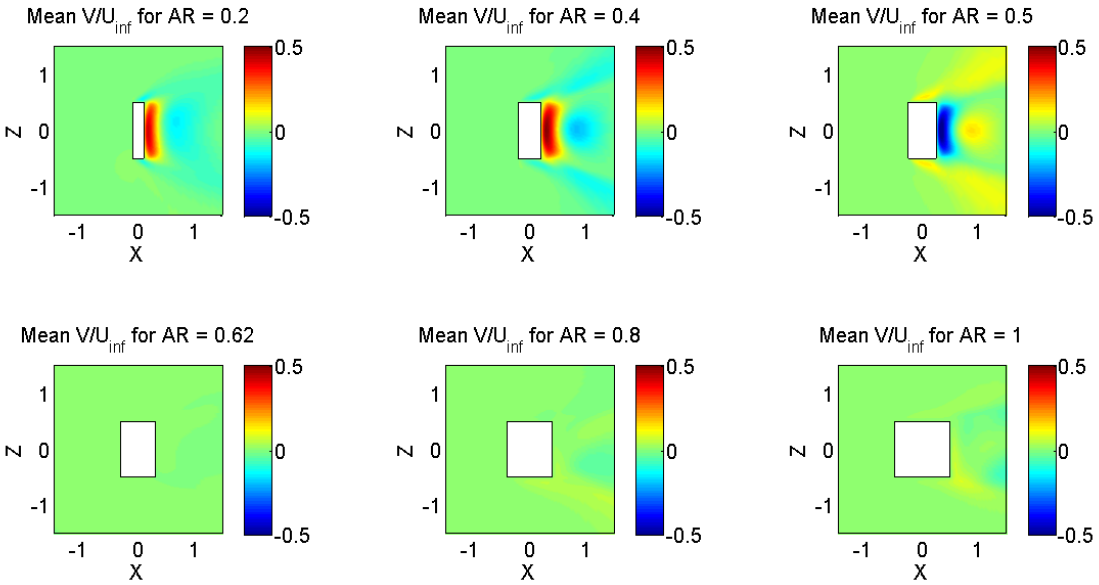

Figure 3.70 Mean spanwise flow of various aspect ratios at Re = 500.

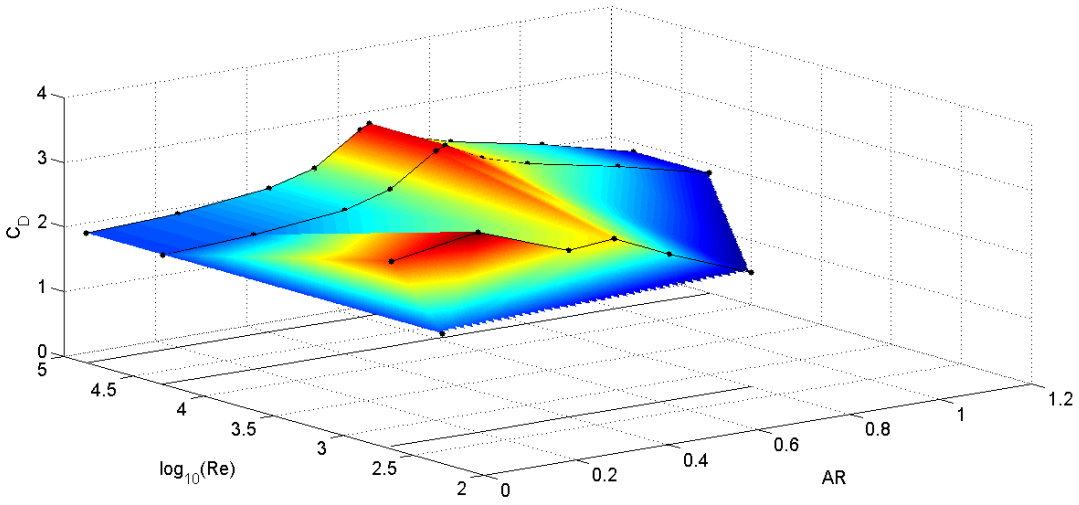

Figure 3.71 Drag coefficient as a function of Reynolds number and aspect ratio.Drag coefficient data at Re = 2×10^4 - 7×10^4 from Bearman and Trueman [2]. Present calculation provides drag coefficient results at Re = 500.

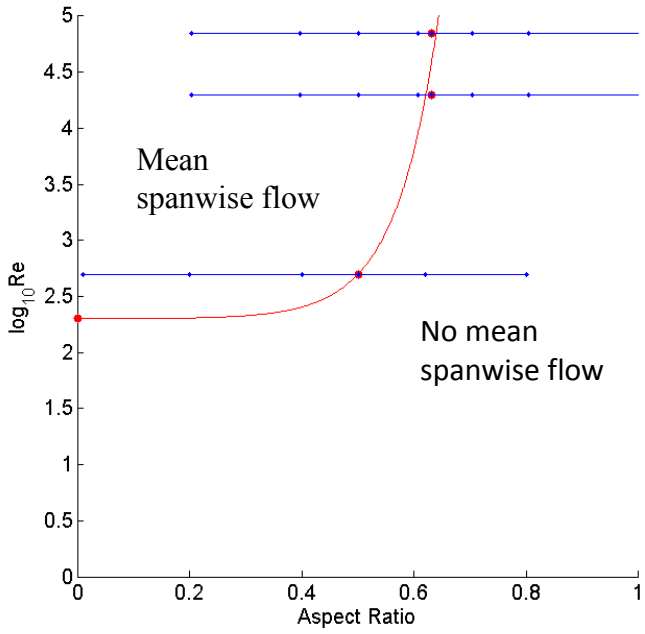

Figure 3.72 Projection of the drag coefficient onto the Re vs. AR plane. Points highlighted in red correspond to where transitions in mean spanwise flow to no mean spanwise flow are thought to occur, which correspond to the increases in drag.

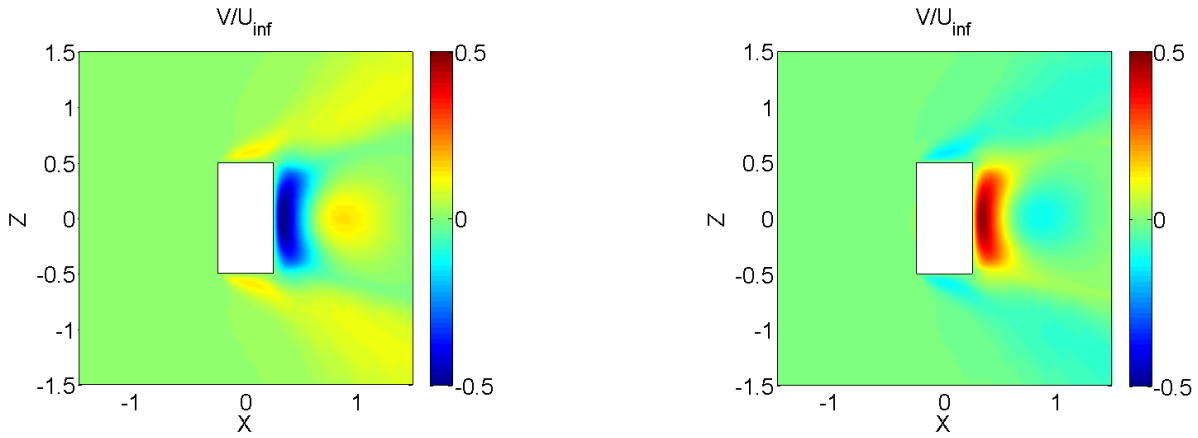

Figure 3.73 Mean spanwise velocity for an aspect ratio 0.5 rectangular cylinder. Two different initial conditions produced two values of the mean spanwise velocity.

3.6 CONCLUSIONS

In this chapter, rectangular cylinders at Re = 500 were explored numerically using DNS. The drag coefficient was found to have a significantly different trend when compared to the original experiment. The critical aspect ratio was reduced and the peak drag coefficient increased. At Re = 20,000, the critical aspect ratio was 0.62 with a peak drag of 2.94. For the present calculation at Re = 500, the critical aspect ratio was 0.2 with a peak drag of 3.09. In addition, there was found to be very little variation in the Strouhal number with each aspect ratio being one of two values.

Moreover, a mean spanwise flow was found to exist for aspect ratios less than or equal to 0.5. This also coincided with the first aspect ratio exhibiting a free shear layer that impinges on the trailing edge corner. The combination of these two events is believed to cause the local increase in the drag coefficient that is shown for the aspect ratio 0.5 case.

When compared to the original experiment at high Reynolds number, the lack of vortex entrainment in the free shear layer is believed to be the cause of the drastically different flow behavior between the low Reynolds number case and the high Reynolds number case. At Re = 500, the separating vortex sheet does not roll up into shear-layer vortices near the body. The displacement thickness of this laminar layer remains thin. In contrast, at high Reynolds number,

the shear layer vortices are formed very near the separation point, so that this turbulent layer spreads at a relatively rapid rate with a large displacement thickness. The outer, high-speed streamlines are deflected by the displacement thickness of the layer, so that the trajectory of the layer is less curved than for the low Reynolds number flow. As a consequence, the critical aspect ratio of maximum drag is much larger at high Reynolds number.

The maximum drag coefficient is somewhat lower for turbulent case, since the thick shear layer rolls up into relatively large von Karman vortices near the base of the body. The laminar shear layer at lower Reynolds number forms smaller and tighter vortices with lower pressure near the base, increasing the drag.

Chapter 4. MODIFIED RECTANGULAR CYLINDERS AT RE = 500

4.1 MOTIVATION

Based upon the mechanic of drag increase as explained for rectangular cylinders at higher Reynolds numbers, a method to increase the drag coefficient of the aspect ratio 0.62 cylinder at Re = 500 is explored. This particular aspect ratio was selected because there is a known starting point at Re = 500 that has significantly lower drag than it does at Re = 20,000. While this ideal is not novel, the method to which it will be achieved is. It can be said that what is being proposed is analogous to the way the dimples on a golf ball raise the effective Reynolds number on a smooth sphere into the drag crisis regime.

The method selected to increase the drag of the selected aspect ratio is based on the relationship between the momentum thickness and Reynolds number as seen in Eqn. 3.6. Since momentum thickness and Reynolds number are inversely proportional, it can be said that if we decrease the momentum thickness, the Reynolds number will effectively increase. This will be accomplished by removing fluid from the boundary layer on the front face, which makes the momentum thickness decrease. This will decrease the distance to initial vortex roll-up within the free shear layer and effectively increase the Reynolds number. In addition, we will consider a location to vent the fluid for potential future application use.

4.2 GRIDS

To modify the geometry of the rectangular cylinder for suction, a shift from the single grid format to the multigrid format was made. This required making multiple individual grids and assembling them using the Chimera overset grid approach, from which Overflow gets its name. Three configurations were considered. The first was front suction only, while the second was blowing out of the top and bot only. The third configuration or full configuration was the combination of suction on the front faces and blowing out of the top and bottom. The holes for suction and blowing were set to be $0.02h$ width. The length of the hole was set to be $0.1h$. The holes for front suction were centered about a point $0.15h$ from each leading edge corner. The holes for top and bot blowing were centered at a point $0.05h$ from the trailing edge corners. All holes were set to span

the entire bluff body from η_{min} to η_{max}. A 2-D close up of an individual hole is shown in Fig. 4.1. Finer grids around the corners and directly in front of the hole were added. The normal off the wall spacing of each of those grids was to 1.0×10^{-4}. 2-D sections of all 3 configurations are shown in Figs. 4.2-4.4. A completed 3-D grid is shown in Fig. 4.5.

The top and bottom of the hole had viscous walls applied. At η_{min} and η_{max}, an inviscid wall was applied like the base grid. At the end of the hole, the pressure and velocity were specified. For an incompressible flow, only one of the conditions is necessary, but since the code is compressible both needed to be specified. The conditions of the front suction case were specified as $U/a_\infty = 0.02$ and $P/P_\infty = 0.996$. The conditions of the top/bot blowing case were specified as $U/a_\infty = 0.01$ and $P/P_\infty = 1.001$. The values of pressure were chosen such that the holes would suck or blow without an adverse pressure gradient developing within the hole. Through some trials, it was determined that if the pressure was not set low enough for suction or high enough for blowing, that pressure gradients going opposite their intended direction would develop within the hole.

The boundary conditions of the remaining grids were specified according to the parts of the rectangular cylinder or hole they contacted. Viscous walls were applied for parts of the grid in contact with the rectangular cylinder or the hole walls and as always, inviscid walls at η_{min} and η_{max}.

In terms of the non-dimensional mass flux defined in Eqn. 4.1, the mass flux through the front suction holes and top/bot blowing holes were 2 and 1, respectively. In addition, this was also verified through the integration program. The reference area was set to be $A_{ref} = 0.04h^2$, which was equal to the hole height multiplied by the span. The reference area was also equal to the area the mass flowed through making the ratio $A/A_{ref} = 1$. Since the simulations were in the incompressible regime, this resulted in the non-dimensional mass flux being equal to the ratio of velocity specified at the end of the hole normalized by the free stream velocity.

$$\dot{m} = \frac{\rho U A}{\rho_\infty U_\infty A_{ref}} \tag{4.1}$$

where A is the calculated area the mass goes through and A_{ref} is a set reference area.

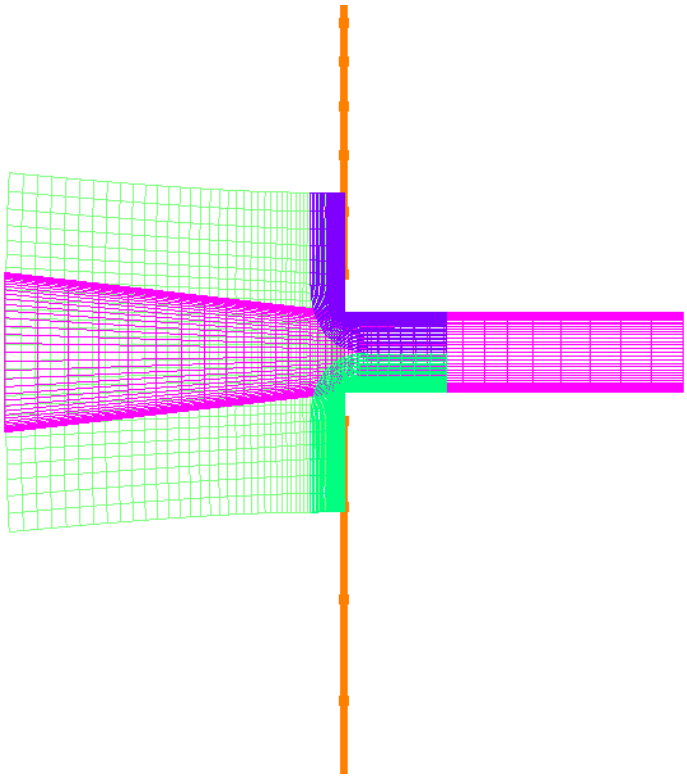

Figure 4.1 Close up of the multiple grids that form the hole for suction. Image of the x-z plane at mid-span (y = 0).

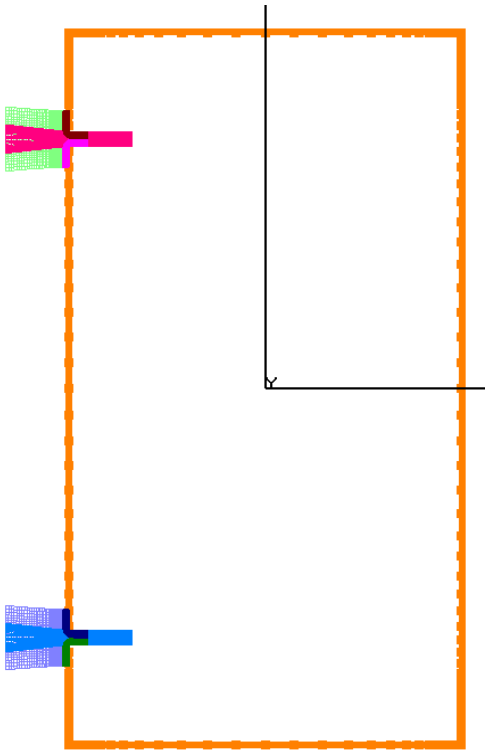

Figure 4.2 Grid of the front suction case. Image of the x-z plane at mid-span (y = 0).

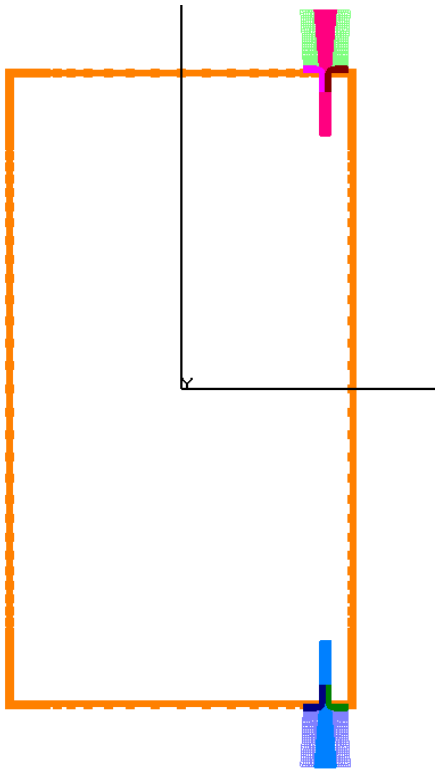

Figure 4.3 Grid of the top/bot blowing case. Image of the x-z plane at mid-span (y = 0).

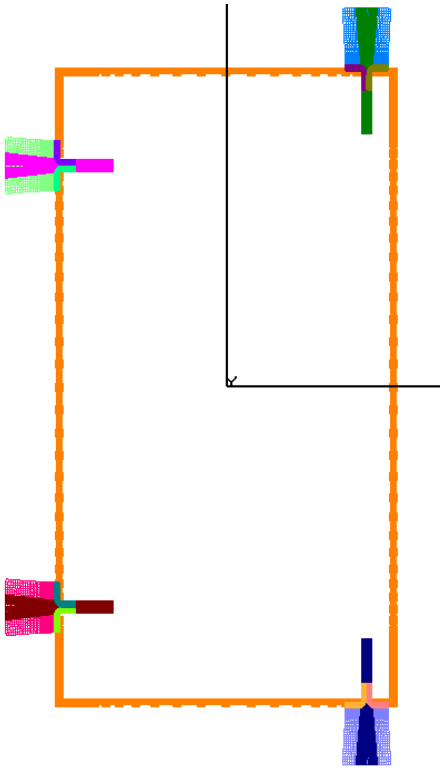

Figure 4.4 Grid of the full configuration case. Image of the x-z plane at mid-span (y = 0).

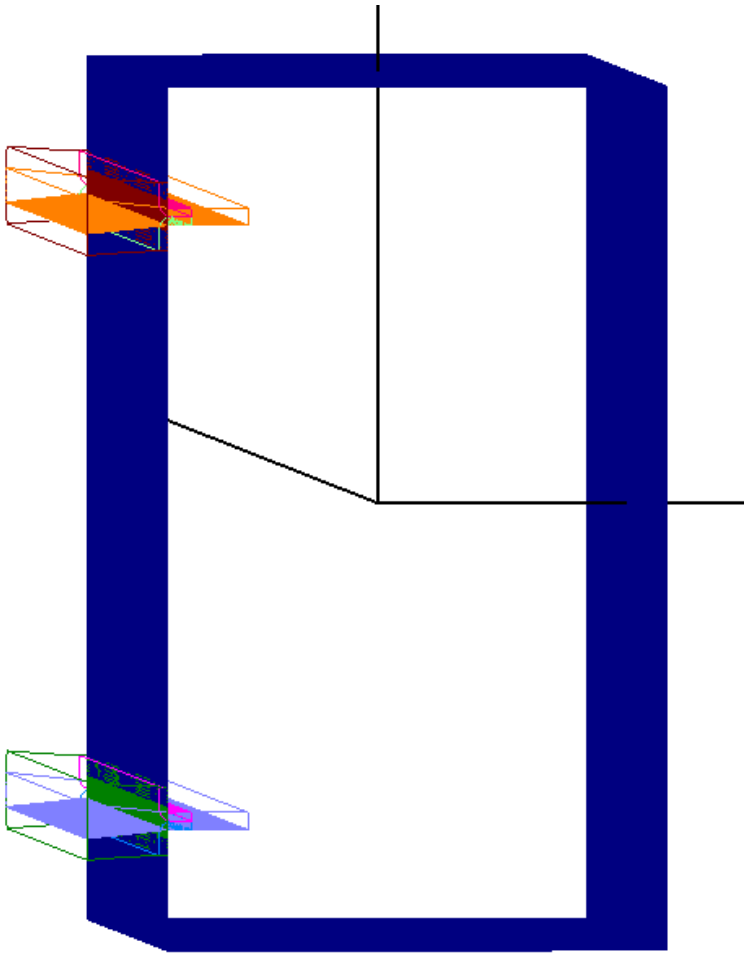

Figure 4.5 Complete 3-D grid for the front suction case.

4.3 SIMULATION PARAMETERS

The Reynolds number of the simulation was set to 500 with the free-stream Mach number being reduced to 0.01. To force asymmetry in the flow, the angle of attack was set to 0.01 degrees, but for this set of simulations the side slip angle was 0 degrees. Again, the other values were left as their default as they appear in the Overflow manual. The laminar flow solver was selected and the non-dimensional time step ta_∞/L was increased to 0.02. The selected numerical methods of solving the problem were set to be the same as the prior simulations. The right hand side of the Navier-Stokes equations were solved with Euler central difference terms, while the left hand side of the Navier-Stokes equations were solved using the ARC3D Beam-Warming block tridiagonal scheme.

For the simulations in this chapter, the initial conditions of the simulation were altered to force faster convergence. At start-up, a circular vortex with a linear velocity distribution in the radial direction and its diameter equal to the width of the rectangular cylinder h was placed upstream of the body. This vortex spanned from η_{min} to $\eta_{max,}$ and at the max radius, the velocity was set to be $2U_\infty$. This mound of vorticity was allowed to flow over the body and the simulations were stopped when a repeating oscillation pattern in the force coefficients was found.

4.4 Results and Discussion

The results of the simulations are summarized in Table 4.1. The drag coefficients of all three configurations were found to increase, but for different reasons. In Figs. 4.6 and 4.7, the pressure coefficient distributions for the front and back faces of all configurations are shown.

For the front suction case, the pressure coefficient showed a marked increase in the vicinity of the holes, which caused an increase in the drag coefficient. On the rear face of the configuration, we see that the pressure distribution is similar to the base case, but the mean pressure is increased. From our earlier arguments, this can be attributed to the increase in distance to vortex roll-up, which causes the free shear layer to be thinner. As can be seen in Fig. 4.9, the result was a reduction in contact the free shear layer had at the trailing edge corner and a reduction of the higher values of vorticity seen there. In addition, the shed vortex is slightly further out at max drag than its base case counterpart.

For the top/bot suction case, the distribution of the pressure coefficient on the rear face was found to be significantly lower than the base case. The cause of this was found to be an increase of vorticity in the shed vortex that forms near the rear face. Comparing Figs. 4.6 and 4.8, we notice the strong coloration corresponding to higher vorticity in the vortex on the rear face, which is due to the addition of vorticity from the hole adding itself to the free shear layer. The no-slip boundary condition applied to the walls of the hole results in a velocity profile that is approximately parabolic within the hole. This generates positive and negative vorticity that is pushed out of the hole. On the top surface, the free shear layer contains the positive vorticity, which is increased by the addition of positive vorticity from the hole. In addition, the negative vorticity from the hole adds

itself to the negative vorticity due to reversed flow on the surface. The combined effect results in a stronger shed vortex.

For the full configuration case, which was a combination of front suction and top/bot blowing, a significant increase in the drag coefficient occurred. The pressure coefficient on the front face saw a slight increase compared to the front suction case, while the pressure coefficient on the back face saw a slight decrease compared to the top/bot blowing case. This resulted in a drag coefficient 49% higher than the base case. In addition, the fluctuating lift was found to have decreased, which can be considered important for stability purposes.

The power spectra of the modified rectangular cylinders are shown in Figs. 4.12 - 4.14. In addition, the complete pressure coefficient on the surface of the body is shown in Fig. 4.15.

Table 4.1 Summary of results for modified rectangular cylinders

Simulation	C_d	St	$C_d{}'$	$C_L{}'$
AR 0.62 (Re = 500)	2.24	0.1832	0.3046	1.2831
Front suction	2.70	0.1532	0.2583	1.1228
Top/bot blowing	2.79	0.1832	0.3159	1.0733
Full Configuration	3.33	0.1832	0.2951	0.9572
AR 0.62 (Re = 20,000)	2.94	0.1460	N/A	N/A

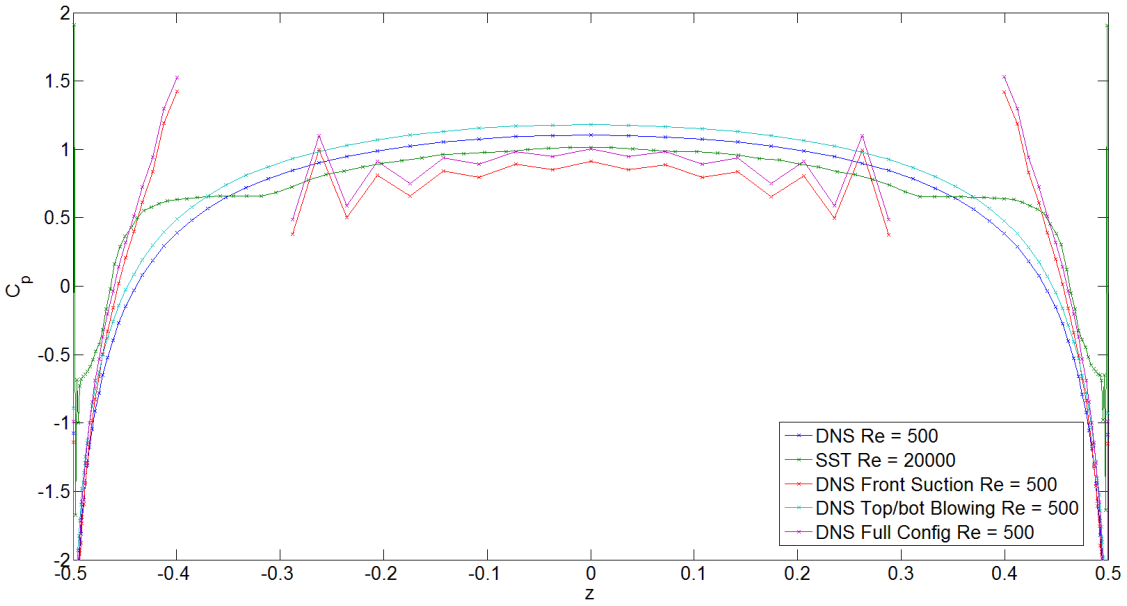

Figure 4.6 Distribution of the pressure coefficient on the front face for all configurations. The discontinuity in the front suction and full configuration cases is the location of the holes.

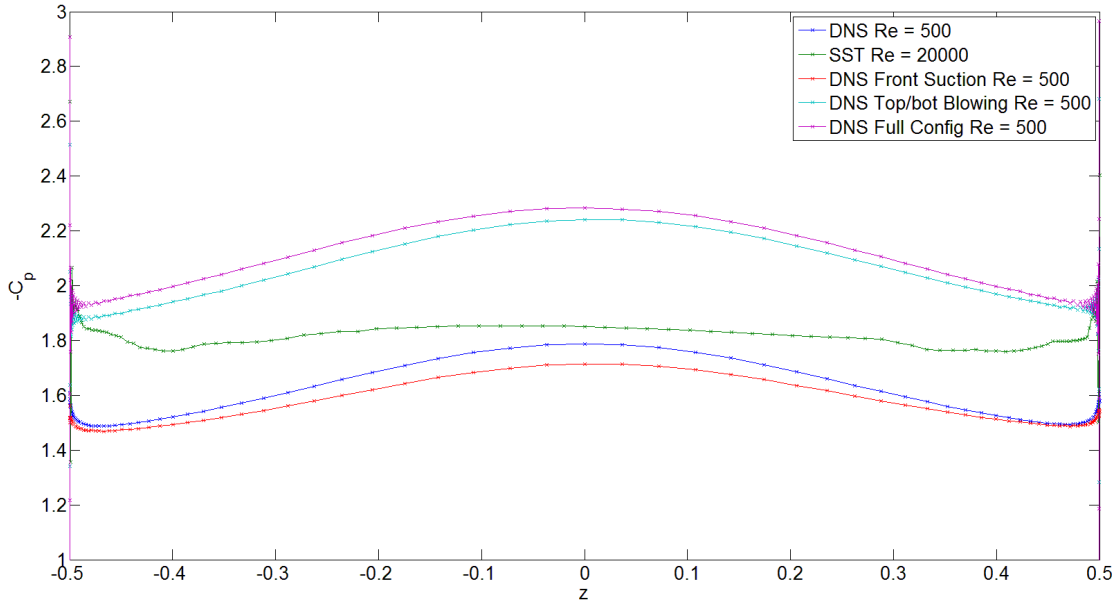

Figure 4.7 Distribution of the pressure coefficient on the back face for all configurations.

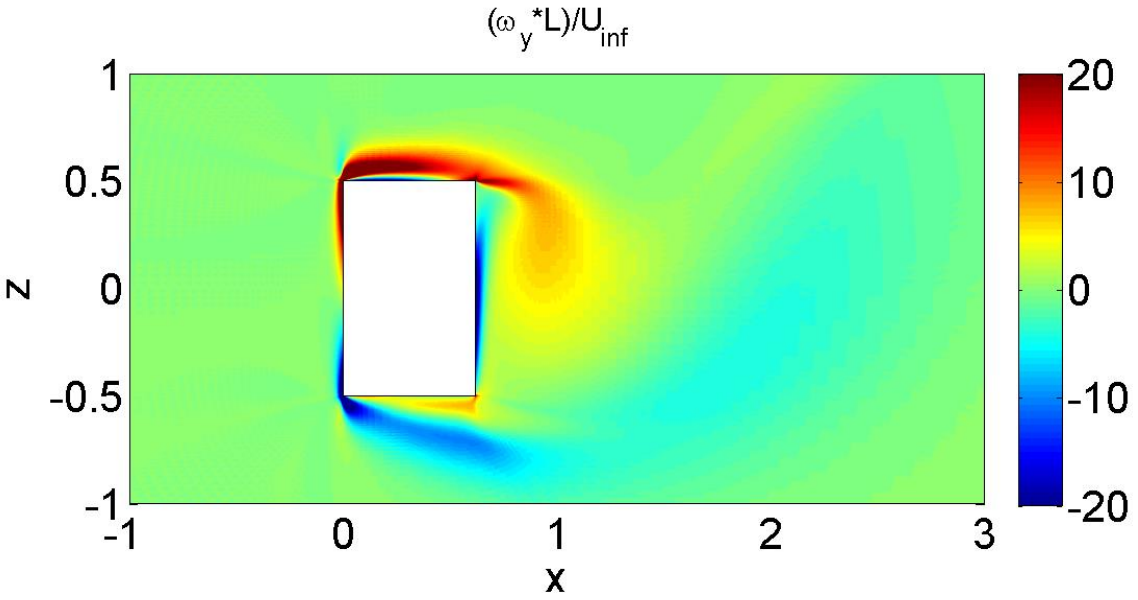

Figure 4.8 Normalized y-vorticity for the base aspect ratio 0.62 case.Image is of the x-z plane at mid-span.

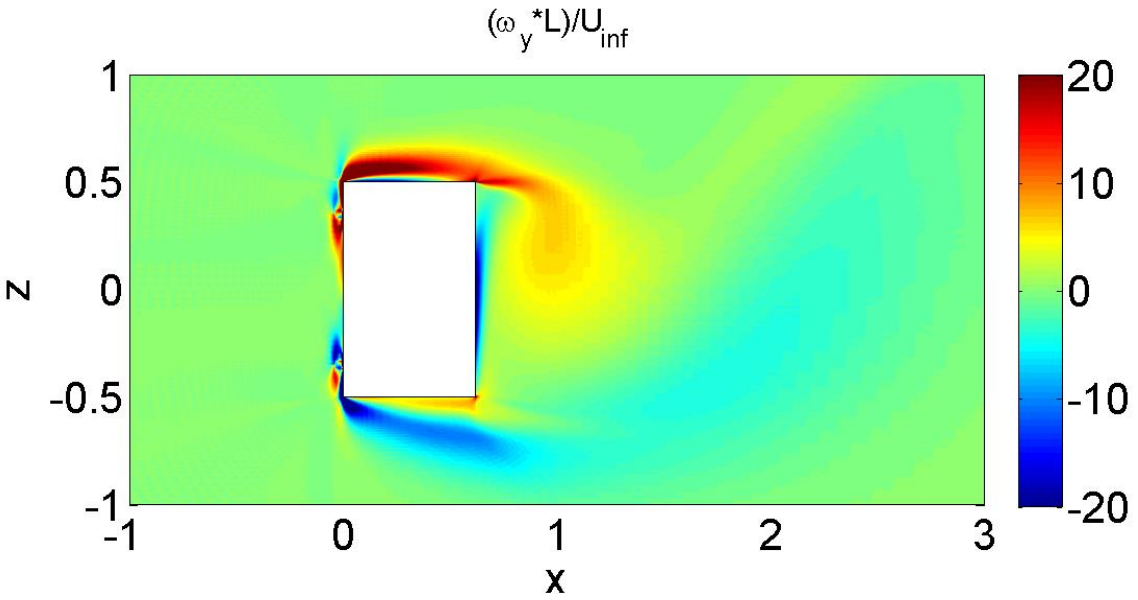

Figure 4.9 Normalized y-vorticity for front suction case. Image is of the x-z plane at mid-span.

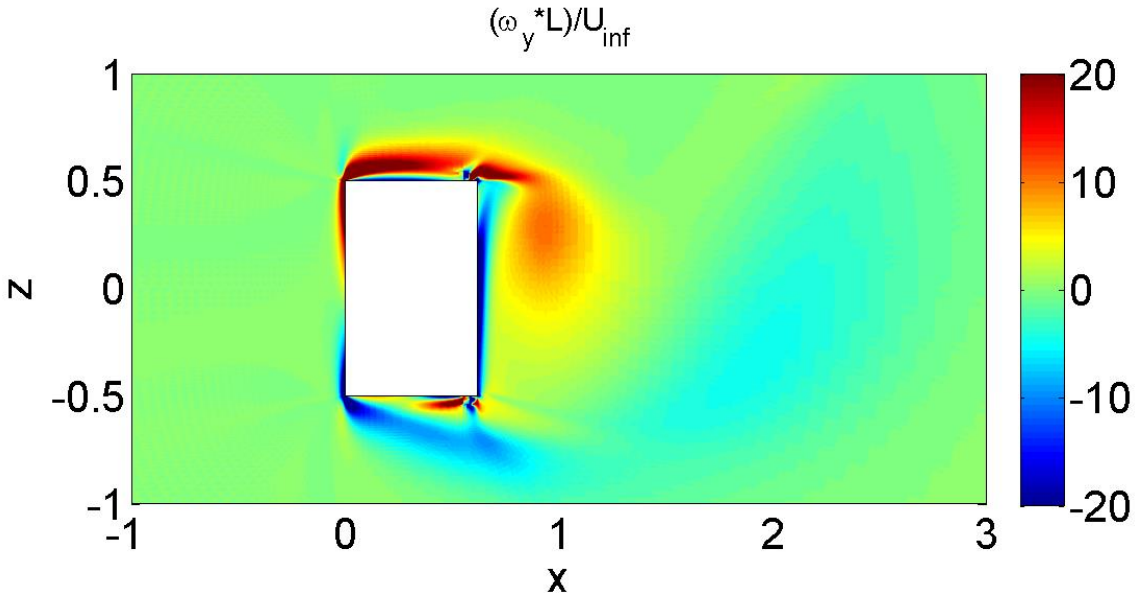

Figure 4.10 Normalized y-vorticity for top/bot blowing case. Image is of the x-z plane at mid-span.

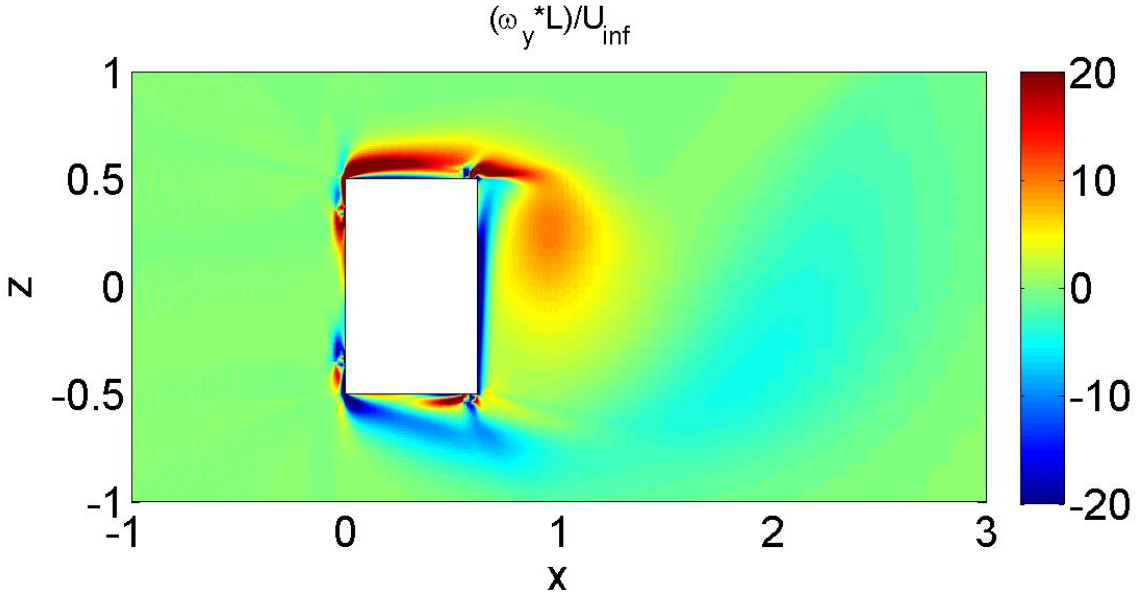

Figure 4.11 Normalized y-vorticity for full configuration case.Image is of the x-z plane at mid-span.

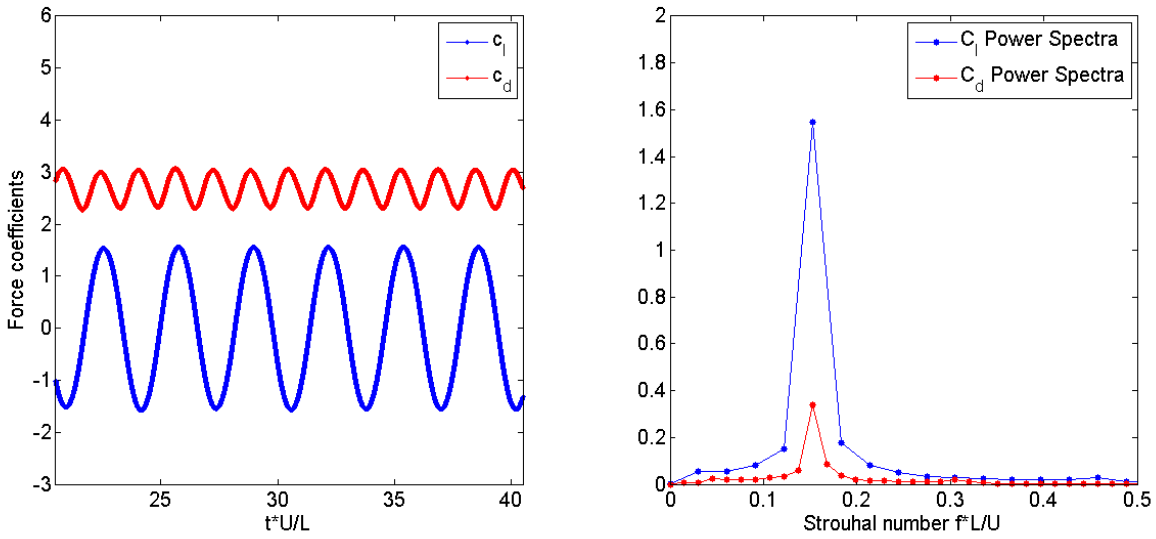

Figure 4.12 Time history and power spectra for the front suction case.

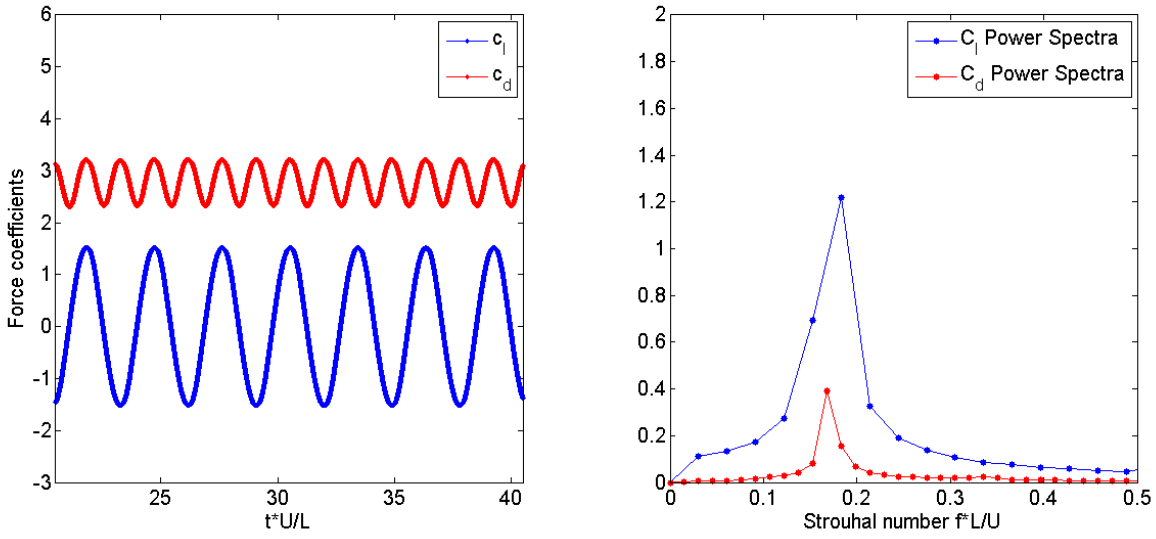

Figure 4.13 Time history and power spectra for the top/bot blowing case.

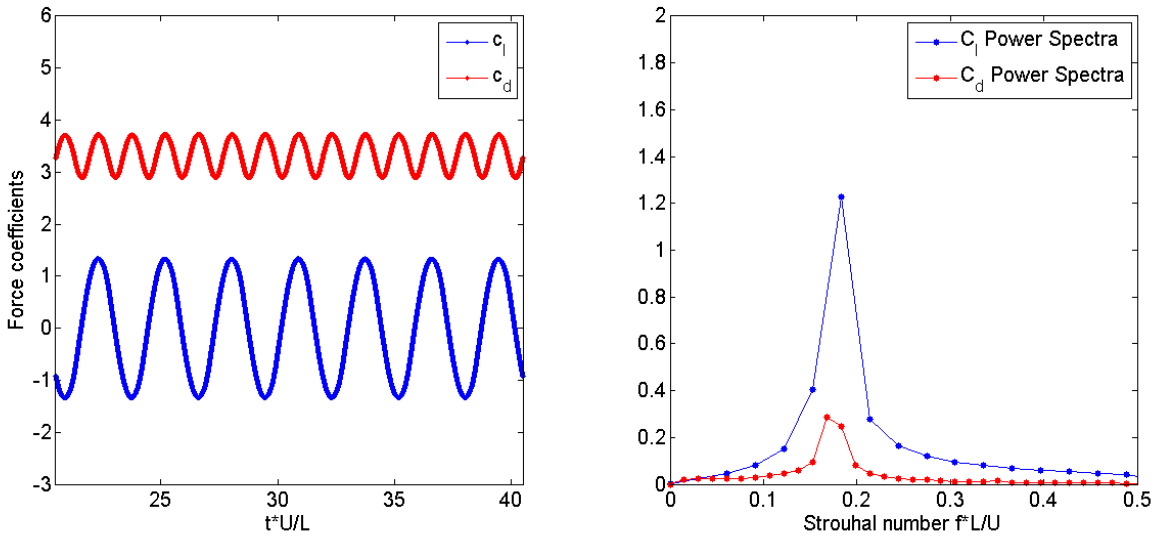

Figure 4.14 Time history and power spectra of the full configuration.

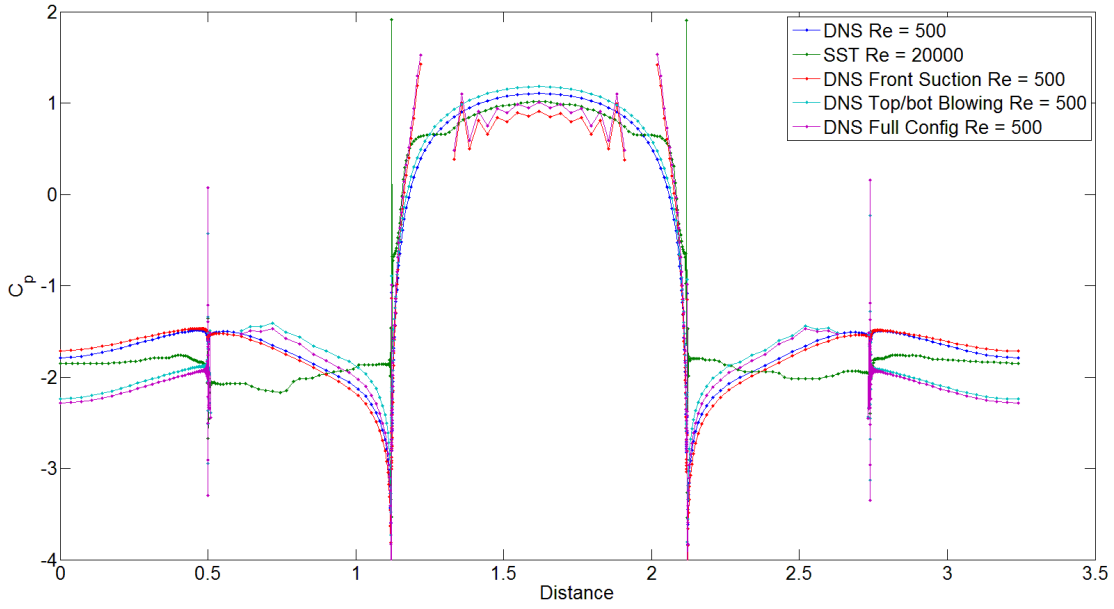

Figure 4.15 Distribution of the pressure coefficient on the entire surface for all configurations.

4.5 CONCLUSIONS

In this chapter, the simulations of modified 0.62 aspect ratio rectangular cylinders were presented. Three configurations were considered and all three configurations were found to have increased the drag coefficient, which was unexpected.

The front suction case exhibited an increase in pressure around the vicinity of the holes and increased the mean pressure on the front face. Meanwhile, the pressure on the rear face increased due to the shed vortex being further away from the body. The net result was an increase in the drag coefficient due to the increase in pressure on the front side being much greater than the increase in pressure on the back side. In analyzing the flow, it appears that the boundary layer thickness at the leading edge corner is only half the value seen in the base case. This would correspond to an effective increase in the Reynolds number by a factor of 4 and is still an order off of the original experiment. Ideally, we would like suction to occur closer to the leading edge corner, but for numerical reasons this could not be done. As a result, it appears that vortex roll-up in the free shear layer was not achieved and instead we see front suction increasing the distance to the formation of a shed vortex.

Unfortunately, the increase in drag in the front suction case was not for the reasons anticipated. It was thought that a decrease in pressure would occur on the rear side if we were able to make the shed vortex form closer to the rear face like it does in the Re = 20,000 case. However, this does mean the idea was wrong since it was estimated that the effective Reynolds number was raised by approximately a factor of 4 rather than the factor of 40 we need it to be to get from Re = 500 to 20,000.

In the top/bot suction case, the drag coefficient was expected to decrease due to the free shear layer being blown away from the body, but this was found not to be the case. The no slip boundary condition within the hole added vorticity to the flow. As can be seen in Fig. 4.10, the positive vorticity added itself to the positive vorticity in the free shear layer. This resulted in a stronger vortex, whose distance to formation was left unchanged. The stronger vortex decreased the pressure on the rear face and increased the drag. The negative vorticity added itself to the negative

vorticity of the reverse flow. Based on our explanation at higher Reynolds number, this would have increased the curvature of the free shear layer a bit. In tandem, the positive and negative vorticity from the hole both work towards increasing the drag.

In the full configuration, the best of the front suction and top/bot blowing cases can be seen. The pressure on the front face is increased for the reasons discussed for the front suction case, while the pressure on the rear face is decreased for the same reasons discussed from the top/bot blowing case. However, together we see an effect that is greater than what super position would imply. More simulations and experiments are needed to verify the ideas presented in this chapter, but they provide the framework for future engineers who would attempt to increase the drag of objects.

Chapter 5. CONCLUSION

5.1 SUMMARY

When it comes to rectangular cylinders, we have a class of fluid flow that waiting to be explored. The relatively recent discovery of the drag peak has led to more interest in the problem, but it still lags behind what we understand about the circular cylinder. This dissertation explored the problem numerically in an attempt to provide more insight for future researchers.

In Chapter 2, 2-D and 3-D RANS simulation results of rectangular cylinders at Re = 20,000 were presented. It was found that the 3-D simulations matched the original experiment in its entirety, while the 2-D simulations were only in agreement for aspect ratios greater than or equal to 0.6. The results of the 2-D simulations were found to be consistent with other published results. However, since we are interested in probing the physics of the flow there is some doubt as to what is driving the small scale features of the flow in the RANS simulations and so we made the move to DNS.

In Chapter 3, 3-D DNS simulations of rectangular cylinders at Re = 500 were presented. It was determined from the simulations that the flow had significantly changed in comparison to what had been observed experimentally at higher Reynolds numbers. The critical aspect ratio was found to be 0.2 with the max drag increasing to 3.09. In addition, it was shown that a mean spanwise flow exists for aspect ratios less than 0.5 with the exception of the aspect ratio 0.01 case. In that case, it is thought that there are some numerical issues, and this can be seen in the weak intensity of the power spectra plot for that case. Moreover, the impingement of the free shear layer was definitively shown to begin at aspect ratio 0.5 for the aspect ratios simulated. The concurrence of the mean spanwise flow and the free shear layer impingement is thought to be the cause of a local drag increase for the aspect ratio 0.5 case. It is also possible that this extends to the higher Reynolds number case as well.

The entrainment rate plays a central role in the trajectory of the free shear layer. At low Reynolds number, the separating vortex-sheet does not roll up near the separation point, but the shear layer remains laminar, with a very low entrainment rate. On the other hand, at high Reynolds number, the vortex sheet rolls up near the separation point, causing a relatively high entrainment rate. As high-speed fluid is entrained into the layer and mixes with low-speed fluid, it is decelerated. From the continuity equation, the mean streamlines must therefore diverge, corresponding to a much greater displacement thickness of the shear layer at high Reynolds number. The outer, high-speed flow is deflected according to the displacement thickness, so that at high Reynolds number, the shear layer trajectory is less curved than at low Reynolds number. Thus the critical aspect ratio for maximum drag is much larger at high Reynolds number.

According to this picture, the maximum drag coefficient at the critical aspect ratio is greater for the low Reynolds number case because the laminar vortex sheet is relatively thin. When the sheet rolls up into a vortex near the base of the body, the vortex core is relatively tight and compact, with a relatively low pressure. The average base pressure of the body is relatively low, yielding a relatively high drag coefficient.

In Chapter 4, 3-D DNS simulations of modified aspect ratio 0.62 rectangular cylinders were presented. In Chapter 3 it was shown that the distance to vortex roll-up within the free shear layer is proportional to the momentum thickness of the boundary layer on the front face and inversely proportional the square root of the Reynolds number. Thus, by applying suction to the front face boundary layer to thin the boundary layer, we attempted to raise the effective Reynolds number to 20,000, but we were unsuccessful in thinning the boundary layer by the factor of 40 needed to get there. However, we were successful in raising the drag of the Re = 500 case using 3 different configurations. The full configuration featured front suction and blowing out of the top and bottom and was successful in increasing the drag coefficient beyond its value at Re = 20,000 to 3.33.

5.2 SUGGESTIONS FOR FUTURE WORK

While the work presented in this dissertation has shown many interesting features related to rectangular cylinder flow, there are numerous questions that are left unanswered. The importance

of spanwise flow and the impingement of the free shear layer are not fully understood in relation to the drag increase at Re = 500. In addition, the role of vortex roll-up and entrainment in the free shear layer is waiting to be explored. Here we present some suggestions for future work:

- **How does the spanwise flow change if the ratio of span to height is changed?** In the simulations presented in this paper, the span b to height h ratio was set to 2, but it can be imagined there is a change in the spanwise flow depending on this ratio. In simple harmonics, when considering air in pipes, different modes exist that are dependent on wave speed and the length of the tube. If we change the span, are there other modes or flows that exist?

- **What is the effect of suction on the back face?** In rectangular cylinder flows, it has been shown that the proximity shed vortex to the rear face is the primary reason for an increase in drag. It can be imagined that suction from a hole on the rear face will bring the shed vortex even closer to the body and increase the drag further.

- **Can front suction be used to reproduce the distribution of pressure on the rear face at a higher Reynolds number?** The front suction case presented was successful in increasing the drag coefficient, but not for the reasons originally thought. The front suction case failed to thin the boundary layer sufficiently to raise the effective Reynolds number to 20,000 or higher, which leaves the idea of front suction starting vortex roll-up in the free shear layer unproven.

- **What is the interaction between entrainment, spanwise flow, and free shear layer impingement at higher Reynolds numbers?** Bluff body flows are one of the most complex flows in nature and happen to occur everywhere. From what we have shown in this dissertation, there is definitely a complex interaction between spanwise flow, free shear layer impingement, and free shear layer entrainment. The arguments, thus far, have remained qualitative, so explaining the process definitively is left to future researchers.

BIBLIOGRAPHY

[1] H. Nakaguchi, K. Hashimoto and S. Muto, "An experimental study on aerodynamic drag of rectangular cylinders," *Journal of the Japan Society of Aeronautical and Space Sciences,* no. 16, pp. 1-5, 1967.

[2] P. W. Bearman and D. M. Trueman, "An investigation of the flow around rectangular cylinders," *Aeronautical Quarterly,* no. 23, pp. 229-237, 1972.

[3] S. F. Hoerner, Fluid-Dynamic Drag, Published by the Author, 1965.

[4] A. Okajima, "Strouhal numbers of rectangular cylinders," *Journal of Fluid Mechanics,* vol. 123, pp. 379-398, 1982.

[5] R. W. Davis and E. F. Moore, "A numerical study of vortex shedding from rectangles," *Journal of Fluid Mechanics,* vol. 116, pp. 475-506, 1982.

[6] A. Okajima, "Numerical simulation of flow around rectangular cylinders," *Journal of Wind Engineering and Industrial Aerodynamics,* vol. 30, pp. 171-180, 1990.

[7] W. Rodi, "Comparison of LES and RANS calculations of the flow around bluff bodies," *Journal of Wind Engineering and Industrial Aerodynamics,* Vols. 69-71, pp. 55-75, 1997.

[8] A. Sohankar, C. Norberg and L. Davidson, "Numerical simulation of flow past a square cylinder," in *Proceedings of FEDSM99 3rd ASME/JSM Joint Fluids Engineering Conference,* San Francisco, California, 1999.

[9] K. Shimada and T. Ishihara, "Application of a modified k-ε model to the prediction of aerodynamic characteristics of rectangular cross-section cylinders," *Journal of Fluids and Structures,* vol. 16, no. 4, pp. 465-485, 2002.

[10] D. A. Lyn, S. Einav, W. Rodi and J. H. Park, "A laser-Doppler velocimetry study of ensemble-averaged characteristics of the turbulent near wake of a square cylinder," *Journal of Fluid Mechanics,* vol. 304, pp. 285-319, 1995.

[11] J. Conlon, "OVERFLOW code empowers computational fluid dynamics," NASA, [Online]. Available: http://www.hq.nasa.gov/hpcc/insights/vol5/overflow.htm. [Accessed 20 May 2015].

[12] R. H. Nichols and P. G. Buning, "OVERFLOW 2 User Manual," NASA, August 2010. [Online]. Available: people.nas.nasa.gov/~pulliam/Overflow/Overflow_Manuals.html. [Accessed May 2015].

[13] M. Shur, P. R. Spalart, M. Strelets and A. Travin, "Detached-eddy simulation of an airfoil at high angle of attack," in *Engineering Turbulence Modelling and Experiments 4*, Elsevier, Amsterdam, 1999.

[14] F. M. White, Viscous Fluid Flow, New York: McGraw-Hill, Inc., 1974.

[15] "Boussinesq eddy viscosity assumption," CFD Online, [Online]. Available: http://www.cfd-online.com/Wiki/Boussinesq_eddy_viscosity_assumption. [Accessed May 2015].

[16] B. S. Baldwin and T. J. Barth, "A one-equation turbulence transport model for high Reynolds number wall-bounded flows," NASA Technical Memorandum 102847, 1990.

[17] P. R. Spalart and S. R. Allmaras, "A one-equation turbulence model for aerodynamic flows," *Recherche Aerospatiale,* vol. 1, pp. 5-21, 1994.

[18] F. R. Menter, "Improved two-equation k-ω turbulence models for aerodynamic flows," NASA Technical Memorandum 103975, 1992.

[19] X. Tian, M. C. Ong, J. Yang and D. Murhag, "Unsteady RANS simulations of flow around rectangular cylinders with different aspect ratios," *Ocean Engineering,* vol. 58, pp. 208-216, 2012.

[20] A. Roshko, "Perspectives on bluff body aerodynamics," *Journal of Wind Engineering and Industrial Aerodynamics,* vol. 49, pp. 79-100, 1993.

[21] C. H. K. Williamson, "Vortex dynamics in the cylinder wake," *Annual Review of Fluid Mechanics,* vol. 28, pp. 477-539, 1996.

[22] H. K. Moffat, "Viscous and resistive eddies near a sharp corner," *Journal of Fluid Mechanics,* vol. 18, no. 1, pp. 1-18, 1964.

[23] R. Franke and W. Rodi, "Calculation of vortex shedding past a square cylinder with various turbulence models," in *Turbulent Shear Flows, vol. 8*, Springer, Berlin, 1993.

[24] M. Kato and B. E. Launder, "The modeling of turbulent flow around stationary and vibrating square cylinders," in *Ninth Symposium on Turbulent Shear Flows, Paper 10-4*, Kyoto, Japan, 1993.

[25] K. Koenig and A. Roshko, "An experimental study of geometrical effects on the drag and flow field of two bluff bodies separated by a gap," *Journal of Fluid Mechanics,* vol. 156, pp. 167-204, 1985.

[26] P. G. Saffman, Vortex Dynamics, Cambridge: Cambridge University Press, 1992.

VITA

Jonathan M. Wai was born and raised south of Seattle in Renton, WA. The son of a University of Washington graduate and aeronautical engineer, he was introduced to the university by attending football games as a child. Upon graduating high school, he was admitted to the University of Washington and never left. In 2007, he received his degree from the Aeronautics and Astronautics department and an M.S.A.A. under the direction of Peter Rhines in 2009. He decided to continue his education further and received a Ph.D. from the same department 2015.